Functionalised Iron Oxide Nanoparticles for Magnetophoretic Transport in the Extracellular Matrix

By

Stephen James Lyons

Thesis Submitted for the Degree of Doctor of Philosophy

Supervisors:
Dr. Aoife Morrin
Prof. Dermot Brougham

School of Chemical Sciences **MAY 2020**

Declaration:

I hereby certify that this material, which I now submit for assessment on the programme of study leading to the award of PhD, is entirely my own work, that I have exercised reasonable care to ensure that the work is original, and does not to the best of my knowledge breach any law of copyright, and has not been taken from the work of others save and to the extent that such work has been cited and acknowledged within the text of my work.

Signed:

(Candidate) ID NO: 16210086

Date: 14/09/2020

Table of Contents

Chapter 1 Recent Advances in Magnetic Nanoparticles for Biomedical Applications

Chapter 2 Magnetophoretic Transport of Functionalised Iron Oxide Nanoparticles Through Hydrated Polymer Networks

Chapter 3 Theoretical Study and Electrostatically-Modulated Magnetophoretic Transport of MNPs Through Hydrated Polymer Networks

Chapter 4 Magnetophoretic Transport of Functionalised Iron Oxide Nanoparticles Through Collagen-Based Gels and Cultured ECM

Chapter 5 Biomarker Capture from Hydrated Polymer Networks and Cultured Extracellular Matrix

Chapter 6 Conclusion and Future Work

List of Abbreviations

%D	Percentage difference
ΔE	Energy barrier to moment reversal
∇B	Magnetic field Gradient
μ_0	Permeability of free space
APTES	(3-aminopropyl)triethoxylsilane
B	Magnetic field strength
BA	Boronic acid
Ba	Benzyl alcohol
Da	Dopamine
d_{hyd}	Hydrodynamic diameter
DI H_2O	Deionised water
DLS	Dynamic light scattering
DMEM	Dulbecco’s modified eagle medium
DMF	Dimethylformamide
DS	Dopamine sulphonate
ECM	Extracellular matrix
EDL	Electric double layer
EE	Enrichment-exclusion
EEO	Electroendosmosis
ELISA	Enzyme-linked immunosorbent assay
EPI	Epirubicin
F_D	Drag force
F_M	Magnetic force
FTIR	Fourier-transfer infrared spectroscopy
GLYMO	(3-glycidyloxypropyl)trimethoxysilane
H	Response of material to a magnetic field
H_2O_2	Hydrogen peroxide
Hc	Coercivity
HCl	Hydrochloric acid
HGMS	High gradient magnetic separation
HK	Hexokinase
IS	Ionic strength
ISF	Interstitial fluid
K	Anisotropy energy density
Ka	Disassociation constant
k_B	Boltzmann constant
KOH	Potassium hydroxide
LOD	Limit of detection
m	Magnetic force acting on a dipole
M	Magnetic moment per unit volume
MEEA	2-[2-(2-Methoxyethoxy)ethoxy]acetic acid
MNP	Magnetic nanoparticle

Mr	Remnant magnetisation
MRI	Magnetic resonance imaging
Ms	Saturation magnetisation
η	Viscosity
NP	Nanoparticle
OA	Osteoarthritis
PBS	Phosphate buffered saline
PCA	Polyacrylate
PDI	Polydispersity index
PEG	Polyethylene glycol
pKa_{exp}	Experimental pKa value
PLA	Poly-L-lactic acid
PVA	Polyvinyl alcohol
r	Radius of the particle
SEM	Scanning electron microscope
T	Temperature
T_B	Brownian motion relaxation time
TEM	Transmission electron microscopy
THF	Tetrahydrofuran
T_N	Neel relaxation time
UV	Ultraviolet
v	Velocity
v_{exp}	Experimental velocity
V_m	Particle volume
VSM	Vibrating sample magnetometer
v_{th}	Theoretical velocity
ζ_p	Zeta potential
λD	Debye length
φ	Porosity factor
χ	Magnetic susceptibility

List of Figures

List of Tables

List of Publications and Presentations

Publications

S. Lyons, E. P. Mc Kiernan, G. Dee, D. Brougham & A. Morrin, Electrostatically modulated magnetophoretic transport of functionalised iron oxide nanoparticles through hydrated networks, Nanoscale, 2020.

This body of work was published in January of 2020 in Nanoscale. This publication focuses on the effect of electrostatics on magnetophoretic transport as described in Chapter 3.

Oral Presentations

Protein Mining in Skin Interstitial Fluid for Melanoma Biomarkers, Analytical Research Forum (ARF), London, England, 2016.

Characterisation of Superparamagnetic Nanoparticles for Biomedical Applications Within the Extracellular matrix, Perspectives in Percutaneous Penetration (PPP), Le Grand Motte, France, 2018.

Characterisation of Superparamagnetic Nanoparticles for Biomedical Applications Within the Extracellular matrix, 9th annual Council for Analytical Sciences in Ireland, Maynooth, Ireland, 2018.

Poster Presentations

Protein Mining in Skin Interstitial Fluid for Melanoma Biomarkers, Analytical Research Forum (ARF), London, England, 2016.

Superparamagnetic Nanoparticles: Velocity, Motion & Behaviour, 4th Insight Student Conference, University College Cork, Cork, Ireland, 2017.

Synthesis and Functionalisation of Magnetic Nanoparticles for Biomedical applications,69th Irish Universities Chemistry Research Colloquium, Dublin City University, Dublin, Ireland, 2018.

Characterisation of Superparamagnetic Nanoparticles for Biomedical Applications Within the Extracellular matrix, Perspectives in Percutaneous Penetration (PPP), Le Grand Motte, France, 2018.

Acknowledgments

I would like to acknowledge the guidance and support by my primary supervisor Dr. Aoife Morrin and my secondary supervisor Prof. Dermot Brougham.

I would like to thank my Mother, Father, Charlie and Una for their never-ending support throughout the 4 years of this research.

Abstract

Magnetic nanoparticles (MNPs) are allowing for new approaches to drug delivery, biomarker capture and are also enabling cancer treatments such as magnetic field hyperthermia and magnetic drug delivery. Applied research into functionalised MNPs is now advancing to in-vivo studies as their unique properties such as magnetic responsiveness and small scale are being exploited to overcome some pre-existing limitations for non-invasive in-vivo applications. One prominent application is magnetophoretic delivery of MNPs within tissue to a desired location in the body. While there has been an increasing interest in magnetophoresis from a fundamental point of view, a detailed picture of how the motion of MNPs is influenced by the characteristics of the surrounding tissue environment is lacking. Addressing this would improve reliability, accuracy and precision of magnetic guidance techniques. By understanding how molecular interactions influence functionalised MNPs interactions with biological tissue, appropriate measures can be taken in their future design and in-vivo delivery to ensure precise and reliable magnetic motion and guidance.

This thesis attempts to contribute to the understanding of magnetophoretic behaviour of functionalised iron oxide nanoparticles in biological tissue. In the first instance, a new optical imaging method is proposed to study functionalised MNPs undergoing magnetophoretic transport through biological tissue mimics including hydrogels and cultured extracellular matrix (ECM). Following the establishment of the method, the impact of chemical and physical attributes of the MNP, as well as the nature of the tissue mimic environment and their interactions, on magnetophoretic motion in different field gradients is examined. This work provides insights into electrostatic interactions as a modulator of magnetophoretic transport of MNPs which are important in the context of biological transport, given the nature of the ECM in tissue. The application of this new knowledge is then applied to biomarker sampling from tissue mimics using functionalised MNPs. The impact of MNP-biomarker binding and uptake on magnetophoretic behaviour is investigated and the analytical capability of the novel approach elucidated. The approach developed here is demonstrated to have potential for minimally-invasive sampling of biomarkers from complex, biphasic environments such as the ECM.

Chapter 1

Recent Advances in Magnetic Nanoparticles for Biomedical Applications

1.1. Introduction

Nanoparticles (NPs) are classified as a material having at least one dimension between 1 and 100 nm[1]. NPs are an important class of material that demonstrates unique properties on account of their size dimension, high surface area, reactivity, tuneable surface chemistry and can be made from a variety of materials[2]. These unique properties arise from various attributes[3], including the small scale of NPs that put them in the size range of biomolecules such as proteins. NPs can comprise of a variety of materials such as metals including gold and silver, inorganic materials such as silica and polymers such as polyvinyl alcohol (PVA), polyethylene glycol (PEG) and polystyrene[4]. NPs that possess a responsive magnetic moment are known as magnetic nanoparticles (MNPs) and comprise, at least partially of magnetic materials including iron, nickel or cobalt. They have great potential for use in a variety of applications, ranging from tumour therapy, biodetection, nuclear magnetic resonance (NMR) imaging, drug delivery and biocapture[5,6]. The key characteristic of a MNP is its susceptibility to an external magnetic field. This induces the response of the MNP in a magnetic field. Being manipulated by an external magnetic field, coupled with their intrinsic penetrability into human tissue opens up a variety of biological applications for MNPs[7]. For example, MNPs can resonantly respond to time-varying magnetic fields, causing its magnetic core to heat and so are being developed to be used as hyperthermia agents to destroy tumours or cancer cells in-vivo[8].

MNPs have sizes that can range from just a few nm to tens of nm where their size scale determines their magnetic properties. They have a similar size scale to biological cells[9], reducing the risk of a MNP being identified by the hosts immune system. Recognition can lead to aggregation which would cause major issues for in-vivo applications. The magnetic cores of MNP are typically functionalised in order to stabilise them and to allow them to be tailored for a particular application[10]. The surface chemistry can be tailored to target or bind biomarkers, or control their interactions with or respond to their environment, i.e. to trigger drug release. This chapter will discuss the fundamentals and underlying physics of MNP materials, approaches to surface functionalisation and their biological applications.

1.2 Fundamentals of magnetism

Magnetism is defined as an attractive and repulsive phenomenon produced by a moving electric charge[11]. The affected region around a moving charge consists of both an electric and magnetic field. All materials exhibit a form of magnetism but magnetic behaviour depends on the electron configuration of the atoms and temperature[12]. The electron configuration can cause magnetic moments to cancel each other out (making the material less magnetic) or align (making the material more magnetic). The magnetic moment refers to the magnetic strength and orientation of a magnet in response to a magnetic field. Increasing the temperature increases random thermal motion, making it harder for electrons to align, and typically decreases the magnetic strength of a material. Magnetic materials can be classified into five main types of magnetism; ferromagnetism, ferrimagnetism, antiferromagnetism, paramagnetism and diamagnetism.

Ferromagnetism occurs when the magnetic moments align spontaneously below their Curie temperature[13]. The Curie temperature is related to a magnetic material, it can cause sharp changes in their magnetic properties when reached. In ferromagnetic materials, the magnetic moments align in a parallel manner in an equal arrangement. With ferrimagnetism the magnetic moments are unequal in magnitude and align themselves in an antiparallel arrangement[14]. Antiferromagnetism occurs at the Curie temperature, where the magnetic moments align parallel to each other. At this temperature, the aligned magnetic moments give no net magnetisation[15]. Paramagnetism is mainly observed in materials with an uneven number of electrons. The net magnetisation cannot be zero and will always respond to an external magnetic field. It is a weak form of magnetism seen in magnetic materials in response to an applied magnetic field[16]. Diamagnetism is found in materials that have a negative magnetic susceptibility. The negative susceptibility arises from a current induced by electron orbits that force the magnetic moments to align opposite an applied field. This results in the moments being shielded from an applied magnetic field.

The ability to guide MNPs is based on their response to an external magnetic field. Therefore, it is necessary to understand how this response is linked to the magnetic field.

When a magnetic material is introduced to a magnetic field, the individual atomic moments in the material contribute to its overall response[17,18]:

$$B = \mu_0(H+M) \tag{1.1}$$

where B is the magnetic flux or induction (T), μ_0 is the permeability of free space (TmA^{-1}), H is the magnetic field intensity (A/m) and M is the magnetisation per unit volume ($A\ m^{-1}$).

MNPs below 100 nm are single-domain particles and can have superparamagnetic properties. The total magnetic moment of these MNPs can be regarded as one giant magnetic moment, composed of all the individual magnetic moments of the atoms[19]. In superparamagnetic MNPs, magnetisation randomly flips direction under the influence of temperature[20]. The typical time between flips is called the Neel relaxation time. In the absence of an external magnetic field, when the time needed to measure the magnetisation of the NPs is much longer than the Neel relaxation time, the net value of magnetisation averages at zero and they are said to be in the superparamagnetic state[21](Figure 1.1). Superparamagnetic MNPs are commonly used in biomedical applications and would typically comprise of maghemite or magnetite with core diameters ranging from sub-10 to 80 nm[22,23].

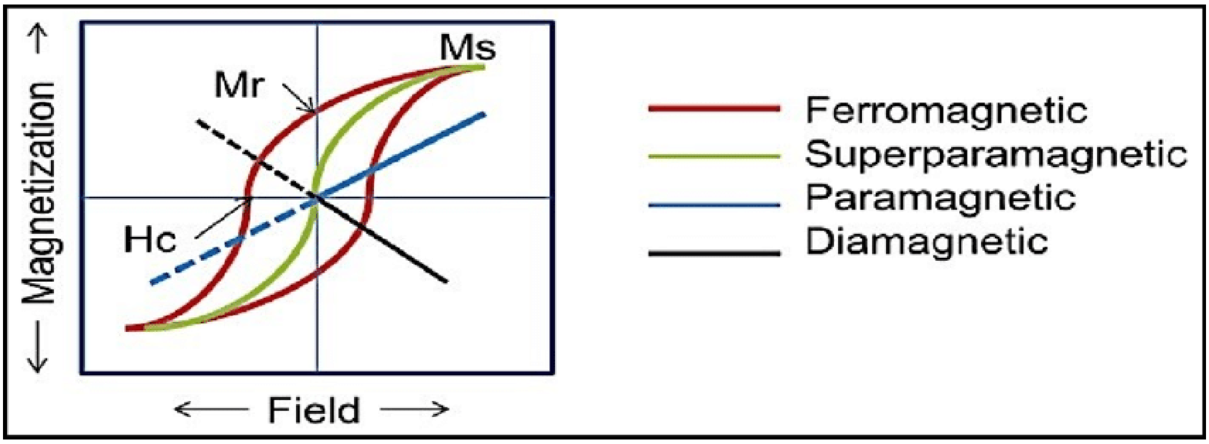

Figure 1.1 Magnetometry of ferromagnetic, superparamagnetic, paramagnetic and diamagnetic materials under the influence of an applied field showing saturation magnetisation (Ms), remnant magnetisation (Mr) and coercivity (Hc) (the intensity of an external field needed to force the magnetisation to zero)[24].

Superparamagnetism is dependent on two processes in a magnetic field, Neel relaxation (discussed above) and Brownian motion. The Neel relaxation (τ_N) process is determined by the magnetic anisotropic energy of the MNPs relative to the thermal energy. Brownian motion is the random movement of particles in a fluid due to collisions with other atoms and molecules in solution. Both Neel relaxation and Brownian motion processes are characterised by a relaxation time: τ_B for the Brownian process which depends on the hydrodynamic properties of the fluid, is the time taken for a particle to return to its original position; Both Brownian and Neel processes will be present in a MNP dispersion. Only τ_N is relevant in fixed MNPs where no physical rotation of the particle is possible. The underlying physics of superparamagnetism is founded on an activation law for the relaxation time τ_N of the net magnetisation of the particle:

$$\tau_N = \tau_0 \exp \left(\frac{\Delta E}{k_B T}\right) \qquad (1.2)$$

where τ_0 is the pre-exponential factor (s), ΔE is the energy barrier to moment reversal (J), k_B is the Boltzmann constant (JK^{-1}) and T is temperature (K).

For non-interacting particles, τ_0 is of the order 10^{-10}–10^{-12} s and is only weakly dependent on temperature. ΔE is influenced by general intrinsic and extrinsic effects such as the magnetocrystalline and shape anisotropies, respectively; but in the simplest of cases it is given by:

$$\Delta E = KV_m \qquad (1.3)$$

where K is the anisotropic energy density ($J \cdot m^{-3}$) and V_m is the particle volume (m^3).

This direct proportionality between ΔE and V_m is the reason that superparamagnetism—the thermally activated flipping of the net moment direction—is important for all small particles, since for them, ΔE is comparable to k_BT at room temperature.

For a material to magnetic, it must exhibit ferro-, ferri- or superparamagnetic behaviour at room temperature[25]. There are three classes of materials that meet this criteria; metals, alloys and oxides. Three metallic elements exhibit ferromagnetic properties - iron, cobalt and nickel. As bare metals, they have a high tendency to oxidise, so an oxidation-protective layer is needed for in vivo applications[26,27]. Alloys are ferromagnetic materials and can consist for example of cobalt/platinum or iron/platinum[28]. However, these materials have found little use in biomedical applications due to their strong magnetisation which can lead to aggregation and high toxicity. Iron oxides, on the other hand, have many uses for medical applications due to their biocompatibility and tuneable surface chemistry.

1.2.1 Fundamentals of magnetophoretic transport

In order to understand how a magnetic particle will move in an external magnetic field, it is important to understand the relationship between the two main forces that dictate magnetophoretic transport. These are the magnetic force (F_m) and the drag force (F_D)[29–31]. F_M is given by:

$$F_m = (m\nabla)\ B \tag{1.4}$$

where F_M ($kg \cdot m \cdot s^{-2}$) is the magnetic force acting on a point-like magnetic dipole ($A \cdot m^2$).

This equation can be geometrically interpreted as the differentiation of the magnetic energy $E_m = ½ \cdot m \cdot B$ with respect to the distance in the direction of m. In the case of particle of magnetization M ($A \cdot m^{-1}$) and magnetized volume V_m, the total magnetic moment, m, of the particle is defined as:

$$m = V_m \cdot M \tag{1.5}$$

The saturation magnetisation (M) is dependent on various parameters including the magnetic susceptibility, χ, of a particle in response to an external magnetic field according to:

$$M = \frac{\chi}{\mu_0} B \tag{1.6}$$

By substituting equations 1.6 and 1.5 into equation 1.4, the following is obtained:

$$F_m = \frac{V_m \chi}{\mu_0} (B\nabla)\ B \tag{1.7}$$

F_D is given by the following equation[29,32]:

$$F_D = 6\pi r \eta v \tag{1.8}$$

where r is the radius of the particle (m), η is the viscosity of the surrounding fluid (Pa·s) and v is the velocity ($m \cdot s^{-1}$).

When F_m is equal to F_D, a terminal velocity is achieved for a particle in a viscous medium under the influence of an external magnetic field. Thus equations 1.7 and 1.8 can be equated and an expression for terminal velocity, v, can be derived:

$$v = \frac{\chi_v V_m B \nabla B}{6\pi r \mu_0 \eta} \tag{1.9}$$

Studies into understanding the magnetophoretic factors that can influence a particles behaviour in a viscous medium have continued to gain attention for biomedical applications[33,34].

1.3 Magnetic nanoparticle synthesis

MNPs are synthesised from a variety of materials resulting in varying magnetic susceptibilities, stabilities and toxicities. Maghemite, hematite and magnetite are all iron oxides that can form superparamagnetic NPs[35,36]. They are typically synthesised from a precursor ferrite, which is a ceramic containing iron oxide and a mixture of copper, nickel, cobalt, magnesium or iron[37]. Size can be controlled by seed-mediated growth or capping agents[38]. A broad range of synthetic methods can be used to synthesise MNPs via chemical, physical and biological routes (Figure 1.2).

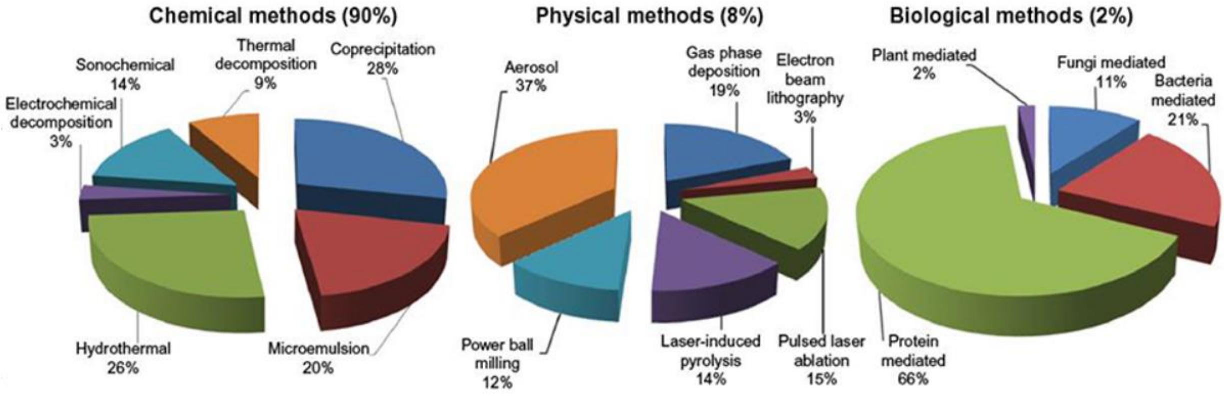

Figure 1.2 Comparative presentation of the synthesis of iron oxide magnetic nanoparticles by three different routes (2019)[39].

1.3.1 Iron oxide MNPs

Iron oxides are predominantly used as MNP cores in biomedical applications. The three most commonly used iron oxides are hematite, magnetite and maghemite. Hematite (α-Fe_2O_3) forms in a crystalline rhombohedral structure and usually is found with various other iron oxides. Hematite is an antiferromagnetic material with a Neel temperature of 600 °C. It is weakly magnetic and can bear a small magnetic charge due to surface defects of the hematite crystals. Hematite is the most chemically stable of all the oxide metals but has solubility issues in water and toxicity issues which limit their use in biomedical applications but they have found use in environmental applications[40].

Magnetite (Fe_3O_4) is a magnetic iron oxide that has a cubic inverse spinel structure with oxygen forming a closed packing and Fe cations occupying interstitial tetrahedral sites and octahedral sites. Electrons can hop between Fe^{2+} and Fe^{3+} ions in the octahedral sites at room temperature unlike maghemite, rendering magnetite an important class of half-metallic materials. This hopping between ions can contribute to an electric conductibility which can occur below 125 K. This is called the Verwey transition. It is ferrimagnetic and can be magnetised or used to magnetise other materials. Magnetite NPs are commonly used due to the superparamagnetic behaviour they exhibit at room temperature with high saturation magnetisation. In addition, their non-toxicity and high biocompatibility is important for biomedical applications[41]. The crystal structures of both magnetite and maghemite are based on a cubic dense packing of oxygen atoms differing only in the distribution of Fe ions within the crystal lattice. Maghemite (γ-Fe_2O_3) is a phase of iron oxide that has numerous in vivo applications due to its strong magnetic and optical properties. Its spinel structure and unit cell is the same as magnetite, it is also ferrimagnetic but with all Fe atom is in the higher oxidation state, unlike magnetite. Maghemite is more chemically stable than magnetite but magnetite is used more frequently, as it is often easier to synthesise and has higher bulk volume magnetisation (5 vs. 4×10^5 $A\cdot m^{-1}$).

1.3.2 Synthesis of iron oxide magnetic nanoparticles

1.3.2.1 Chemical synthesis

The chemical route is the most popular approach for the synthesis of MNPs. There are many different chemical methods, among which organic phase synthesis has become a popular choice due to its ease of controlling NP formation rate and protecting against uncontrolled oxidation during the synthetic process[42]. Co-precipitation is a well-established synthesis route for obtaining uniform small scale MNPs[43]. In the next section, co-precipitation and some non-aqueous phase methods will be discussed.

1.3.2.1.1 Co-precipitation

The co-precipitation method is for MNP synthesis is often used when high purity and good stoichiometric control are required. This is a very well-established synthesis method and was first reported by Massart[43]. However, this method can result in wide particle size distributions if the necessary precautions are not taken[44]. Fe_3O_4 or γ-Fe_2O_3 MNPs are synthesized from aqueous Fe^{2+}/Fe^{3+} salt solutions (2:1 stoichiometry) by the addition of a base under an inert atmosphere at room or at elevated temperature[45]. An oxygen-free environment is necessary during synthesis, otherwise magnetite can be further oxidised to ferric hydroxide. The synthesis carried out by Massart[43] produced MNPs with a core size of 6-8 nm. Petcharoen et al.[46], also synthesised magnetite MNPs by the Massart method using ammonium hydroxide as the precipitating agent (Figure 1.3).

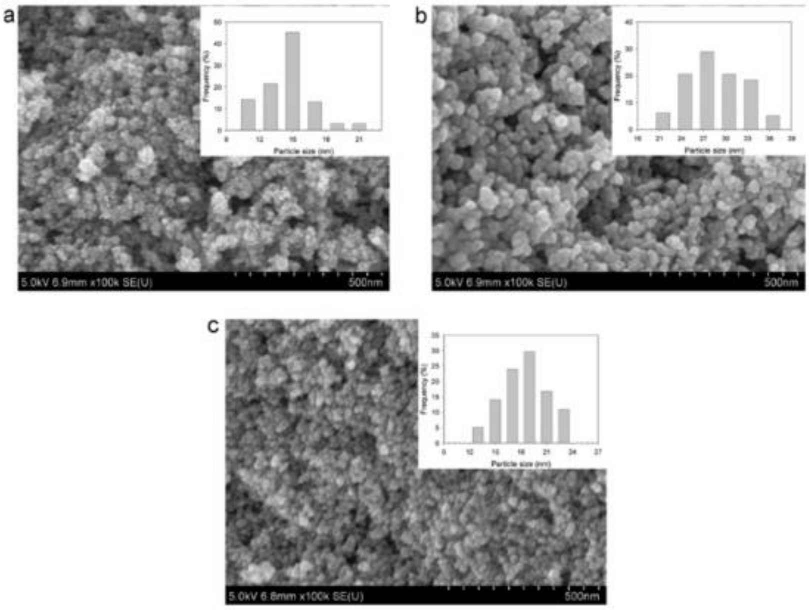

Figure 1.3 Scanning electron microscope (SEM) images of the (a) bare magnetite NPs (b) oleic acid-MNPs and (c) hexanoic acid-MNPs synthesised by a co-precipitation method (Ratio 1:2.45) by Petcharoen et al. [46]. Size distribution profiles inlaid for each SEM image.

They were prepared by the dissolution of iron (II) chloride and iron (III) chloride was controlled by reaction temperature. The MNPs were functionalised with oleic acid and hexanoic acid and resulted in an average hydrodynamic diameter (d_{hyd}) of 15.1 nm (Figure 1.3). In a publication by Martinez-Mera et al.[47], magnetite MNPs without surfactants were synthesised in a co-precipitation method using Fe^{2+}/Fe^{3+} salts at room temperature resulting in a MNP d_{hyd} of 7.9 nm in a ratio of 1:1 .

1.3.2.1.2 Non-aqueous phase

Synthesis methods like that of Massart that take place in the aqueous phase, have several conditions that need to be controlled and maintained such a pH, temperature, stoichiometric ratio of ions etc. The significant issue with the Massart method, is that the synthesised nanoparticles exhibit broad size range, typically with diameters between 5 and 15 nm. With this in mind, Sun et al.[48] synthesised monodisperse magnetite NPs controlled by seed-mediated growth with a high-temperature reaction (255°C) of iron(III) acetylacetonate in a high boiling point solvent at reflux such as diphenyl ether. Seed-mediated growth was used to control NP size by adding the iron(III) complex to the oil phase in the presence of oleic acid and oleylamine, which acted as capping agents. This resulted in monodisperse MNPs with a d_{TEM} of 4 nm. This method demonstrated that a high temperature reaction of iron (III) acetylacetonate in the presence of capping agents can be used to produce size-controlled monodisperse MNPs. However some of the reagents used can adsorb to the surface of the MNPs, and can be difficult to remove, especially when the goal is to transfer them into water, also ligand transfer can be with made like by aspartic adic containing polypeptide, after a water transfer step combined with oxidation using tetramethylammonium hydroxide treatment as described by Euliss et al.[49].

Later on, Pinna proposed a promising non-aqueous phase route for the synthesis of MNPs that has been applied for the preparation of nanocrystalline magnetite[50]. Carrying out the synthesis in a non-aqueous phase that is an aromatic alcohol, such as benzyl alcohol (Ba), can overcome the previously mentioned phase transfer limitation. Compared to fatty amines or carboxylic acids, Ba is a soft ligand and does not interact with the resulting MNPs but helps control the rate of crystallisation of the iron to the desired iron oxide.

The non-aqueous phase involves the partial reduction of some the iron complex iron(III) acetylacetonate into iron (II) species, in a solvent such as Ba and results in monocrystalline magnetite particles with sizes ranging from approx. 12-25 nm depending on temperature and length of reaction[50]. The resulting MNPs are highly crystalline, and size can be tailored, either by reaction temperature or by a post-reaction fractionation. The absence of surfactant results in a high-purity material. For example, this Pinna method was used by Ninjbadger et al.[51] to synthesise MNPs (d_{hyd} 12.6 nm) and low polydispersity index (PDI) values (0.16) across several dispersions were noted.

1.3.3 Physical synthesis

The most common types of physical syntheses route to MNPs employ spray pyrolysis, aerosol and electrobeam lithography techniques. Spray and laser pyrolysis have been shown to be excellent techniques for the direct and continuous high rate production of well-defined MNPs[52]. In spray pyrolysis, a solution of ferric salts and a reducing agent in organic solvent is sprayed into a series of reactors; where the aerosol solute condenses and the solvent evaporates. The resulting dried residue consists of particles whose size depends upon the initial size of the original droplets. Maghemite NPs with sizes ranging from 5 to 60 nm with different shapes have been obtained using different iron precursor salts in alcohol using this method[52]. Kumfer et al.[53] synthesised reduced iron oxide NPs using a gas-phase, laminar diffusion flame process. Gas/aerosol phase methods yield high quality products but the percentage yield is usually low. Variables such as oxygen concentration, gas phase impurities, and the heating time must be controlled precisely to obtain pure products.

1.3.4 Biological synthesis

Biological synthesis methods for MNPs use green reagents, and allow for large-scale production. The biological route, although expensive can allow for highly specific MNP synthesis. The most common method of biological synthesis is by protein mediation. Rawlings et al.[54] used magnetotactic bacteria to biomineralise MNPs within membrane vesicles (magnetosomes), which were embedded with dedicated proteins that control nanocrystal formation. The membranes were prone to aggregation so tight control of experimental conditions was required. Superparamagnetic magnetite and maghemite NPs were produced with a d_{hyd} range of 30-50 nm depending on protein concentration which dictates the crystallisation rate (Figure 1.4).

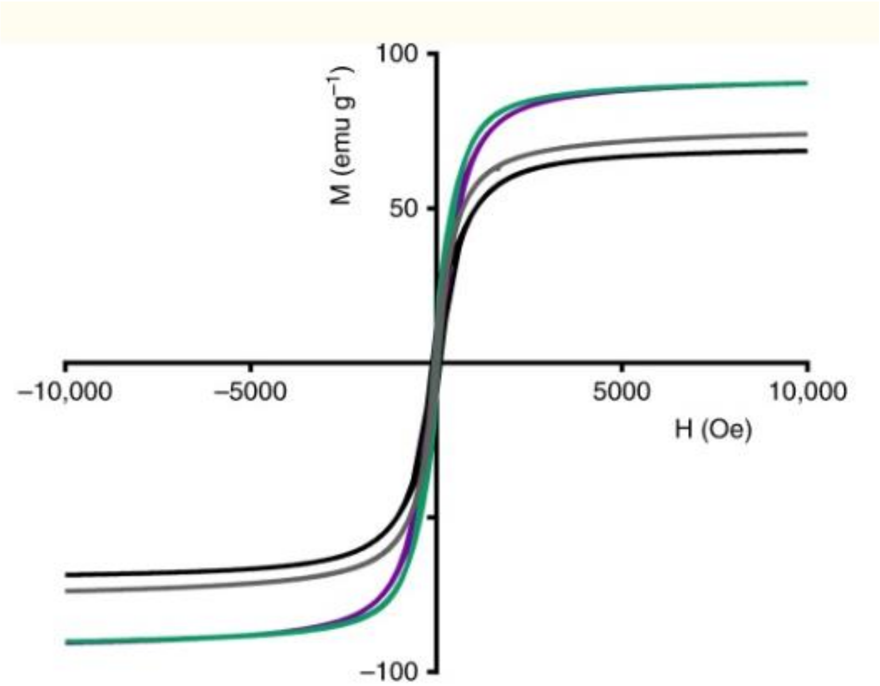

Figure 1.4 Vibrating sample magnetometry (VSM) analysis of particle samples generated with three coiled coil proteins, peptide, and a protein free control[54].

1.4 Surface functionalisation: Tuning iron oxide MNP properties

The MNP surface can be functionalised with various chemistries, to create stable dispersions, provide functionality and alleviate biocompatibility issues. Functionalisation can prevent aggregation, and improve colloidal stability for biomedical applications[55,56]. The hydroxyl groups present on the iron oxide core can covalently bind to a range of functional groups[57,58]. Depending on the synthesis approach used, residual surfactants can be present on the MNP surface. The residual surfactant that can be present from the synthesis process can dictate what functionalisation approach is needed. The surfactants can vary widely as it is usually responsible for the formation of the iron oxide and can include sodium oleate[59], oleic acid or oleyamine. The presence of these surfactants can limit their use in biomedical applications due to their necessity to remove them by ligand exchange or to add an amphiphilic polymer to disperse the MNPs in water[60].

Non-functionalised MNPs can be targeted by plasma proteins called opsonin's, which adsorb spontaneously on their surface[61]. This forms a protein corona by a process called opsonisation[62] (Figure 1.5). The corona forms due to the high surface free energy of the NPs, resulting in adsorption of various molecules, most notably proteins.

This protein corona can trigger aggregation through protein bridges, resulting in the formation of large MNP clusters which are detrimental to the bio-applicability of these materials[63]. Binding forces that are responsible for corona formation and aggregation include van der Waals, hydrophobic and electrostatic interactions[71]. Parameters affecting the extent of opsonisation are related to the physical properties of the MNP surface (size, material, etc.) and nature of chemical functionalisation[64].

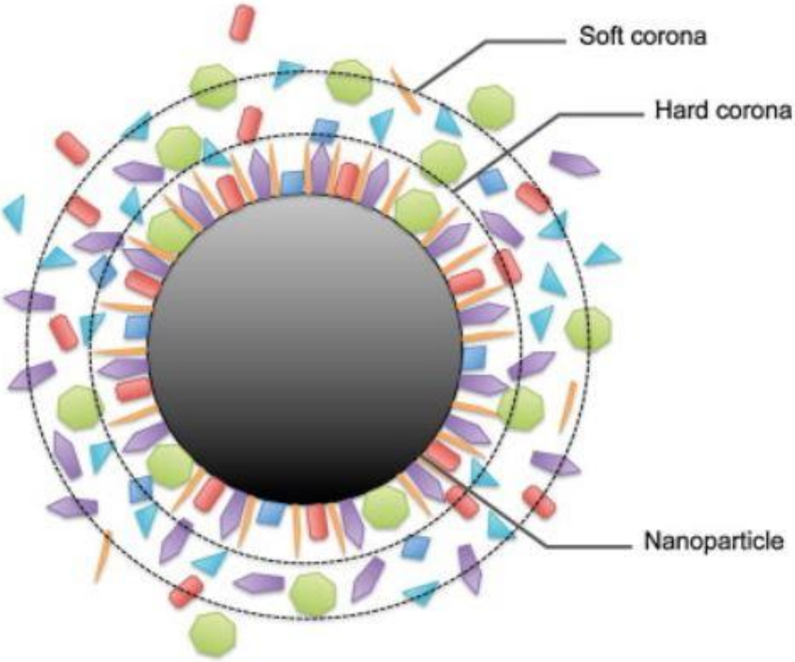

Figure 1.5 Formation of soft and hard protein coronas on a non-functionalised iron oxide NP[65].

1.4.1 Surface functionalisation of MNPs

As many iron oxide MNP synthesis methods are performed in organic solvents, functionalisation is needed to render them stable in the aqueous phase for biomedical applications[66]. This process is called phase transfer[67–69]. Phase transfer is necessary if the desired particle type cannot be synthesized with the corresponding ligand on the surface in a single phase. The choice of ligand is also dictated by the end-application requirements. Surface ligands can impart hydrophilicity or hydrophobicity, chemical functionality and colloidal stability to NPs.

There are three main methods employed for phase transfer, which are ligand exchange[70,71], ligand modification[72,73] and silanization[74,75] (Figure 1.6).

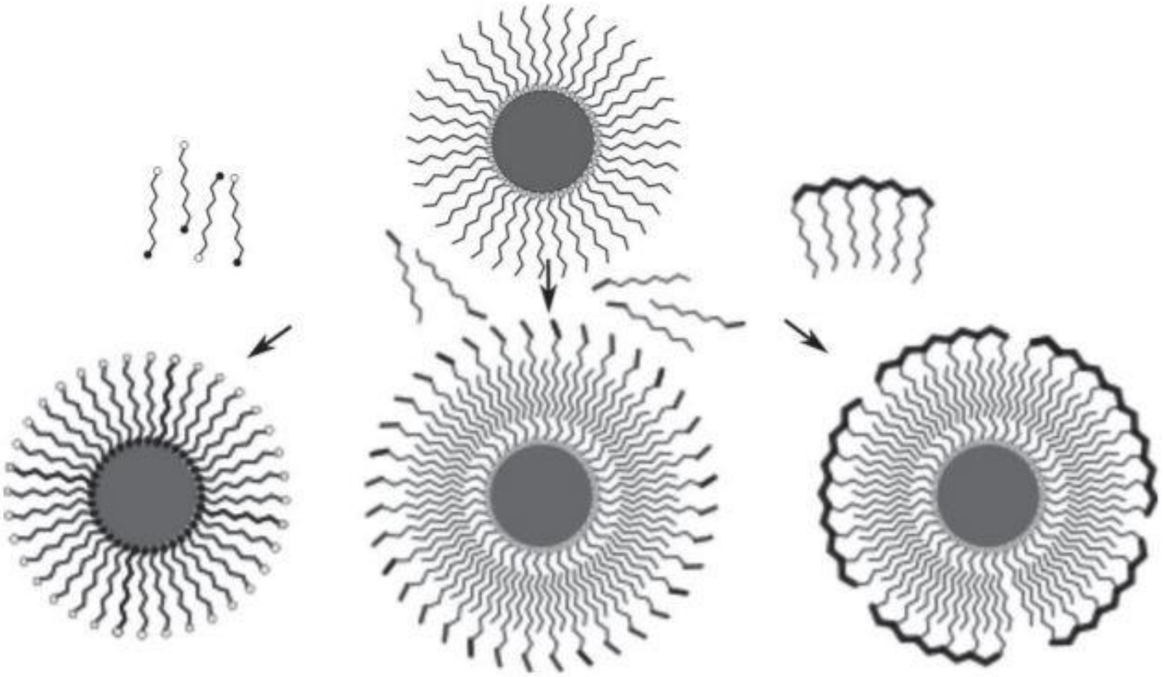

Figure 1.6 Different strategies for phase transfer of nanoparticles. Left: ligand exchange, the incoming ligand has one head group binding to the NPs surface (filled circles), the other end (empty circles) is e.g. hydrophilic. Centre: Ligand modification of existing ligands Right: existing silane functionalisation is then crosslinked with an inorganic silica shell (strong black)[67].

Ligand exchange is a common method used improve the stability of or impart functionality to NPs (Figure 1.6 Left), whereby ligand molecules (e.g. surfactants) on the NP surface can be exchanged by others[67,76]. These surfactants are common on the MNP surfaces due to their use as capping agents in the iron oxide core syntheses. For ligand exchange, an incoming ligand molecule will need to bind more strongly to the inorganic NP surface than the existing (surfactant) ligand present from synthesis. Oleic acid is a common example of a surfactant ligand that is usually exchanged. Ligand exchange with small molecule ligands may be necessary to obtain particles with a specific size or functionality[77,78].

With the ligand exchange strategy, ligands stabilizing the NPs in the initial solvent phase used for synthesis can replaced by other, more strongly binding ligands that allow transfer to a second phase and provide colloidal stability there, e.g. by exchanging hydrophobic ligands by hydrophilic ones to allow colloidal stability in the aqueous phase[79]. Commonly used ligand molecules include thiol groups that bind strongly to inorganic surfaces of NPs[80–82]. Iron oxide MNPs are hydrophobic and surface functionalisation with oleic acid is a common procedure for stabilising MNPs in the aqueous phase for size analysis, or with phosphines for highly concentrated MNP dispersions[83,84].

Ligand modification is used to ensure the stable functionalisation of the MNP in different phases. Ligand modification involves the modification of a ligand already present on the MNP surface; the surface hydroxyl groups on iron oxide for example. The ligand molecule stabilizing the MNPs in the original first phase is rendered hydrophilic or hydrophobic to transfer and stabilise the MNPs into the second phase. Modification of the initial surface ligands is a general way to make NPs compatible with specific macromolecular ligands[85]. For example, hydrophilic NPs stabilised by a mercaptocarboxylic acid via ligand exchange can be modified by a hydrophobic molecule that is chemically bound to its carboxylic terminal groups[86].

Ligand modification can be used to facilitate efficient phase transfer after a ligand exchange step if necessary. Many surface chemistries will not bind strongly to the iron oxide surface, meaning ligand exchange is performed first to form a covalent linkage with the surface that can then be modified further. This modification can take place in the initial phase, but is then transferred to the desired phase for application. The subsequent chemistry must share some of the same characteristics as the original ligand for modification to take place.

An example of this is seen in a study by Ninjbadgar et al.[50], whereby iron oxide particles were first functionalised by an aminosilane (3-glycidyloxypropyltrimethoxysilane, GLYMO) through ligand exchange. However, these MNPs are dispersible in water, so ligand modification was necessary and the ligand selected was PEG. The GLYMO ligand was modified by a base catalysed epoxy ring opening with an amine terminated polymer in tetrahydrofuran (THF). The resulting PEG-MNPs were extracted and dispersed in H_2O.

Another strategy for phase transfer is the addition of a molecular layer to the original ligand by covalent linkage to change surface properties. A common example of this is the silanization of MNPs to improve stability and allows the magnetic moment to be maintained[87,88]. This silianization results in a ligand bilayer that can transfer hydrophobic MNPs from the aqueous phase to organic solvents, or hydrophobic MNPs to water[89,90]. Silanization comprises of a ligand modification process in which an initial silane layer is covalently bound to the NP surface, through a covalent linkage with the surface hydroxyl groups or a residual surfactant present from synthesis.

A common reagent used to achieve this is 3-aminopropyl triethoxylsilane (APTES) where hydrolysed silanol groups react with the surface hydroxyl groups of the iron oxide core leading to a surface silanization[91]. Then, using this first layer, a polymeric, crosslinked inorganic silica shell can be deposited on the NP surface, which can be further derivatized depending on the desired application. A cross coupling between ligands is used after the initial ligand exchange so as to provide a covalent bridge surrounding the particles through covalent linkage of silanol bonds. Silica can be used to increase the mechanical strength of non-metallic NPs or as a contrast agent in MRI are some typical examples. In all of these cases, the use of the pure inorganic material might be problematic because it is not trivial to achieve the desired colloidal stability or biocompatibility. Encapsulation of the inorganic particles in a polymeric material can help to overcome these problems.

1.4.2 Surface chemistries for biomedical applications

1.4.2.1 Polymers

Polymers are commonly used to functionalise MNPs for biomedical applications. Many polymers have excellent biocompatibility, low toxicity and good biodegradability[92,93]. Polymers can be split into natural and synthetic, whereby the choice of which is often balanced by a trade-off between biocompatibility and thermal or chemical stability (Figure 1.7)[94]. Dextran is a highly biocompatible and biodegradable neutral bacterial polysaccharide with simple repeating glucose subunits and hydrophilic properties[95,96]. It has a high water solubility and shows little toxicity to human cells[96]. It has been used as a surface functionalisation molecule in several biomedical applications due to its aqueous solubility, biocompatibility, biodegradability, wide availability, ease of modification and non-fouling properties[97]. Dextran as a surface functionalisation of a MNP will endow a slightly negative ζ_p of -17 mV[97].Dextran’s are commonly employed for MNP coating because of their affinity for the iron oxide surface through chelation and hydrogen bonding[98]. It is often used as an alternative to PEG functionalisation to minimise NP interactions with their environment. The functionalisation of dextran onto magnetite cores is a facile process, where dried dextran is added to magnetite MNPs in water and sonicated to ensure homogeneous surface functionalisation[99,100].

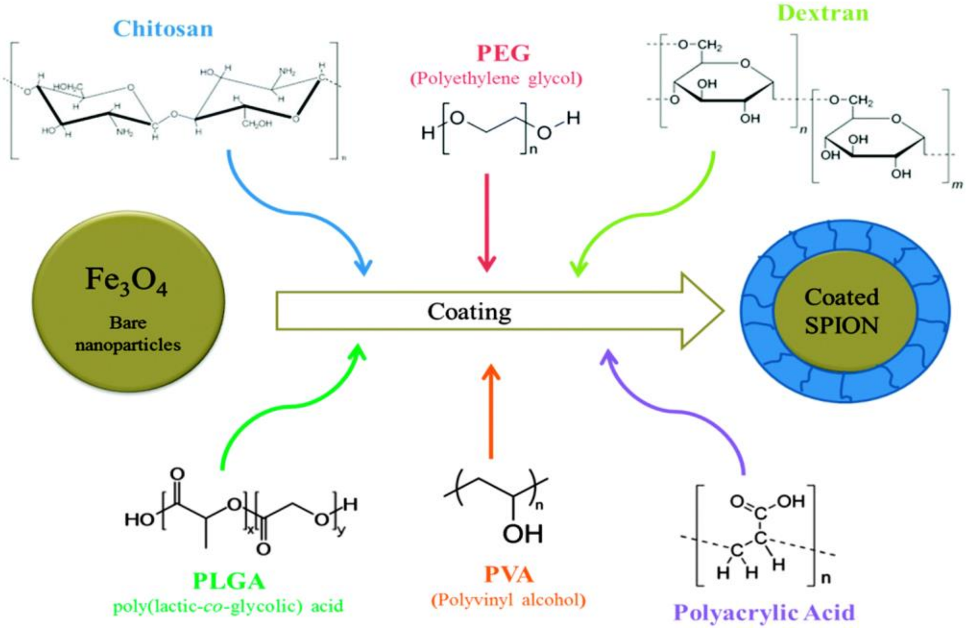

Figure 1.7 Iron oxide cores can be functionalised with various polymers including PEG, PVA and dextran are common choices for biomedical studies due to their biocompatibility[94].

Synthetic polymers such as PEG, PVA and poly-L-lactic acid (PLA) have also been used to functionalise MNPs[101–103]. PEG, is commonly used for surface modifications in biomedical applications due to its relatively high stability, water solubility, and low immunogenicity[104,105]. PEG is a hydrophilic linear polymer consisting of repeating units of $–CH_2–CH_2–O–$. The chain length is essential to resisting bio-fouling, but increasing PEG chain length will also increase d_{hyd}, and so there is a trade-off between chain length and MNP size. PEG-MNPs are sterically stabilised whereby incoming molecules are sterically repulsed and cannot penetrate the hydrated PEG layer[106,107]. As such, PEG functionalisation of MNPs results in inert hydrophilic surfaces with low non-specific interactions and grants resistance to bio-fouling. PEG can be functionalised to MNPs in a number of ways, a common method is to carry out the functionalisation process in situ in a co-precipitation method[108]. Before the pH is increased by the addition of a base, the PEG polymer is added to the salts. Upon crystallisation of the iron, the change in pH will protonate the hydroxyl groups present on the surface of the iron oxide, this is then attached to the hydroxyl terminated PEG via covalent bonds.

1.4.2.2 Biomolecules

The conjugation of biomolecules, such as antibodies, aptamers and proteins, to inorganic NPs generates hybrid materials that can be used to allow the NPs interact specifically with biological systems. NP–biomolecule conjugates can bring together the unique properties and functionality of both materials, e.g. fluorescence or magnetic moment of inorganic NP and the functionality imparted by the biomolecules e.g. highly specific binding of a target by molecular recognition. Approaches for the conjugation of biomolecules to NPs generally fall under three concepts[67] – firstly, ligand-type binding to the surface of the NP, electrostatic adsorption of biomolecules to NPs and covalent binding by conjugation chemistry by exploiting and modifying functional groups on both the NPs and the biomolecules.

Biotin vitamin is an example of a biomolecule using for functionalisation of MNPs, known for its part in the biotin-avidin affinity-based system[109,110]. Biotin will not bind to the iron oxide core strongly in a direct manner, and so is often linked to the MNP via a polymer chemistry such as PEG. This PEG is amine terminated that will interact with amine terminated proteins/peptides like biotin to form stable amide bonds. PEG eliminates the common issues of aggregation with biotinylated proteins and antibodies[111]. The PEG spacer makes the biotin freely available for biocapture applications.

1.4.2.3 Chemical functionalisation

There are vast numbers of other chemistries that can be functionalised to the surface of MNPs by a variety of means[112]. An example of a small molecule often used as a surface functionalisation for MNPs is citrate[113]. Sodium citrate can act as both a reducing and a coordinating agent. Free electron pairs in the carbonyl groups can stabilize MNPs electrostatically and act as a coordination agent in compounds with metallic atoms that have free orbitals[114]. The main advantage of the chemical reduction method using citrate is the possibility of subsequent functionalisation and its excellent biocompatibility[115]. Another commonly used functionalisation chemistry is oleic acid. It is used as a capping agent as mentioned previously and to prevent aggregation[116]. It is often the functionalisation of choice for size determination using electron microscopy. This is due to the ease of functionalisation, as it happens during synthesis and has a small footprint[117,118]. The oleic acid covalently binds to the surface of the iron oxide. The addition of oleic acid neutralizes the surface of the MNP (-OH groups) to provide stability.

Another example of a chemical functionalisation is zwitterionic chemistry. These groups possess the greatest polarity found within the non-ionic class of hydrophilic groups. Zwitterions are molecules with a positive and negative electrical charge but can have a net charge of zero depending on environmental conditions (pH). Due to its electrical charges, a zwitterion will be highly soluble in water and organic solvents. When a zwitterion is dissolved in water, the hydrogen atoms in water immediately surround the negatively charge, and the oxygen atoms surround the positive charge of the ion.

Common zwitterionic groups used are amino acids, carboxybetaines, phospholine and sulphobetaines. In a study by Wei et al.[119], compact zwitterion-functionalised MNPs were examined for their viability in biological applications. The dopamine sulphonate (DS) ligand used was designed with three characteristics in mind (Figure 1.8). Firstly, the dopamine moiety provides strong coordination to the iron oxide surface via covalent bonds. Then the sulphonate group offers high water solubility. Finally, the combination of the quaternary amine group and the sulphonate group provides the ligand with a zwitterionic character, enabling pH stability and decreasing non-specific interactions with proteins.

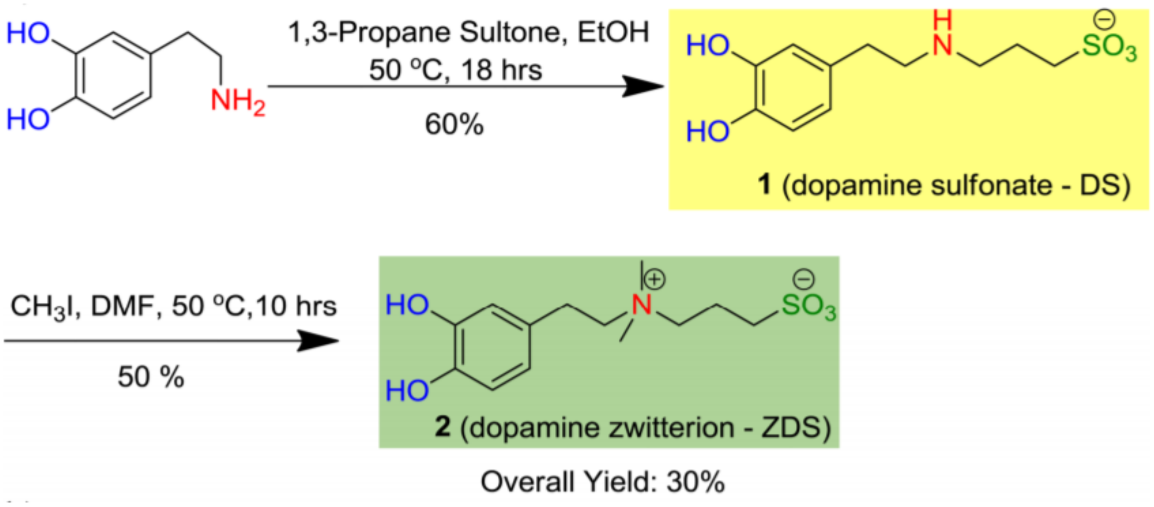

Figure 1.8 Chemical structure and synthesis route to DS and the zwitterionic DS ligand[119].

Another common surface chemistry used to functionalise NPs is boronic acid (BA)[120]. Its binding affinity for diol groups can be used in biocapture or biosensing applications.

BA does not bind strongly to metals, so ligand modification is often used to overcome this limitation. A common approach is to covalently attach amine-based BAs (aminophenylBA for example) through epoxide chemistry[58,120] where the silane surface functionalisation is modified by the opening of the epoxy ring by the amine terminated BA. Diol groups that BA has affinity for includes sugars, steroids and catecholamines[121–124]. A more detailed insight into the behaviour and characteristics of BA-functionalised MNPs is given in Chapter 5.

1.5 Magnetophoresis of magnetic nanoparticles

The term magnetophoresis describes the behaviour of a MNP moving through a medium of defined viscosity under the influence of an external magnetic field[34]. Magnetophoresis under optimised conditions can be highly specific and highly sensitive to applied magnetic fields. It has applications in magnetic separation, drug delivery and biosorting[125]. The use of the term magnetophoresis has been limited to time-independent magnetic fields. The concept of magnetophoretic motion has not been widely recognised due to the complex specifics of the magnetic dipole-field interaction such as strong dependence on position[126], that make it difficult to observe and to control exactly how the MNP moves in the magnetic field[127]. How MNPs move in a magnetic field depends on their properties; particle size, magnetic susceptibility, chemical composition of the surrounding medium and the strength of the applied magnetic field[125,128]. The motion of MNPs in different hydrogels in magnetic fields is of interest[129,130], to study magnetophoretic motion behaviour for application in biological tissue[131,132].

Several forces influence the magnetophoretic motion of MNPs. As mentioned earlier the magnetic force ($F_{m)}$ is the force applied by the external magnet on the MNPs as they move in the field. The drag force (F_D) is another relevant force that acts opposite to the relative motion of the MNP with respect to the surrounding fluid. Inter-particle forces must be repulsive in nature to have independent MNPs, free from aggregation. When these repulsive forces weaken or become attractive, particles aggregate and influence magnetophoretic motion[55]. By selectively controlling each of these forces, it is possible to control the magnetophoretic transport of MNPs[56]. Controlled transport can be challenging for colloidally stable suspensions because of the magnetic, viscous drag, and Brownian motion and rotation (how Brownian motion can cause the rotation of a particle) scale differently with particle size as they interact with the medium[134].

There are some critical challenges in studying the magnetophoretic transport behaviour of MNPs. These include applying sufficient magnetic force to induce motion and having a precise method to track MNP position with respect to time, so as to measure velocities. The first challenge has been discussed in relation to creating a strong enough F_m ($>F_D$). F_M is defined by the strength of the external magnetic field and the gradient with respect to MNP position. Typical magnets used are rare metal neodymium magnets because of their strong magnetic fields and large magnetic field gradients over a range of ~10 cm. In order to measure velocity, MNP position should be measured accurately and precisely over time. In a study by Lim at al.[32], dark field optical microscopy was used to observe the plasmonic scattering of individual MNPs (d_{hyd} 100 nm) as they moved within water under the combined influence of magnetic, viscous drag, and Brownian forces. The magnetic field was induced by a single magnetic tip present at the wall of the microfluidic chamber. The magnetic tip was able to capture and release MNPs in a tweezer like effect. The trajectories of individual MNPs were analysed quantitatively to differentiate the effects of the forces and revealed the requirements for magnetic manipulation of nanoparticles within microfluidic devices or living cells. The magnitude of the forces acting on the MNPs was quite small, this technique also established a method for the detection of tiny forces such the binding events of molecular species attached to the NPs.

A recent study by Sun et al.[135], on the magnetophoresis of MNPs in water was studied using coupled particle-fluid modelling and dye-tracing experiments. Both the direction and speed of the MNPs was studied. Bare iron oxide MNPs were used in this study, where the water medium contained methylene blue dye. The positively charged dye was attracted to the MNP surface due to its negative surface charge. To perform the dye-tracing experiments, a plastic cuvette was filled with water/methylene blue mixture and was placed on the surface of a magnet. The MNPs were then added. The position of the MNPs were tracked over time by digital imaging and analysed by computational models. It was found that the MNPs did not follow a straight path towards the magnet, but rather circulated in a convectional manner before moving towards the magnet (Figure 1.9).

This was concluded to be due to displacement of fluid as the MNPs moved in response to the external magnetic field. These experiments demonstrated that particle-fluid interactions and magnetophoresis of the MNP plays an important role in affecting the kinetics of carrier fluid. It was also found that the higher the concentration of MNPs used, the more violent the displacement of fluid. This is important to note, as although the MNPs were superparamagnetic and assumed to be acting independently, concentration was demonstrated to affect their magnetophoresis through the fluid medium.

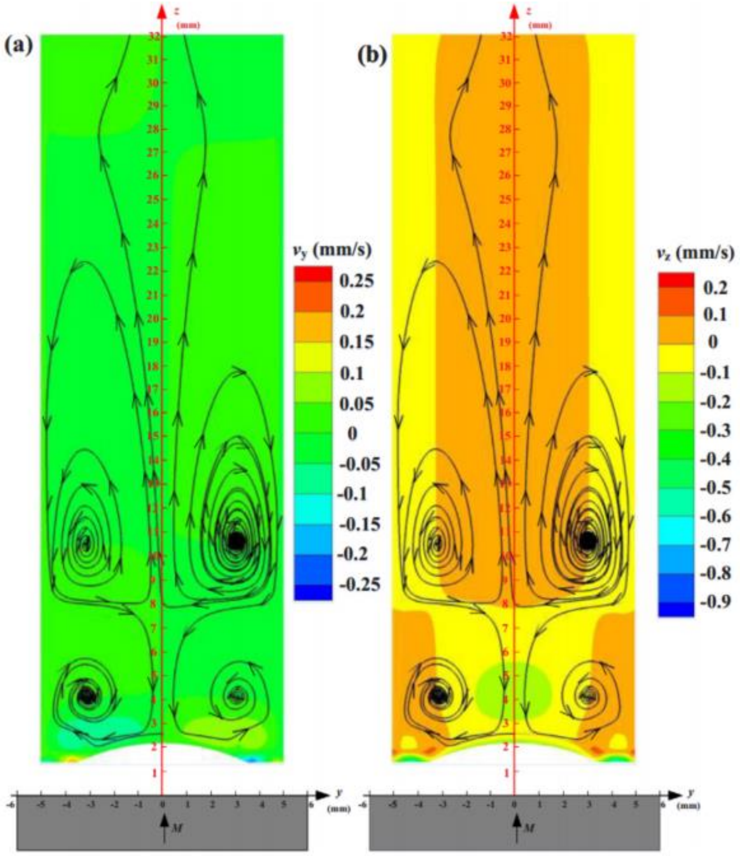

Figure 1.9 Detailed mapping of the movement patterns of MNPs in fluid under the influence of an external magnetic field[135]. Magnet is shown underneath the cuvette inducing motion.

A recent study in 2016 by Garraud et al.[136], examined the use of a small permanent magnet to capture and retain MNPs from a synovial fluid mimic. Iron oxide MNPs (d_{hyd} 8.5 ± 1.5 nm) were embedded in a polystyrene matrix with a fluorescent dye attached. The medium used was a mixture of water and glycerol to mimic the viscosity of the synovial fluid over the expected range. A neodymium N52 magnet was used for these experiments. Computational modelling combined with video was used to track the MNPs. The study showed results that were in broad agreement with equation 1.9, the balance between F_M and F_D led to velocities of 0.5-800 μm/s depending on viscosity. It is stated that these velocities agreed strongly with their numerical model.

To enhance magnetophoretic transport for biomedical applications for drug delivery for example, greater control is needed. This has led to some studies developing new methods of magnetic guidance, one such example is by Liu et al.[137], whereby two oppositely polarized magnets were used to enhance magnetophoretic transport in deep tissue. This is in contrast to the one magnet used in most magnetophoretic transport studies, one magnet is used as it is easier to guide the MNPs to a specific point. In this study, two separate circular neodymium magnets with a field strength of 0.67 T were placed 16 mm apart, creating equal pull in both directions at the centre point. An agarose gel (0.4% w/v) was placed in the centre and 100 nm PEG-polyacrylate (PCA) functionalised MNPs were deposited on the surface. This study did detailed analysis of the field gradient in both directions. It was found that the gradient changes after certain distances have been reached, the change in gradient is not gradual as it is dependent on the field lines exerted from the magnet face. This dual magnet system enabled equal distribution in both directions with an increased susceptibility ($\chi = 0.722$) due to the concentric magnetic field gradients.

It is also possible to combine different magnets to induce magnetophoretic transport into tissue by permanent and alternating field gradients. A study by Jafari et al.[138], used a permanent magnetic field generated from a neodymium magnet (0.8 T) and an alternating field generated from a pair of electromagnets (100 Hz) to induce magnetophoretic transport in cartilage of a cow knee joint (Figure 1.10). PEG-MNPs (d_{hyd} 30 nm) were placed on the surface and guided through the knee joint for 40 min. Magnetophoretic transport was measured under permanent field only and compared with the combined fields. Combined application of an alternating magnetic field and the static field gradient resulted in a nearly 50 times increase in MNP transport in bovine articular cartilage tissue as compared with static field conditions.

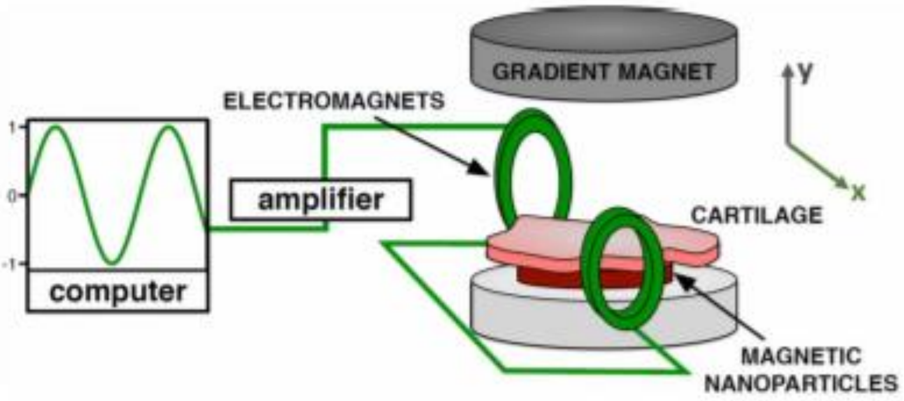

Figure 1.10 Experimental setup for MNP delivery experiments[138].

1.5.1 Magnetophoretic transport studies in vitro

Some magnetophoretic studies have focused on comparing experimental and theoretical rates of magnetophoretic motion in hydrogels and tissue via digital imaging. Using equation 1.9, discussed in the previous section, it is possible to calculate the theoretical velocity at which a MNP should travel towards magnet in an external magnetic field in a viscous medium. A study by Kuhn et al.[30], focused on theoretically calculating the velocity at which MNPs migrated through a viscous medium and compared it to their experimental measurements. In this study, PEG and silica-MNPs were used with d_{hyd} ranging from 135 nm to 400 nm. MNP transport was studied through ECM medium and measured using digital imaging. The ECM medium was a 1:1 mixture of ECM to Dulbecco's modified medium (η = 380 cP). The magnetic field gradient was mapped by a Hall Probe, to enable a detailed understanding of the effect of the magnetic field on the MNP at any distance. A theoretical velocity range was predicted for all functionalised MNPs used (0-2.8 mm/h). Their measured experimental velocity values of 1.5 (PEG, d_{hyd} 145 nm), 0.27 (Silica, d_{hyd} 135 nm) and 0.15 mm/h (PEG, d_{hyd} 400 nm) fell within their predicted velocity range.

A similar approach was used by Holligan et al.[7], where magnetophoretic transport of bare iron oxide MNPs were studied. Agarose gel was used as a mimic for the vitreous body of the eye (Figure 1.11). An equation similar to equation 1.9 was used to predict MNP theoretical velocity in agarose[30]. In this case, the agarose was treated as a biphasic medium (due to agarose fibres binding by hydrogen bonding to form the network, leaving water filled pores between these bound fibres), thus a porosity factor (φ, 0.2) was included to account for this. The viscosity parameter in equation 1.9 was that of water given that this was the phase of the agarose within which the MNPs were transported. A theoretical velocity of 0.468 mm/h was calculated for the bare iron oxide MNPs. To measure velocity experimentally, the MNP were pulled through the agarose whereby the front position was tracked over time and an experimental velocity of 0.277 mm/h was measured. Their experimental values differed by approx. 100% when compared to the theoretical velocity.

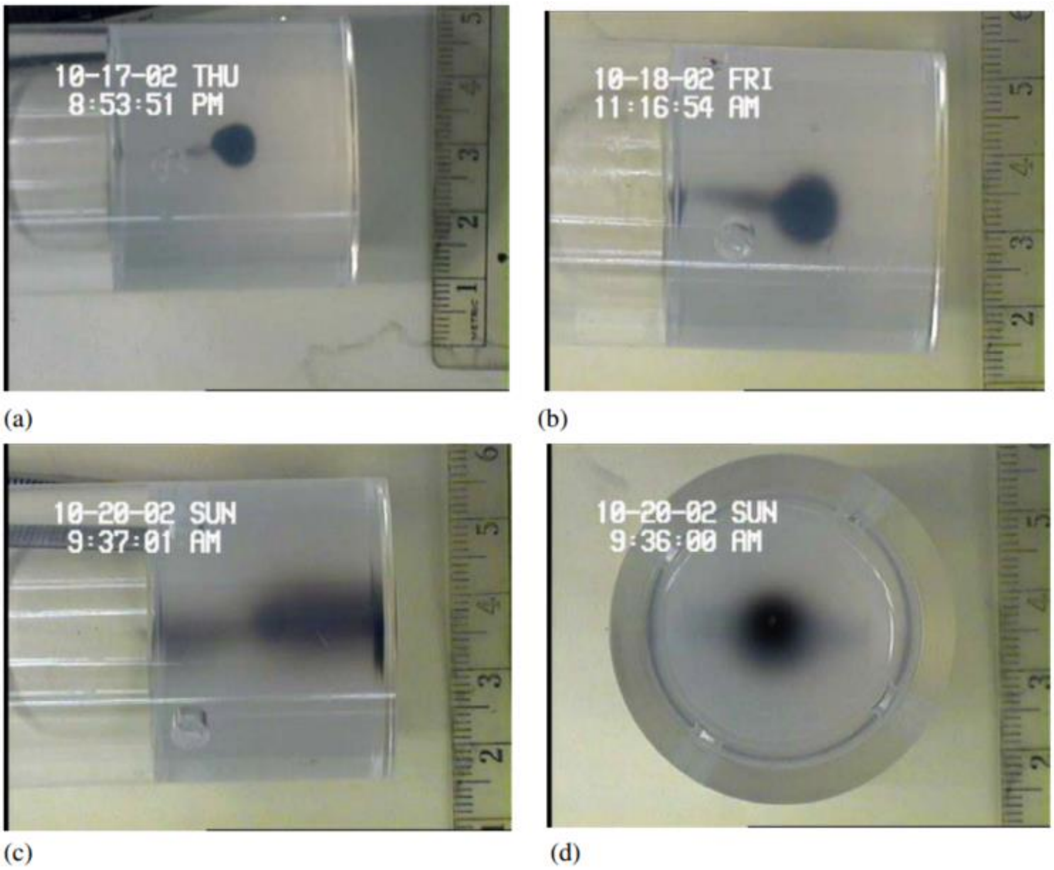

Figure 1.11 Experimental setup showing MNPs movement through the agarose towards an external magnet over a period of three days[7]. The MNPs were injected into the agarose centre via a needle (a), the MNPs were then imaged 14 h later (b), and again 72 h later (c), (d).

In a publication by Kulkarni[128], MNP motion is investigated in liver, kidney and brain tissue. Four different surface chemistries were investigated. The chemistries used were PEG, chitosan, starch and lipid. The motion was measured in two ways, the particles were allowed to passively diffuse into the tissue and the particles were guided through the tissue via a magnet placed directly under the tissue. MNPs with a positive zeta potential (ζ_p) moved faster through the tissue than MNPs with a negative ζ_p, due to the positive charge keeping particles from aggregating and preventing interactions with the tissue. Chitosan-MNPs moved most effectively through all three-tissue types (as compared to starch, lipid, and PEG particles). They indicate that MNP motion in tissue is complex and that additional studies are required to elucidate transport mechanisms.

Another method being investigated is the use of functionalised MNPs for transdermal delivery of anti-cancer agents via hair follicles[138] (Figure 1.12). A model anti-cancer agent, epirubicin (EPI) was then functionalised onto MNPs surface through covalent linkage. The MNPs had a d_{hyd} of 10 nm and a negative surface charge of – 27 mV in water. The EPI-MNPs composite exhibited magnetic responsiveness with a saturation magnetisation intensity of 77.8 emu g^{-1}. Transdermal studies demonstrated that the EPI-MNP composites penetrated deep inside the skin. The magnetic field-assisted MNP transdermal vector can circumvent the stratum corneum via follicular pathways. The study indicates the potential of a MNP-based vector for feasible transdermal therapy of skin cancer.

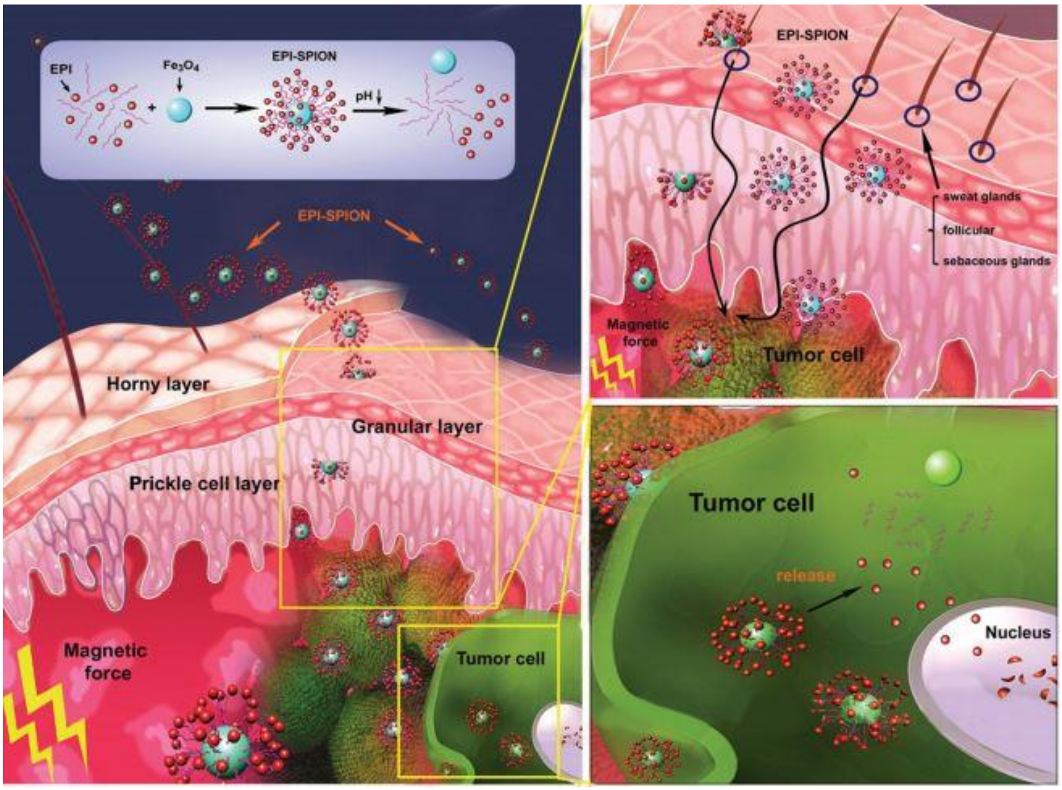

Figure 1.12 Graphic concept of the EPI-MNPs penetrating the skin to gain access to the target tumours.

1.6 Conclusion

The need for precise control over MNP synthesis is still being studied, adapted and improved. The unique properties of superparamagnetic NPs mean they are applicable for biocapture, drug delivery, hyperthermia and as contrast agents for MRI. The surface functionalisation used to protect the magnetic core is always striving to improve their biocompatibility, cellular uptake and stability. By tailoring the characteristics of the MNPs, it is possible to control their interactions, stability and loading capacity. The surface functionalisation can be tailored to specifically target biomarkers within a specific area and be guided by an external magnetic field. There are still many challenges for using MNPs for in vivo applications.

There are currently limitations in the understanding of magnetophoretic transport mechanisms of MNPs, particularly through biological media such as human tissue. By gaining a detailing understanding of how MNPs move through and interact with biological media such as the ECM, it will be possible to predict interactions and behaviours of MNPs in-vivo and optimize MNPs and surface chemistries for specific in-vivo transport applications. Immune system recognition, aggregation and extraction are the main challenges being researched today regarding the use of MNPs in biomedical applications. While there is a small body of work focussing on the transport of MNPs in-vitro and in-vivo, more research is needed to understand how the physical and biochemical nature of the in-vivo environment in particular influences MNP magnetophoretic motion.

1.7 Thesis outline

The purpose of this work is to develop and apply a method to track and predict magnetophoretic transport and behaviour in tissue for biomedical applications. This thesis proposes using digital imaging to track MNP fronts through hydrogels used as mimics for the ECM as well as through cultured ECM. Electrostatic, physical and chemical MNP properties and their interactions with these environments are investigated to allow for a better understanding of MNP motion in ECM.

Chapter 2 reports on the development of an imaging method used in the thesis to experimentally track and calculate magnetophoretic transport of MNPs through agarose gel. Synthesis and characterisation of iron oxide cores and subsequent functionalisation's were compared and optimised for magnetophoretic studies. MNPs were functionalised with PEG and had their experimental velocities calculated based on the MNP front position obtained over time as they migrated through agarose under the influence of an external magnetic field. The conditions of the magnetophoretic experiments were studied and optimised. Finally, MNPs with other surface functionalisation chemistries were investigated in the magnetophoretic setup and it was observed that different experimental velocities were observed for different surface chemistries.

Chapter 3 focuses on understanding the effect of MNP surface chemistry on magnetophoretic transport as they were transported through agarose. MNPs were functionalised with neutral PEG, negatively charged citrate and positively charged arginine. The ionic environment of the agarose gel was manipulated to monitor its impact on the different MNP velocities. Both MNP surface charge and the ionic content of the agarose environment were shown to impact magnetophoretic velocity. These new findings are explained in the context of a known enrichment exclusion effect used to explain nanofluidic behaviour of charged particles in the literature. Theoretical calculations of magnetophoretically-induced velocity, based on an existing equation in the literature were shown not to account for this new observation.

Chapter 4 focuses on investigating magnetophoretic transport in more advanced tissue mimics, collagen/agarose hydrogels and cultured ECM. Collagen was combined with agarose and synthetic interstitial fluid was used an aqueous phase within the gels. These agarose/collagen gels presented hydrophobic behaviour at the gel surface leading to time lags before MNP penetration of the gel. The electrostatics present in the agarose/collagen were in stark contrast to the electrostatics of an agarose gel, the collagen interacted with both charged particles to slow velocity. Cultured ECM was also investigated for magnetophoretic studies. All functionalised MNPs were able to be magnetophoretically guided through the ECM at lower velocities when compared to the agarose-based gels due to a significantly more complex environment. The impact of a significantly stronger magnetic field than previously used was also investigated. It was found to change the path taken by MNPs and ignore electrostatic influences observed in Chapter 3 under certain conditions.

Chapter 5 investigated the capture of glucose by BA-MNPs from hydrogels and cultured ECM. ζ_p measurements of the BA-MNPs were used to track ionisation state of the BA-MNPs as a function of pH as well as binding of cis-diols. Magnetophoretic experiments in agarose were carried out in the presence and absence of glucose to investigate the effect of glucose uptake on transport. Finally, a method was developed to quantify glucose content in agarose and cultured ECM using BA-MNPs for glucose extraction and a subsequent enzyme assay for quantification. The method was found to have a limit of detection (LOD) of 0.72 ppm and was reproducible over a physiological range of glucose in tissue and blood.

1.8 References

1. Strambeanu, N., Demetrovici, L., Dragos, D. & Lungu, M. Nanoparticles: Definition, Classification and General Physical Properties. in Nanoparticles' Promises and Risks: Characterization, Manipulation, and Potential Hazards to Humanity and the Environment 3–8 (2015).
2. De, M., Ghosh, P. S. & Rotello, V. M. Applications of Nanoparticles in Biology. *Adv. Mater.* **20**, 4225–4241 (2008).
3. Cho, K., Wang, X., Nie, S., Chen, Z. (Georgia) & Shin, D. M. Therapeutic Nanoparticles for Drug Delivery in *Cancer. Clin. Cancer. Res.* 14, 1310–1316 (2008).
4. McNamara, K. & Tofail, S. A. M. Nanoparticles in Biomedical Applications. *Adv. Phys.: X* **2**, 54–88 (2017).
5. Gao, J., Gu, H. & Xu, B. Multifunctional Magnetic Nanoparticles: Design, Synthesis, and Biomedical Applications. *Accounts Chem. Res.* **42,** 1097–1107 (2009).
6. Pankhurst, Q. A., Connolly, J., Jones, S. K. & Dobson, J. Applications of Magnetic Nanoparticles in Biomedicine. *J. Phys. D: Appl. Phys.* **36**, R167–R181 (2003).
7. Holligan, D. L., Gillies, G. T. & Dailey, J. P. Magnetic Guidance of Ferrofluidic Nanoparticles in an In Vitro Model of Intraocular Retinal Repair. *Nanotechnology* **14**, 661 (2003).
8. Châtel, P. F. de, Nándori, I., Hakl, J., Mészáros, S. & Vad, K. Magnetic Particle Hyperthermia: Néel Relaxation in Magnetic Nanoparticles under Circularly Polarized Field. *J. Phys.: Condens. Matter,* **21**, 124202 (2009).
9. Assa, F. et al. Chitosan Magnetic Nanoparticles for Drug Delivery Systems. *Crit. Rev. Biotechno.* **37**, 492–509 (2017).
10. Al Faraj, A., Shaik, A. P. & Shaik, A. S. Effect of Surface Coating on the Biocompatibility and In Vivo MRI Detection of Iron Oxide Nanoparticles after Intrapulmonary Administration. *Nanotoxicology.* **9**, 825–834 (2015).
11. Morrish, A. H. "The Magnetic Field," in *The Physical Principles of Magnetism*, Michigan: IEEE Press, 1-30 (2001)
12. Siegman, H. & Stohr. J. "Electric Fields, Currents and Magnetic Fields" in *Magnetism*. 1st edn. Berlin: Springer Verlag. 39-60 (2006).
13. Bozorth, R. M. "Factors Affecting Magnetic Quality" in *Ferromagnetism*. 1st edn. New Jersey: IEEE Press. 14-47 (1993).
14. Lee, J. G., Li, P., Dong, X. L. & Choi, C.J. Fabrication of Ferromagnetic Mn-Al Alloy Nanoparticles Using a Plasma Arc-discharge Process. *Thin Solid Films*, **519**, 81-85, (2010).
15. Forrester, M. & Kusmartsev, F. The Nano-Mechanics and Magnetic Properties of High Moment Synthetic Antiferromagnetic Particles. *Phys. Status Solidi (a)* **211**, 884–889 (2014).
16. Deissler, R. J., Wu, Y. & Martens, M. A. Dependence of Brownian and Néel Relaxation Times on Magnetic Field Strength. *Med. Phys*. **41**, 012301 (2014).
17. Rikken, R. S. M. et al. Manipulation of Micro- and Nanostructure Motion with Magnetic Fields. *Soft Matter* **10**, 1295–1308 (2014).

18. Shevkoplyas, S. S., Siegel, A. C., Westervelt, R. M., Prentiss, M. G. & Whitesides, G. M. The Force Acting on a Superparamagnetic Bead Due to an Applied Magnetic Field. *Lab Chip* **7**, 1294–1302 (2007).
19. Tu, L. et al. Measurement of Brownian and Néel Relaxation of Magnetic Nanoparticles by a Mixing-Frequency Method. *IEEE Transactions on Magnetics*. **49**, 227–230 (2013).
20. Marghussian, V. Magnetic Properties of Nano-Glass Ceramics. *Nano-Glass Ceramics*, 181–223 (2015).
21. Shah, S. A., Reeves, D. B., Ferguson, R. M., Weaver, J. B. & Krishnan, K. M. Mixed Brownian Alignment and Néel Rotations in Superparamagnetic Iron Oxide Nanoparticle Suspensions Driven by an AC Field. *Phys. Rev. B. Condens. Matter. Mater. Phys*. **92**, (2015).
22. Singh, N., Jenkins, G. J. S., Asadi, R. & Doak, S. H. Potential Toxicity of Superparamagnetic Iron Oxide Nanoparticles (SPION). *Nano. Rev.* **1**, (2010).
23. Aurich, K., Schwalbe, M., Clement, J. H., Weitschies, W. & Buske, N. Polyaspartate Coated Magnetite Nanoparticles for Biomedical Applications. *J. Magn. Magn. Mater.* **311**, 1–5 (2007).
24. Adawi, H. Surface Effect Of Ferromagnetic Nanoparticles On Transition Between Single- And Multi-Domain Structure Or Between Single-Domain Structure And Superparamagnetic Phase. (Master's Thesis). Wright State University, Ohio. (2016).
25. Biehl, P., Von der Lühe, M., Dutz, S. & Schacher, F. H. Synthesis, Characterization, and Applications of Magnetic Nanoparticles Featuring Polyzwitterionic Coatings. *Polymers*. **10**, 91 (2018).
26. Saif, S., Tahir, A. & Chen, Y. Green Synthesis of Iron Nanoparticles and Their Environmental Applications and Implications. *Nanomaterials*. **6**, (2016).
27. Hadjipanayis, C. G. et al. Metallic Iron Nanoparticles for MRI Contrast Enhancement and Local Hyperthermia. *Small*, **4**, 1925–1929 (2008).
28. Wang, C. et al. Heusler Nanoparticles for Spintronics and Ferromagnetic Shape Memory Alloys. *J. Vac. Sci. Technol., B,* **32**, 020802 (2014).
29. Zborowski, M., Fuh, C. B., Green, R., Sun, L. & Chalmers, J. J. Analytical Magnetophoresis of Ferritin-Labeled Lymphocytes. *Anal. Chem*. **67**, 3702–3712 (1995).
30. Kuhn, S. J., Hallahan, D. E. & Giorgio, T. D. Characterization of Superparamagnetic Nanoparticle Interactions with Extracellular Matrix in an In Vitro System. *Ann. Biomed. Eng.* **34**, 51–58 (2006).
31. Urbach, A. R., Love, J. C., Prentiss, M. G. & Whitesides, G. M. Sub-100 nm Confinement of Magnetic Nanoparticles Using Localized Magnetic Field Gradients. *J. Am. Chem. Soc.* **125**, 12704–12705 (2003).
32. Lim, J. et al. Magnetophoresis of Nanoparticles. *ACS Nano.* **5**, 217–226 (2011).
33. Wei, W. & Wang, Z. Investigation of Magnetic Nanoparticle Motion under a Gradient Magnetic Field by an Electromagnet. *J. Nanomater*. **7**, (2018).
34. Zborowski, M. & Chalmers, J. J. Magnetophoresis: Fundamentals and Applications. Wiley *Encyclopaedia of Electrical and Electronics Engineering* 1–23 (2015).

35. Darezereshki, E. Synthesis of Maghemite (γ-Fe2O3) Nanoparticles by Wet Chemical Method at Room Temperature. *Mater. Lett*., **64**, 1471–1472 (2010).
36. Kefeni, K. K., Msagati, T. A. M., Nkambule, T. T. I. & Mamba, B. B. Synthesis and Application of Hematite Nanoparticles for Acid Mine Drainage Treatment. *J. Environ. Chem. Eng.* **6**, 1865–1874 (2018).
37. Stankic, S., Suman, S., Haque, F. & Vidic, J. Pure and Multi Metal Oxide Nanoparticles: Synthesis, Antibacterial and Cytotoxic Properties. *J. Nanobiotechnology.* **14**, (2016).
38. Si, S. et al. Size-Controlled Synthesis of Magnetite Nanoparticles in the Presence of Polyelectrolytes. *Chem. Mater.* **16**, 3489–3496 (2004).
39. Gul, S., Khan, S. B., Rehman, I. U., Khan, M. A. & Khan, M. I. A Comprehensive Review of Magnetic Nanomaterials Modern Day *Theranostics. Front. Mater*. **6**, (2019).
40. Asoufi, H. M., Al-Antary, T. M. & Awwad, A. M. Green Route for Synthesis Hematite (α-Fe2O3) Nanoparticles: Toxicity Effect on the Green Peach Aphid, Myzus Persicae (Sulzer). *Environ. Nanotech. Monit. Manag.* **9**, 107–111 (2018).
41. Kumar, R., Inbaraj, B. & Chen, B.-H. Surface Modification of Superparamagnetic Iron Nanoparticles with Calcium Salt of Poly(γ-glutamic acid) as Coating Material. *Mater. Res. Bull.* **45**, 1603–1607 (2010).
42. Wu, L., Mendoza-Garcia, A., Li, Q. & Sun, S. Organic Phase Syntheses of Magnetic Nanoparticles and Their Applications. *Chem. Rev.* **116**, 10473–10512 (2016).
43. Massart, R. Preparation of Aqueous Magnetic Liquids in Alkaline and Acidic Media. *IEEE Trans. Magn*. **17**, 1247–1248 (1981).
44. Anbarasu, M., Anandan, M., Chinnasamy, E., Gopinath, V. & Balamurugan, K. Synthesis and Characterization of Polyethylene Glycol (PEG) Coated Fe3O4 Nanoparticles by Chemical Co-Precipitation Method for Biomedical Applications. *Spectrochimica. Acta. Part. A*. **135**, 536–539 (2015).
45. Huber, D. L. Synthesis, Properties, and Applications of Iron Nanoparticles. *Small*. **1**, 482–501 (2005).
46. Petcharoen, K. & Sirivat, A. Synthesis and Characterization of Magnetite Nanoparticles via the Chemical Co-Precipitation Method. *Mater. Sci. Eng: B* **177**, 421–427 (2012).
47. Martínez-Mera, I., Espinosa-Pesqueira, M. E., Pérez-Hernández, R. & Arenas-Alatorre, J. Synthesis of magnetite (Fe3O4) nanoparticles without surfactants at room temperature. Mater. Lett. **61**, 4447–4451 (2007).
48. Sun, S. & Zeng, H. Size-Controlled Synthesis of Magnetite Nanoparticles. J. Am. Chem. Soc. **124**, 8204–8205 (2002).
49. L. E. Euliss, S. G. Grancharov, S. O'Brien,T. J. Deming, G. D. Stucky, C. B. Murray, and G. A. Held. Cooperative Assembly of Magnetic Nanoparticles and Block Copolypeptides in Aqueous Media. *Nano Lett*. **3**, 1489-1493 (2003)
50. Pinna, N. Magnetite Nanocrystals: Nonaqueous Synthesis, Characterization, and Solubility. *ACS publications* **17**, 3044–3050 (2005).
51. Ninjbadgar, T. & Brougham, D. F. Epoxy Ring Opening Phase Transfer as a General Route to Water Dispersible Superparamagnetic Fe3O4 Nanoparticles

and Their Application as Positive MRI Contrast Agents. *Adv. Funct. Mater.* **21**, 4769–4775 (2011).

52. Din, M. I., Raza, M., Hussain, Z. & Mehmood, H. A. Fabrication of Magnetite Nanoparticles (Fe3O4-NPs) for Catalytic Pyrolysis of Nutshells Biomass. *Soft Mater*. **17**, 24–31 (2019).
53. Ma, C., Luo, B., Song, H. & Zhi, L. Preparation of Carbon-Encapsulated Metal Magnetic Nanoparticles by an Instant Pyrolysis Method. *New Carbon Mater*. **25**, 199–204 (2010).
54. Kumfer, B. M., Shinoda, K., Jeyadevan, B. & Kennedy, I. M. Gas-Phase Flame Synthesis and Properties of Magnetic Iron Oxide Nanoparticles with Reduced Oxidation State. *J. Aerosol Sci.* **41**, 257–265 (2010).
55. Rawlings, A. E., Jarrald, R. M., Somner, L. A. & Staniland, S. S. Protein and Peptide-Mediated Synthesis of Magnetic Nanoparticles and Arrays for Biomedicine and Future Data Storage. *Biological Magnetic Materials and Applications*, 95–133, (2018).
56. Glogowski, E., Tangirala, R., Russell, T. & Emrick, T. Functionalization of Nanoparticles for Dispersion in Polymers and Assembly in Fluids. *J. Polym. Sci., Part A: Polym. Chem.,* **44**, 5076–5086 (2006).
57. Baalousha, M. Aggregation and Disaggregation of Iron Oxide Nanoparticles: Influence of Particle Concentration, pH and Natural Organic Matter. *Sci. Total Environ*. **407**, 2093–2101 (2009).
58. Lattuada, M. & Hatton, T. A. Functionalization of Monodisperse Magnetic Nanoparticles*. Langmuir*. **23**, 2158–2168 (2007).
59. Kim, D. K., Zhang, Y., Voit, W., Rao, K. V. & Muhammed, M. Synthesis and Characterization of Surfactant-Coated Superparamagnetic Monodispersed Iron Oxide Nanoparticles. *J. Magn. Magn. Mater*. **225**, 30–36 (2001).
60. T. Pellegrino, L. Manna, S. Kudera, T. Liedl, D. Koktysh, A. L. Rogach, S. Keller, J. Rädler, G. Natile and W. J. Parak. Hydrophobic Nanocrystals Coated with an Amphiphilic Polymer Shell: A General Route to Water Soluble Nanocrystals. *Nano Lett*. **4**, 703-704 (2004).
61. Patel, H.M & Moghimi, S.M. Serum-Mediated Recognition of Liposomes by Phagocytic Cells of the Reticuloendothelial System - The concept of tissue specificity. *Adv. Drug Deliv. Rev.* **32**, 45–60 (1998).
62. Grabbe, S., Landfester, K., Schuppan, D., Barz, M. & Zentel, R. Nanoparticles and the Immune System: Challenges and Opportunities. *Nanomedicine*. **11**, 2621–2624 (2016).
63. Barrán-Berdón, A. L. et al. Time Evolution of Nanoparticle–Protein Corona in Human Plasma: Relevance for Targeted Drug Delivery. *Langmuir.* **29**, 6485–6494 (2013).
64. Rojas, J. M. et al. Time-course Assessment of the Aggregation and Metabolization of Magnetic Nanoparticles. *Acta Biomater.* **58**, 181–195 (2017).
65. Wolfram, J. et al. The nano-plasma interface: Implications of the Protein Corona. *Colloids Surf., B*, **124,** 17–24 (2014).
66. Qu, M. et al. Phase Transfer of Nanoparticles Using an Amphiphilic Ionic Liquid. *Langmuir***, 32**, 13746–13751 (2016).

67. Sperling, R. A. & Parak, W. J. Surface Modification, Functionalization and Bioconjugation of Colloidal Inorganic Nanoparticles. *Philos. Trans. A. Math Phys. Eng. Sci.* **368**, 1333–1383 (2010).
68. Xie, H. et al. Guanidine Cellulose for Biocompatible Nanoparticles Phase Transfer. *Chemistry Select*, **2**, 10555–10558 (2017).
69. Lee, C.-Y., Huang, C.-H. & Wei, G.-T. Behaviors of Ionic Liquids in the Phase Transfer of Aqueous Metal Nanoparticles. *Colloid Surf. A-Physicochem. Eng. Asp.* **367**, 24–30 (2010).
70. Lee, Y. et al. Phase Transfer-Driven Rapid and Complete Ligand Exchange for Molecular Assembly of Phospholipid Bilayers on Aqueous Gold Nanocrystals. *Chem. Commun*. **55**, 3195–3198 (2019).
71. Zakutna, D., Honecker, D. & Disch, S. Phase-Transfer and Stabilization of Highly Monodisperse Ferrite Nanoparticles into Polar Solvents by Ligand Exchange Synthesis. *J. Nanosci. Nanotechnol.* **19**, 5048–5051 (2019).
72. Huehn, J. et al. Selected Standard Protocols for the Synthesis, Phase Transfer, and Characterization of Inorganic Colloidal Nanoparticles. *Chem. Mat*. **29**, 399–461 (2017).
73. Gu, S. et al. A Versatile Strategy for Surface Functionalization of Hydrophobic Nanoparticle by Boronic Acid Modified Polymerizable Diacetylene Derivatives. *Front. Chem.* **7**, (2019).
74. Yang, P. & Zhou, G. Phase Transfer of Hydrophobic QDs for Water-Soluble and Biocompatible Nature Through Silanization. *Mater. Res. Bull.* **46**, 2367–2372 (2011).
75. Yang, P., Ando, M. & Murase, N. Highly Luminescent CdSe/CdxZn1-xS Quantum Dots Coated with Thickness-Controlled SiO2 Shell through Silanization. *Langmuir*. **27**, 9535–9540 (2011).
76. Korpany, K. V. *et al.* One-Step Ligand Exchange and Switching from Hydrophobic to Water-Stable Hydrophilic Superparamagnetic Iron Oxide Nanoparticles by Mechanochemical Milling. *Chem. Commun.* **52**, 3054–3057 (2016).
77. Caragheorgheopol, A. & Chechik, V. Mechanistic Aspects of Ligand Exchange in Au Nanoparticles. *Phys. Chem. Chem. Phys*. **10**, 5029–5041 (2008).
78. Yao, Q., Chen, T., Yuan, X. & Xie, J. Toward Total Synthesis of Thiolate-Protected Metal Nanoclusters. *Accounts Chem. Res*. **51**, 1338–1348 (2018).
79. Lam, T. et al. Fabricating Water Dispersible Superparamagnetic Iron Oxide Nanoparticles for Biomedical Applications through Ligand Exchange and Direct Conjugation. *Nanomaterials,* **6**, (2016).
80. Kluenker, M., Mondeshki, M., Nawaz Tahir, M. & Tremel, W. Monitoring Thiol–Ligand Exchange on Au Nanoparticle Surfaces. *Langmuir* **34**, 1700–1710 (2018).
81. Dewi, M. R., Laufersky, G. & Nann, T. A Highly Efficient Ligand Exchange Reaction on Gold Nanoparticles: Preserving their Size, Shape and Colloidal Stability. *RSC Adv.* **4**, 34217–34220 (2014).
82. López-Lorente, Á. I., Soriano, M. L. & Valcárcel, M. Analysis of Citrate-Capped Gold and Silver Nanoparticles by Thiol Ligand Exchange Capillary Electrophoresis. *Microchim. Acta.* **181**, 1789–1796 (2014).

83. Patil, R. M. et al. Non-Aqueous to Aqueous Phase Transfer of Oleic Acid Coated Iron Oxide Nanoparticles for Hyperthermia Application. *RSC Adv.* **4**, 4515–4522 (2013).
84. Palma, S. I. C. J. et al. Effects of Phase Transfer Ligands on Monodisperse Iron Oxide Magnetic Nanoparticles. *J. Colloid Interface Sci.* **437**, 147–155 (2015).
85. Ling, D., Hackett, M. J. & Hyeon, T. Surface ligands in Synthesis, Modification, Assembly and Biomedical Applications of Nanoparticles. *Nano Today.* **9**, 457–477 (2014).
86. McMahon, J. M. & Emory, S. R. Phase Transfer of Large Gold Nanoparticles to Organic Solvents with Increased Stability. *Langmuir.* **23**, 1414–1418 (2007).
87. Yang, S.-A., Choi, S., Jeon, S. M. & Yu, J. Silica Nanoparticle Stability in Biological Media Revisited. *Sci. Rep.* **8**, 1–9 (2018).
88. Kharisov, B. I. et al. Solubilization, Dispersion and Stabilization of Magnetic Nanoparticles in Water and Non-Aqueous Solvents: Recent Trends. *RSC Adv.* **4**, 45354–45381 (2014).
89. Wang, X. et al. Nanoparticle Ligand Exchange and Its Effects at the Nanoparticle-Cell Membrane Interface. *Nano Lett.* **19**, 8–18 (2019).
90. Daniel, M., Řezníčková, J., Handl, M., Iglič, A. & Kralj-Iglič, V. Clustering and Separation of Hydrophobic Nanoparticles in Lipid Bilayer Explained by Membrane Mechanics. *Sci. Rep.* **8**, 1–7 (2018).
91. Liu, Y., Li, Y., Li, X.-M. & He, T. Kinetics of (3-Aminopropyl)triethoxylsilane (APTES) Silanization of Superparamagnetic Iron Oxide Nanoparticles. *Langmuir*. **29**, 15275–15282 (2013).
92. Han, J. et al. Polymer-Based Nanomaterials and Applications for Vaccines and Drugs. *Polymers*. **10**, 31 (2018).
93. Bohara, R. A., Thorat, N. D. & Pawar, S. H. Role of Functionalization: Strategies to Explore Potential Nano-Bio Applications of Magnetic Nanoparticles. *RSC Adv.* **6**, 43989–44012 (2016).
94. S. Demirer, G., C. Okur, A. & Kizilel, S. Synthesis and Design of Biologically Inspired Biocompatible Iron Oxide Nanoparticles for Biomedical Applications. *J. Mater. Chem. B.* **3**, 7831–7849 (2015).
95. Banerjee, A. & Bandopadhyay, R. Use of Dextran Nanoparticle: A Paradigm Shift in Bacterial Exopolysaccharide Based Biomedical Applications. *Int. J. Biol. Macromol.* **87**, 295–301 (2016).
96. Khalkhali, M. et al. The Impact of Polymer Coatings on Magnetite Nanoparticles Performance as MRI Contrast Agents: A Comparative Study. *Daru*. **23**, (2015).
97. Gracia, R. et al. Synthesis and Functionalization of Dextran-Based Single-Chain Nanoparticles in Aqueous Media. *J. Mater. Chem. B.* **5**, 1143–1147 (2017).
98. Singh, D. et al. Formulation Design Facilitates Magnetic Nanoparticle Delivery to Diseased Cells and Tissues. *Nanomedicine.* **9**, 469–485 (2014).
99. Predescu, A. M. et al. Synthesis and Characterization of Dextran-Coated Iron Oxide Nanoparticles. *R. Soc. Open Sci.* **5**, 171525 (2018).
100. Wasiak, I. et al. Dextran Nanoparticle Synthesis and Properties. *PLOS ONE.* **11**, (2016).

101. Liu, Y. et al. PEGylated FePt@Fe2O3 Core-Shell Magnetic Nanoparticles: Potential Theranostic Applications and In Vivo Toxicity Studies. *Nanomedicine.* **9**, 1077–1088 (2013).
102. Suk, J. S., Xu, Q., Kim, N., Hanes, J. & Ensign, L. M. PEGylation as a Strategy for Improving Nanoparticle-Based Drug and Gene Delivery*. Adv. Drug Deliv. Rev.* **99**, 28–51 (2016).
103. Xiong, F. et al. A Functional Iron Oxide Nanoparticles Modified with PLA-PEG-DG as Tumor-Targeted MRI Contrast Agent. *Pharm. Res.* **34**, 1683–1692 (2017).
104. McBain, S. C., Yiu, H. H. & Dobson, J. Magnetic Nanoparticles for Gene and Drug Delivery. *Int. J. Nanomedicine.* **3**, 169–180 (2008).
105. Zareie, H. M., Boyer, C., Bulmus, V., Nateghi, E. & Davis, T. P. Temperature-Responsive Self-Assembled Monolayers of Oligo(ethylene glycol): Control of Biomolecular Recognition. *ACS Nano.* **2**, 757–765 (2008).
106. Pozzi, D. et al. Effect of Polyethylene Glycol (PEG) Chain Length on the Bio–Nano-Interactions Between PEGylated Lipid Nanoparticles and Biological Fluids: from Nanostructure to Uptake in Cancer Cells. *Nanoscale*. **6**, 2782–2792 (2014).
107. Neamtu, M. et al. Functionalized Magnetic Nanoparticles: Synthesis, Characterization, Catalytic Application and Assessment of Toxicity. *Sci. Rep.* **8**, 6278 (2018).
108. Viswan, A., Chou, H., Sakudo, A. & Nagatsu, M. Bioconjugation Efficiency of Plasma-Functionalized Carbon-Encapsulated Iron Nanoparticles with Biotin–Avidin System. *Biomed. Phys. Eng.***1**, 045104 (2015).
109. Arias, L. S. et al. Iron Oxide Nanoparticles for Biomedical Applications: A Perspective on Synthesis, Drugs, Antimicrobial Activity, and Toxicity. *Antibiotics.* **7**, (2018).
110. Ahn, M. et al. Analysis of the Native Structure, Stability and Aggregation of Biotinylated Human Lysozyme. *PLoS ONE*. **7**, (2012).
111. Guo, X. *et al.* Multi-Functionalized Chitosan Nanoparticles for Enhanced Chemotherapy in Lung Cancer. *Carbohydr. Polym.* **195**, 311–320 (2018).
112. Cahyana, A. H., Pratiwi, D. & Ardiansah, B. Citrate-Capped Superparamagnetic Iron Oxide (Fe3O4-CA) Nanocatalyst for Synthesis of Pyrimidine Derivative Compound as Antioxidative Agent. *IOP Conf. Ser.: Mater. Sci. Eng.* **188**, 012008 (2017).
113. Nigam, S., Barick, K. C. & Bahadur, D. Development of Citrate-Stabilized Fe3O4 Nanoparticles: Conjugation and Release of Doxorubicin for Therapeutic Applications. *J. Magn. Magn. Mater.* **323**, 237–243 (2011).
114. Ranoszek-Soliwoda, K. et al. The Role of Tannic Acid and Sodium Citrate in the Synthesis of Silver Nanoparticles. *J. Nanopart. Res*. **19**, (2017).
115. Bloemen, M. et al. Improved Functionalization of Oleic Acid-Coated Iron Oxide Nanoparticles for Biomedical Applications. *J. Nanopart. Res*. **14**, (2012).
116. Jadhav, N. V. et al. Synthesis of Oleic Acid Functionalized Fe3O4 Magnetic Nanoparticles and Studying their Interaction with Tumor Cells for Potential Hyperthermia Applications. *Coll. Surf. B*. **108**, 158–168 (2013).
117. Chen, H. et al. Development of Oleic Acid-Functionalized Magnetite Nanoparticles as Hydrophobic Probes for Concentrating Peptides with MALDI-TOF-MS Analysis. *Proteomics*. **11**, 890–897 (2011).
118. Wei, H. et al. Compact Zwitterion-Coated Iron Oxide Nanoparticles for Biological Applications. *Nano Lett.* **12**, 22–25 (2012).

119. Borlido, L., Azevedo, A. M., Roque, A. C. A. & Aires-Barros, M. R. Potential of Boronic Acid Functionalized Magnetic Particles in the Adsorption of Human Antibodies Under Mammalian Cell Culture Conditions. J*. Chromatogr. A*. **1218**, 7821–7827 (2011).
120. He, X., Yu, Y. & Li, Y. Facile Synthesis of Boronic Acid-Functionalized Magnetic Metal–Organic Frameworks for Selective Extraction and Quantification of Catecholamines in Rat Plasma. *RSC Adv*. **8**, 41976–41985 (2018).
121. Elsherif, M., Hassan, M. U., Yetisen, A. K. & Butt, H. Glucose Sensing with Phenylboronic Acid Functionalized Hydrogel-Based Optical Diffusers. *ACS Nano.* **12**, 2283–2291 (2018).
122. Bruen, D. et al. Boronic Acid Homopolymers as Effective Polycations for Sugar-Responsive Layer-by-Layer Assemblies. *ACS Appl. Polym. Mater*. **1**, 990–996 (2019).
123. Bruen, D., Delaney, C., Florea, L. & Diamond, D. Glucose Sensing for Diabetes Monitoring: Recent Developments. *Sensors.* **17**, (2017).
124. Alnaimat, F., Dagher, S., Mathew, B., Hilal-Alnqbi, A. & Khashan, S. Microfluidics Based Magnetophoresis: A Review. *The Chemical Record*. **18**, 1596–1612 (2018).
125. Dill, K. A. & Bromberg, S. Molecular Driving Forces: Statistical Thermodynamics in Chemistry and Biology. 2nd Ed. New York: Garland Science (2003).
126. SenGupta, A. K. Environmental Separation of Heavy Metals: Engineering Processes. 1st Ed. Boca Raton: CRC Press (2001).
127. Kulkarni, S. et al. Quantifying the Motion of Magnetic Particles in Excised Tissued: Effect of Particle Properties and Applied Magnetic Field. *J. Magn. Magn. Mater.* **393**, 243–252 (2015).
128. Pankhurst, Q. A., Thanh, N. T. K., Jones, S. K. & Dobson, J. Progress in applications of magnetic nanoparticles in biomedicine. *J. Phys. D: Appl. Phys.* **42**, 224001 (2009).
129. Roohi, R., Emdad, H. & Jafarpur, K. A Comprehensive Study and Optimization of Magnetic Nanoparticle Drug Delivery to Cancerous Tissues via External Magnetic Field. *JTE*. **47**, 681–703 (2019).
130. Kalambur, V. S., Han, B., Hammer, B. E., Shield, T. W. & Bischof, J. C. In Vitro Characterization of Movement, Heating and Visualization of Magnetic Nanoparticles for Biomedical Applications. *Nanotechnology.* **16,** 1221 (2005).
131. Lai, S. K. et al. Rapid Transport of Large Polymeric Nanoparticles in Fresh Undiluted Human Mucus. *PNAS*. **104**, 1482–1487 (2007).
132. Domínguez-García, P., Melle, S., Pastor, J. M. & Rubio, M. A. Scaling in the Aggregation Dynamics of a Magnetorheological Fluid. *Phys. Rev. E.* **76**, 051403 (2007).
133. Lim, J., Tan, D. X., Lanni, F., Tilton, R. D. & Majetich, S. A. Optical Imaging and Magnetophoresis of Nanorods. J*. Magn. Magn. Mater*. **321**, 1557–1562 (2009).
134. Sun, J., Shi, Z., Chen, S. & Jia, S. Experimental and Numerical Analysis of the Magnetophoresis of Magnetic Nanoparticles Under the Influence of Cylindrical Permanent Magnet. *J. Magn. Magn. Mater.* **475**, 703–714 (2019).
135. Garraud, A. *et al.* Investigation of the Capture of Magnetic Particles from High-Viscosity Fluids using Permanent Magnets. *IEEE Trans. Biomed. Eng.* **63**, 372–378 (2016).

136. Liu, J. F. *et al.* Use of Oppositely Polarized External Magnets To Improve the Accumulation and Penetration of Magnetic Nanocarriers into Solid Tumors. *ACS Nano* **14**, 142–152 (2020).
137. Jafari, S. *et al.* Magnetically targeted delivery through cartilage. *AIP Adv.* **8**, 056717 (2018).
138. Rao, Y. *et al.* Epirubicin-Loaded Superparamagnetic Iron-Oxide Nanoparticles for Transdermal Delivery: Cancer Therapy by Circumventing the Skin Barrier. *Small* **11**, 239–247 (2015)

Chapter 2

Magnetophoretic Transport of Functionalised Iron Oxide Nanoparticles Through Hydrated Polymer Networks

2.1 Introduction

The ability to guide and manipulate NPs from a distance is required for several biomedical applications[1]. Magnetophoresis offers several advantages over other active methods for particle manipulation such as electrophoresis, thermophoresis, dielectrophoresis and acoustophoresis[2]. In many of these cases, the medium can be damaged, for example, the heat generated in electrophoresis or thermophoresis can be a significant issue for biological applications[3]. Particle manipulation via magnetophoresis has the distinct advantage that it should not alter the properties of the medium. For example, magnetophoresis is used to enhance drug permeation across physical biological barriers in drug delivery applications[4]. The magnetic permeability, magnetic flux density and the susceptibility are key parameters for the design and optimisation of magnetophoretic applications[5].

Most magnetophoretic studies use the concept of high gradient magnetic separation (HGMS) to influence MNP motion[6]. This concept is based on magnetophoretic velocities being proportional to the magnetic field gradient. Since magnetophoretic velocities tend to be very low, very high field gradients are needed to induce motion. These high gradients can make is possible to separate MNPs with different susceptibilities. Higher gradients also make it possible to guide MNPs from a greater distance. Magnetic guidance is among the most intensively explored targeting approaches for biomedical applications because of its potential to reduce systemic drug exposure and make a local therapeutic effect achievable at significantly lower drug doses[7].

Magnetophoresis has been implemented in microfluidic devices for biomedical applications[8]. For example, magnetic channel walls have been used to capture magnetic beads in flow, by becoming immobilised and granting a functionalisation to the channel wall[9]. Another microfluidic study analysed particle transport in a magnetophoretic system[10]. This study consisted of an array of soft magnets embedded directly below a microfluidic channel. The magnetic field that was generated (0.25 T) was homogenous throughout the microfluidic channel, in which magnetic particles moved through. Bare iron oxide particles (d_{hyd} 250 nm) were pumped through the channel. This study discusses in detail the multitude of forces that influence magnetophoresis. Particle transport in a magnetophoretic system is governed by various forces including: the magnetic force due to all field sources, viscous drag, inertia, gravity, buoyancy, thermal kinetics, particle/fluid interaction perturbations to the flow field, and inter-particle effects (including magnetic-dipole, electrostatic, and van der Waals interactions). It was found that it was possible for the magnets in the microsystem to capture (immobilise magnetic particle on channel wall) 65 % of total particle population. This study highlights the value of applying a magnetic field and specific strengths for selective magnetophoresis.

When investigating magnetophoresis in biological studies, initial experiments require mimics for biological matrices such as tissue. Hydrogel polymers are often used as a mimic and are crosslinked polymer networks which can absorb large amounts of water-based-fluids[11]. Hydrogels are used to mimic the native hydrated micro-environments of human tissue whose scaffold structure comprises polymers based on structural proteins[12,13]. Hydrated polymer networks based on sodium alginate, agarose, chitosan, hyaluronic acid or collagen are regularly reported in the literature as tissue mimics[13–15].

One study by Salloum et al.[16], studied the magnetophoretic motion of MNPs in agarose gels (0.2-4 %w/v) as a mimic for human tissue. MNPs (d_{hyd} 10 nm), were injected into agarose gels with different flow rates. An electromagnetic field was applied to the gels (0.3 T) and their distribution profiles over time were digitally imaged. It was found that the distribution profiles were inconsistent in gels with higher agarose concentrations. In the lower agarose concentrations, the larger mesh sizes make it easier for the NPs to migrate in an isotropic manner to form spherical distribution. With smaller mesh sizes in higher agarose concentrations, NPs deposit on the solid structure rendering some pores along the flow path inaccessible to the NPs. This study demonstrates that the mesh size of a polymer network is critical for magnetophoretic transport. Understanding NP interactions with complex biological systems is important for optimising magnetophoretic transport through tissues[17]. Magnetophoretic studies in hydrogels allow for quick reaction times[18], real time analysis and tracking of magnetophoretic motion.

In this chapter, MNPs were synthesised by different protocols of the Pinna[19] method to obtain monodisperse, responsive superparamagnetic iron oxide NPs. Three different protocols (Reflux, acid-bomb and digestion microwave) were tested using benzyl alcohol and iron acetylacetonate. The synthesised MNPs were characterised by transmission electron microscopy (TEM), magnetometry and dynamic light scattering (DLS). MNPs were functionalised with a variety of surface chemistries to obtain a range of d_{hyd} and surface charges. A method was developed to optically track magnetophoretic transport of these functionalised MNPs in an agarose-based tissue mimic where H_2O was employed as the aqueous phase (agarose-H_2O). The agarose medium was optimised for magnetophoretic transport (gel depth, gel viscosity, MNP concentration, etc.). Given the linear transport behaviour over time of functionalised MNPs, experimental velocity (v_{exp}) values were calculated and shown to differ for the different MNP functionalisation's used. The ability to synthesise monodisperse superparamagnetic MNPs and track their motion and observe velocity dependency on surface chemistry is of great interest for future in-vivo applications such as drug delivery and targeted biomarker capture[20].

2.2 Materials & methods

2.2.1 Materials

Steel autoclave with Teflon inner tube (25 mL), G30 glass test tube, reagent glass bottle (50 mL), Liebig condenser, glass vials (7 mL), zeta capillary folded cuvettes (Malvern), plastic cuvettes. A 50 x 50 x 25 mm grade N52 neodymium magnet (F335-N52) was used for all magnetophoretic studies in this chapter (www.first4magnets.com). Iron acetylacetonate (14024-18-1), benzyl alcohol (100-51-6), tetrahydrofuran (THF) (109-99-9), (3-glycidyloxypropyl)trimethoxysilane (GLYMO) (2530-83-8), acetone (67-64-1), sodium citrate tribasic (III) (6132-04-3), chloroform (67-66-3), potassium hydroxide (KOH) (1310-58-3), arginine (74-79-3), 3-aminophenylboronic acid (206658-89-1), ethanol (64-17-5), dopamine hydrochloride (62-31-7), propanesultone (1120-71-4), ammonia (7664-41-7), dimethylformamide (DMF) (68-12-2), sodium carbonate (6106-20-3), iodomethane (74-88-4), ethyl acetate (141-78-6), 2-[2-(2-methoxyethoxy)ethoxy]acetic acid (MEEA) (16024-58-1), agarose (9012-36-6) (low electroendosmosis (EEO)) (0.09-0.13), and phosphate buffered saline (PBS) tablets (78392) were all purchased from Sigma-Aldrich. Jeffamine M1000 and M2070 were obtained from Huntsman Corporation.

2.2.2 Instrumentation

For the synthesis of MNPs, three different protocols were used. The reflux protocol used an Electromantle obtained from Electrothermal in the UK. The acid bomb protocol used a Memmert oven obtained from Lennox Laboratories in Ireland. The microwave digestion protocol used an Anton Paar Monowave 300 from Anton Paar available in DCU. To characterise the d_{hyd} and the surface charge of the functionalised MNPs, a Malvern Zetasizer Nano ZS was used for both. This was available in DCU. During the functionalisation process of the MNP cores, it was necessary to agitate the MNPs using a PMR-30 2D fixed tilt rocker obtained from Grant Instruments in the UK. The agarose gels were prepared using a heat-stir CB142 hot plate obtained from Stuart Equipment in the UK. In order to measure the viscosity of the agarose gels, a Kinexus Pro+ Rheometer was used. This was available in DCU. To track the movement of MNPs through hydrated gel networks, a Nikon 3300 digital camera was purchased from Birmingham Cameras in Ireland.

2.2.3 Iron oxide nanoparticle synthesis

2.2.3.1 Reflux protocol

Iron acetylacetonate (2 g) was added to benzyl alcohol (40 mL) in a 50 mL round bottom flask. This mixture was bubbled with N_2 for 15 min. A standard reflux was set up with the Liebig condenser attached to the round bottom flask. The flask, containing the mixture was placed into an electromantle at 200 °C. The reaction was supervised for 7 h until the mixture turned from a brick-red to a blue-black colour. The mixture was then transferred to a 50 mL reagent glass bottle and bubbled through with N_2 for 5 min and sealed.

2.2.3.2 Acid bomb protocol

Iron acetylacetonate (1 g) was added to benzyl alcohol (20 mL) in a glass beaker. This mixture was bubbled with N_2 for 15 min. The mixture was then transferred to a steel-autoclave with an inner Teflon tube and autoclaved at 200°C for 48 h. The mixture was then transferred to a 50 mL reagent glass bottle and bubbled through with N_2 for 5 min and sealed.

2.2.3.3 Microwave digestion protocol

Iron acetylacetonate (1 g) was added to benzyl alcohol (20 mL) in a glass beaker. This mixture was bubbled with N_2 for 15 min. The mixture was then transferred to a glass G30 test tube with Teflon cap and microwave digested. The initial temperature was set at 55 °C while the pressure built up to 30 psi. The temperature was ramped to 200 °C over 10 min and held at 200 °C for 3 h before venting to cool to 55 °C. The test tube was then removed and the mixture was transferred to a 50 mL reagent glass bottle, bubbled through with N_2 for 5 min and sealed.

2.2.4 MNP functionalisation

2.2.4.1 PEG1000 functionalisation

To functionalise the MNP surface with PEG, iron oxide NPs (2 mL, 1 mg/mL) in benzyl alcohol were added to a vial with acetone (4 mL). This caused the MNPs to precipitate out of the benzyl alcohol. The glass vial was then placed on a magnet to retain the MNPs while the benzyl alcohol/acetone mixture was removed. This step was repeated 3 times to ensure all benzyl alcohol was removed. GLYMO (50 µL) was dissolved in chloroform (2 mL), and added to the MNP material. This mixture was then placed on a plate shaker at 400 rpm for 24 h. THF (2 mL) was used to remove excess GLYMO by magnetic separation after agitation. GLYMO was used to modify the surface of the MNPs through covalent attachment of functional alkoxysilanes, simultaneously providing surface epoxide groups ready for further conjugation chemistry

PEG (7.0 µL) was dissolved in THF (2 mL) and added to the GLYMO-MNP material. This was placed on a plate shaker at 400 rpm for approx. 5 h. KOH (50 µL, 1.0 M) was then added to precipitate the MNPs. The resulting PEG1000-MNPs were made up with DI H_2O to desired concentration (Figure 2.1).

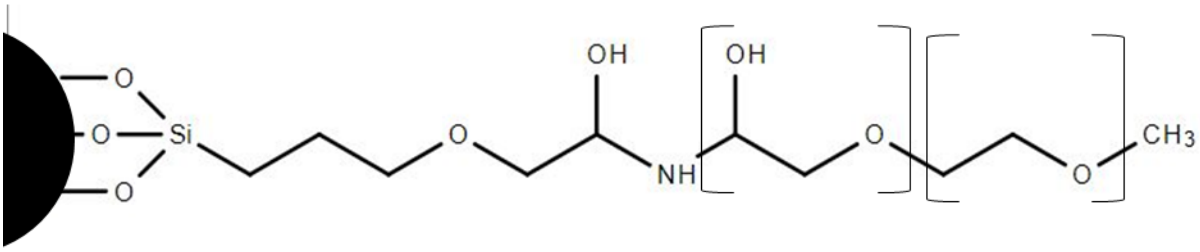

Figure 2.1 Surface chemistry for PEG1000-MNPs.

2.2.4.2 Citrate functionalisation

Citrate-MNPs were synthesised using the same method as described in Section 2.2.4.1, except in place of the GLYMO/chloroform solution, sodium citrate (4 mL, 0.6 g/L) in DI H_2O was added to the MNP material. The mixture was then placed on a plate shaker at 400 rpm for approx. 4 h. The functionalisation was deemed complete when the dispersion turned from blue-black to a dark brown colour. The carboxylate groups of the citrate strongly coordinate to the surface iron cations on the MNP to form a strong bond. The uncoordinated carboxylate groups extend into the aqueous medium, conferring a high degree of water stability[22] (Figure 2.2).

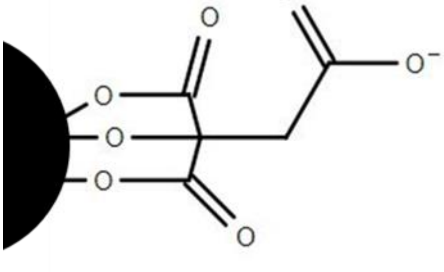

Figure 2.2 Surface chemistry for citrate-MNPs.

2.2.4.3 Arginine functionalisation

Arginine-MNPs were synthesised using the method as described in Section 2.2.4.1 previously up to the point where the GLYMO-MNPs are prepared. Arginine (0.005 g) dissolved in 2 mL DI H_2O was added in place of the PEG/THF solution to the GLYMO-MNPs. This was placed on a plate shaker at 400 rpm for approx. 5 h. The functionalisation was deemed complete when the dispersion turned from blue-black to a dark brown colour (Figure 2.3).

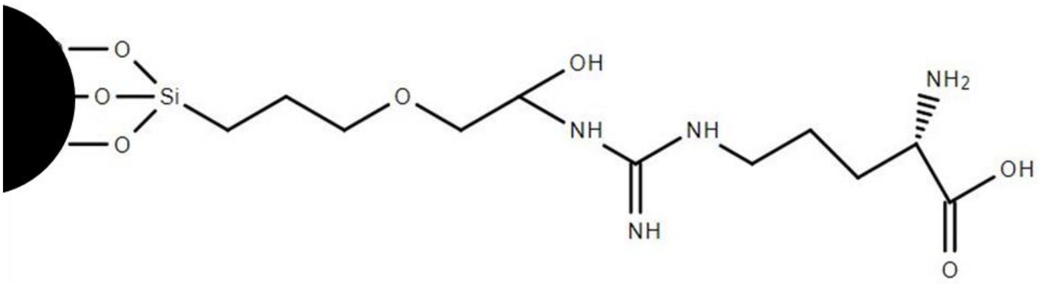

Figure 2.3 Surface chemistry for arginine-MNPs.

2.2.4.4 Boronic acid functionalisation

Boronic acid-MNPs (BA-MNPs) were synthesised using the method as described in Section 2.2.4.1 up to the point where the GLYMO-MNPs were prepared. 3-aminophenylboronic acid (2 mL, 2.5 mg/L) was then added to GLYMO-MNPs and placed on a plate shaker at 400 rpm for 5 h. KOH (50µL, 1.0 M) was added to precipitate out the BA-MNPs. Finally, BA-MNPs were made up with DI H_2O to desired concentration (Figure 2.4).

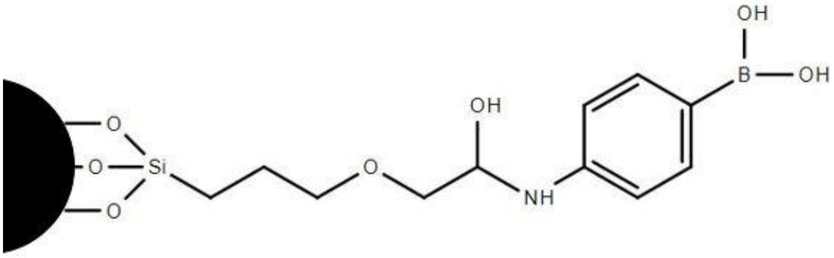

Figure 2.4 Surface functionalisation for BA-MNPs.

2.2.4.5 Dopamine sulphonate functionalisation

This method was adapted from a publication by H. Wei[23] and is divided into three steps.

Step 1 Synthesis of DS: To prepare DS, ethanol (50 mL) was deoxygenated by bubbling N_2 through it for 1 h in a 150 mL round bottom flask. Dopamine hydrochloride

(1.14 g) was dissolved in the ethanol. Propanesultone (0.8 g) and ammonia (416 µl) were added to the solution. This was then heated to 50 ºC in a water bath and stirred for 72 h. The round bottom flask was capped to ensure a nitrogenated environment. The mixture was then placed in a glass dish and heated overnight at 60 ºC to remove excess solvent. The resulting waxy mixture was washed with ethanol to dissolve any remaining propanesultone. The DS was dried under reduced pressure.

Step 2 Synthesis of zwitterionic DS: DS (0.33 g) was dissolved in DMF (50 mL) in the presence of sodium carbonate (0.254 g). Iodomethane (2.2 mL) was added to the mixture and stirred for 12 h. The solvent was removed under reduced pressure via rotary evaporation. DMF (5 mL) and ethyl acetate (45 mL) were added to the remaining precipitate. This was centrifuged, and the solid product was collected. DMF (5 mL) and acetone (45 mL) were added to the solid. This was refluxed at 55 ºC for 2 h. The resulting mixture was centrifuged and solid was collected. The reflux and filtration steps were repeated 2 more times. A white solid was obtained after drying under reduced pressure.

Step 3 DS functionalised MNPs: To functionalise the MNPs with DS, MNPs (17 mg) were added to MEEA (327 µL) in methanol (7.5 mL) and stirred for 5 h at 70 ºC in order increase the overall solubility of the MNPs for the next step. The precipitate was washed with acetone followed by hexane. DS (250 mg) was added in DMF/DI H_2O (7:1) to the MNPs. A second ligand exchange takes place where the zwitterionic DS exchanged with the MEEA. This solution was stirred at 70 ºC for 12 h. The MNPs was washed with acetone to remove excess solvent and re-dispersed in DI H_2O (Figure 2.5).

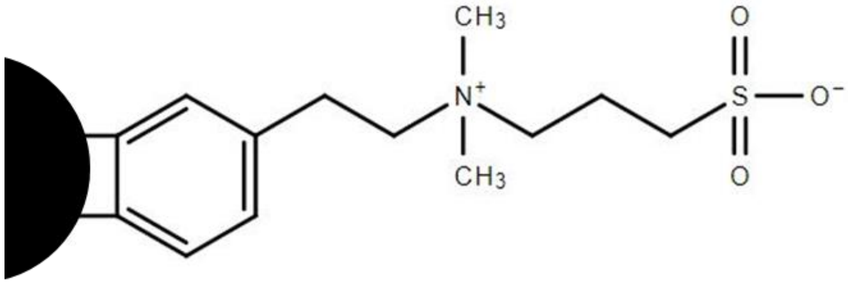

Figure 2.5 Surface functionalisation of DS-MNPs.

2.2.4.6 Magnetic nanoparticle characterisation

All MNP suspensions were characterised using DLS on the Malvern Zetasizer Nano ZS. DLS was used to determine the size distribution profile within a MNP suspension. Light is passed through the sample and the light scatters in multiple directions, known as Raleigh scattering. The fluctuations at which light is scattered are dependent on the size of the particle. Once the particles have been measured, a polydispersity index is also obtained from a fit of the auto-correlation function of the recorded intensity profile. This is a measure of the heterogeneity of the sample based on sizes. A PDI value below 0.2 is indicative of narrow particle size population. Experiments were performed at 25^{o}C and the Z-average d_{hyd} and PDI values from 2nd cumulants analysis are reported. The MNP sample was diluted until it turned from a black opaque dispersion to a transparent brown dispersion (Dilution factor of ~20). 1 mL of this dispersion was then placed into a cuvette, until it filled a minimum of 15 mm of the plastic cuvette. This was then placed into the Zetasizer and the lid was closed to prevent interference from outside light.

ζ_p measurements were performed at 25 °C on the Zetasizer Nano ZS. The MNP sample was diluted until it turned from a black opaque dispersion to a transparent brown dispersion (Dilution factor of ~20). 1 mL of the MNP solution was injected into a folded capillary cell slowly to avoid air bubbles. The caps were then placed at each opening of the capillary cell. The capillary cell was then placed firmly into the Zetasizer until it clicked into place. The lid was closed and the ζ_p was measured. The ζ_p is a measure of the magnitude of the charge repulsion/attraction between particles. A particle with a surface charge of >±30 mV is deemed stable enough to repel another particle of similar charge.

2.2.5 Agarose gel preparation

To prepare agarose gel (0.3% w/v unless otherwise specified), 0.06 g agarose (low EEO content) was added to DI H_2O or PBS solute as specified. This mixture was heated and stirred until the agarose had fully dissolved. Once the agarose solution was transparent, glass vials (53 × 15 × 15 mm) were filled with agarose to a depth of 6 mm (700 µL) and left to cool at room temperature for 1 h. The vials were then capped and left to solidify overnight at 4°C. Prior to use, agarose gels were removed from the fridge and allowed to reach room temperature.

The temperature was not strictly controlled for these experiments; it was assumed that room temperature was reached after 1 h of exposure prior to the magnetophoretic transport experiment. For bulk viscosity measurements, agarose was prepared in a plastic petri dish. The agarose was carefully removed from the petri dish after 1 h to reach room temperature and then placed on the stage of the Kinexus rotational rheometer. The agarose viscosity was measured over a shear ramp from 10^{-4} to 10^{-1} Hz (n = 3).

2.2.6 Imaging of agarose gels during magnetophoresis

PEG1000-MNPs at a concentration of ~1.0 mg/mL were prepared. Agarose-H_2O gels (6 mm depth unless otherwise specified) were prepared in glass vials and placed onto a corner of the cube N52 neodymium magnet, where it would be expected that the magnetic force would be strongest. MNPs (100 µL) were pipetted onto the top surface of the agarose gel to form an even layer of ~1 mm thickness covering the entire upper gel surface (176.6 mm^2), and the vial was capped. The MNPs migration through the gel towards the base of the vial under the influence of the magnetic field over time was monitored (Figure 2.6). Vials were imaged every 30 min using a standard digital camera. ImageJ software was used to process the images to measure the position of the MNP front over time in order to calculate MNP experimental terminal velocity (v_{exp}).

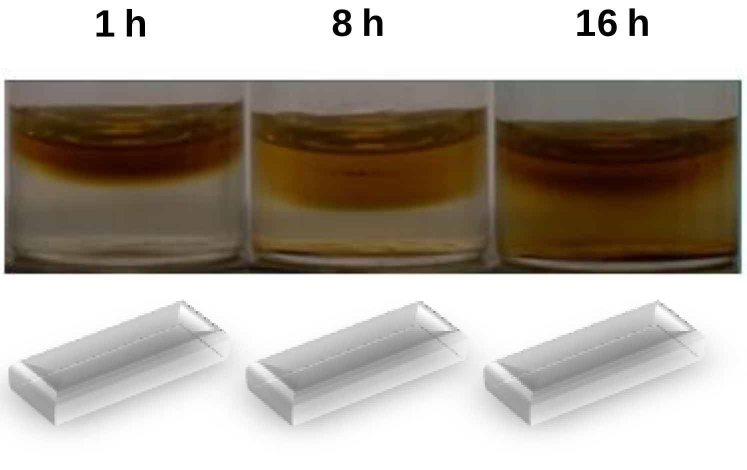

Figure 2.6 Images showing ~1 mg/ml PEG1000-MNPs (d_{hyd} 24.0 nm, (0.16)) moving through agarose-H_2O (0.3% w/v) towards an external magnet over time. Images were taken at 1, 8 and 16 h.

The images were cropped and loaded into ImageJ software to determine the distance travelled by the MNPs into the agarose at each image. A scale bar was generated in ImageJ, which was used to measure the total height of the gel (A) and the furthest point of the centre of the MNP front (B). Point A was converted to the total height of the gel (6 mm) and point B was converted as a percentage of A to measure distance travelled into the gel (x mm). This was done for each individual image and plotted as distance from magnet vs time to determine $v_{exp.}$

2.3 Results & Discussion

2.3.1 Synthesis of iron oxide nanoparticles

Synthetic protocols adapted from the Pinna method[19] were used to synthesise iron oxide NPs where the aim was to identify a synthesis protocol that yielded small, monodisperse MNPs. This chemical route of synthesis uses benzyl alcohol as a capping agent to control the rate of iron crystallisation into magnetite. The benefits of using a non-aqueous phase method are that the resulting MNPs are not covered in undesirable surfactants. Three different synthesis protocols were used according to the methods section – referred to as reflux, acid bomb and microwave digestion protocols. The resulting iron oxide cores were functionalised with a PEG1000 polymer and characterised by DLS to determine d_{hyd} and PDI values (Figure 2.7). This was done to determine if aggregates were present as the presence of aggregates would an indicate that iron was converted to magnetite and not crystallised further to hematite or maghemite.

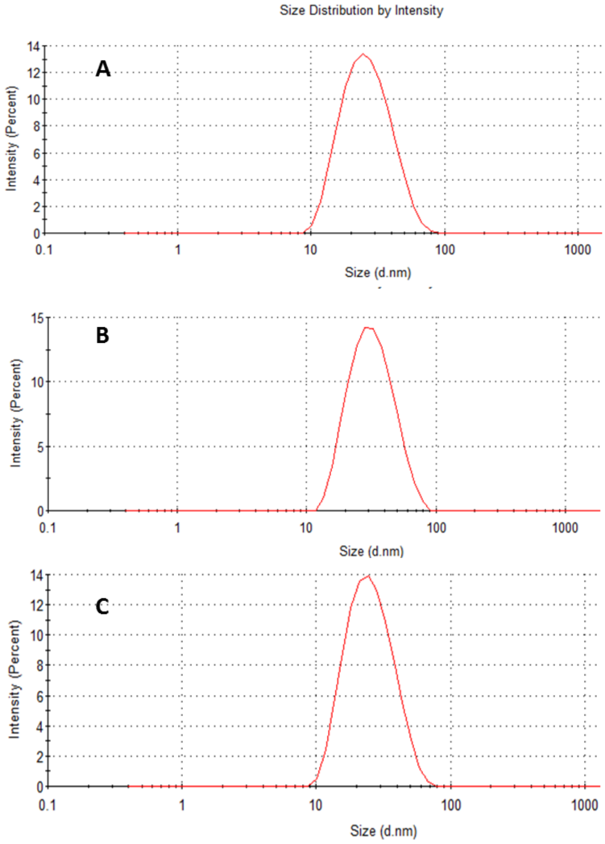

d_{hyd}:	23.7±1.2
PDI:	0.18±0.01

d_{hyd}:	24.1±0.3
PDI:	0.17±0.01

d_{hyd}:	24.1±0.5
PDI:	0.16±0.03

Figure 2.7 Size distribution profiles of PEG1000-MNPs synthesised by (A) reflux, (B) acid bomb and (C) microwave digestion protocols. The tables (right) show the measured d_{hyd} values and corresponding PDI values, n=3.

All protocols resulted in unimodal size distribution profiles with a PDI value of under 0.2. The reflux protocol is the most challenging synthesis, as a constant temperature is needed to ensure uniform crystallisation of the iron acetylacetonate. In the case of the reflux protocol, there may have been temperature fluctuations potentially leading to the formation of hematite which was observed in some earlier syntheses where red residue formed on the glassware. Hematite is antiferromagnetic, meaning its magnetisation can never be zero due to the odd number of electrons, meaning they will be attracted to magnetite or maghemite crystals. The major difference between these two protocols is the time required for synthesis, the acid bomb method takes 48 h, while microwave digestion takes 4 h. In the interest of time, the microwave digestion protocol was used to synthesise all MNPs in this work. The MNPs synthesised by microwave digestion were imaged by TEM to confirm core size (Figure 2.8). MNP samples were sent to UCD for TEM imaging. The core size was calculated as an average of 208 MNPs, chosen from several TEM images of the same MNP batch, and was found to be 8.9±0.8 nm.

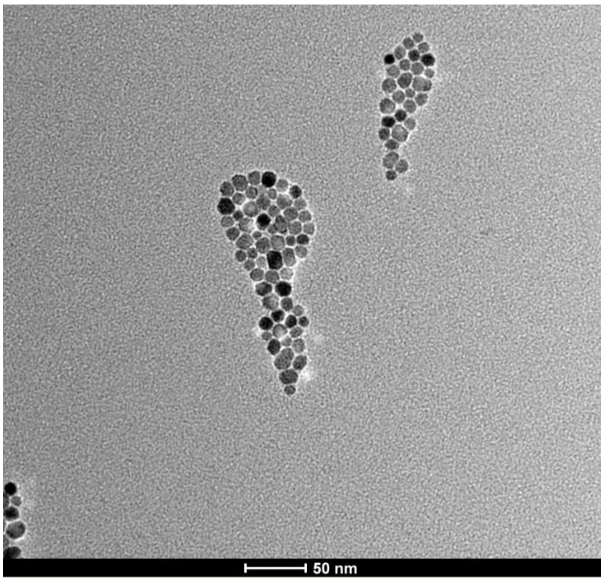

Figure 2.8 TEM image of synthesised MNPs (microwave digestion) at X150K magnification. TEM imaging was carried out by PhD student Eoin McKiernan in University College Dublin (11/10/2019).

To characterise the magnetisation behaviour of the synthesised MNPs, magnetometry was performed. The magnetometry data passes through zero, showing that in the absence of an external magnetic field the MNPs are not magnetic, showing that they are superparamagnetic. The saturation magnetisation was found to be 63.34 emu/g (3.2×10^5 A·m^{-1}, assuming a mass density of 5000 kg·m^3 for iron oxide) indicating strong magnetic responsiveness (Figure 2.9).

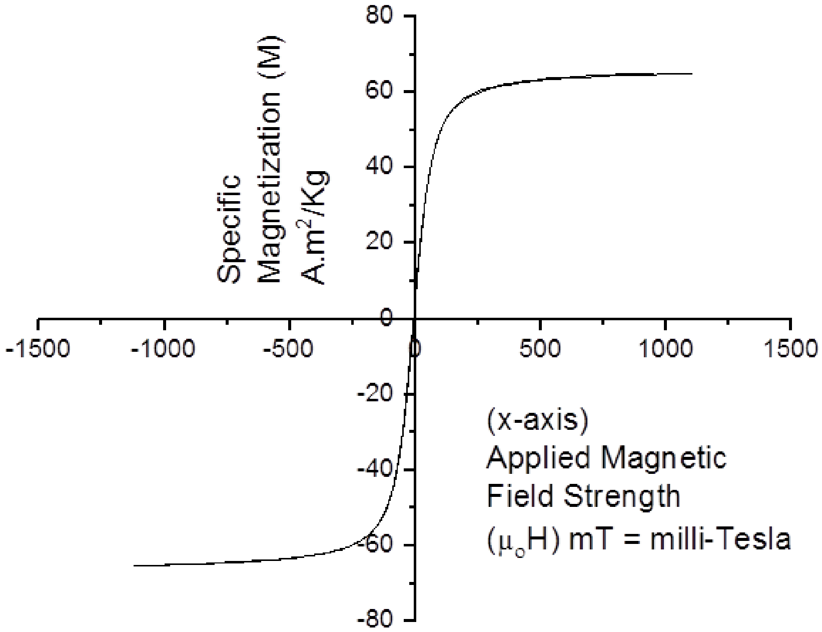

Figure 2.9 Magnetometry data for synthesised MNPs from -1500 mT to 1500 mT. Magnetometry was performed by Prof. Gun'Ko (Trinity College Dublin).

2.3.2 Characterisation of PEG1000- and citrate-MNPs

MNPs were functionalised with PEG1000 and citrate chemistries according to Sections 2.2.4.1 & 2.2.4.2, respectively. Both surface chemistries are linked to the surface of the magnetite core through covalent bonds. PEG is a biocompatible polymer, which possesses a near neutral surface charge and is stabilised as a MNP functionalisation via steric hindrance[24]. Citrate is also biocompatible, has a smaller chemical footprint and exhibits a strong negative surface charge[25]. DLS data for the functionalised MNPs is given in Table 2.1; core size was determined by TEM to be 8.9 nm.

Table 2.1 Tabulated DLS data for PEG1000- and citrate-MNPs.

Surface chemistry	TEM Core (nm)	d_{hyd} (nm)	PDI	ζ_p (-mV)
PEG1000	8.9	24.1	0.16	-9.5
Citrate	8.9	12.1	0.18	-27.3

The d_{hyd} for PEG1000-MNPs was reported to be 24.1 nm, 15.4 nm greater than the iron oxide core d_{hyd}. The PDI was 0.16 which was the same as that of the core. This was expected as PEG is known for its stability. A ζ_p of -9.5 mV was measured for the PEG1000-MNPs, showing it to be weakly negative. (A value of approx. ±5 mV indicates stability whereas a value of ±15 mV indicates a strong negative or positive charge). The weak negative charge observed in this case may be possibly due to the hydroxyl groups generated during the epoxide ring opening reaction[21]. Citrate-MNPs had a significantly lower d_{hyd} (12.1 nm), as would be expected. The PDI increased slightly after citrate functionalisation indicating a slight decrease the overall colloidal stability of the MNPs. The citrate-MNPs exhibited a strong negative charge (-27.3 mV) attributed to the negatively charged citrate ions.

To further verify functionalisation had occurred, Fourier transfer infrared spectroscopy (FTIR) was performed (Figure 2.10). FTIR confirmed that GLYMO had bound to the MNP surface forming stable GLYMO-MNPs as a pre-cursor for the PEG1000-MNPs. The GLYMO-MNPs exhibit Si–O, Si–O–R stretching modes at 1107 and 1052 cm^{-1}, respectively, in addition to the C-H asymmetric stretching modes at 2861 cm^{-1}. The most notable features of the GLYMO-MNPs are the epoxide ring stretching modes at 864, 916 and 1295 cm^{-1}, which were not observed after the coupling reactions.

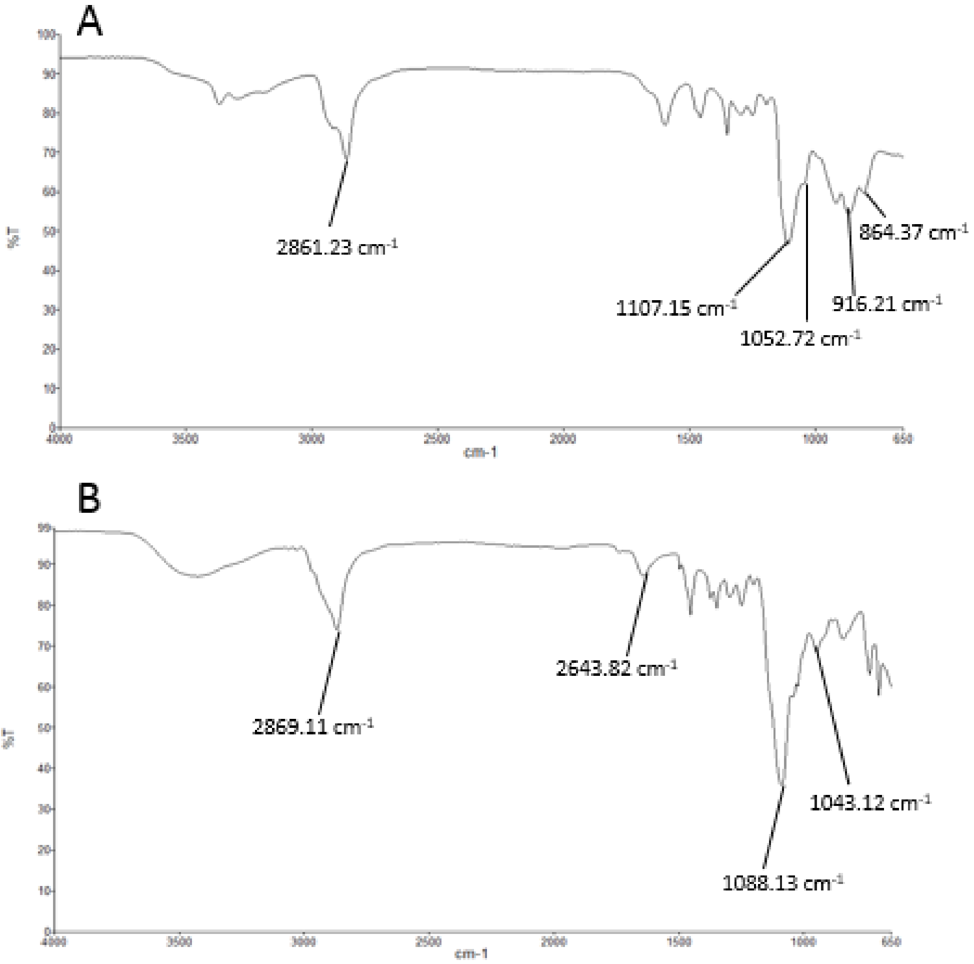

Figure 2.10 A) FTIR of GLYMO-MNPs and B) FTIR of PEG1000-MNPs.

A spectrum obtained for the PEG1000-MNPs confirmed that the epoxide ring from the GLYMO opened via amide linkage. The PEG-MNPs exhibit Si–O stretching modes at 1088 cm^{-1}, respectively, in addition to the C-H asymmetric stretching modes at 2869 cm^{-1}. After the epoxide ring was broken, the associated C-N stretching and N-H bending modes were observed in the region of 1643 cm^{-1}. C–O–C stretching vibrations were observed in region of 1043-1080 cm^{-1}. FTIR confirmed the PEG functionalisation process for the MNPs was successful.

Citrate functionalisation could not be confirmed by FTIR, as the two defining bonds are below the wavelength accessible by the FTIR used. In order to confirm functionalisation of citrate-MNPs, thermogravimetric analysis (TGA) was used. MNP samples were sent to CREST in the Focas Institute in Dublin. 100 mg of each MNP sample was dried in the oven at 110 °C to evaporate off any water in the sample. TGA analysis was performed on citrate- and PEG1000-MNPs. For the citrate-MNPs, there was a two-step degradation observed (Figure 2.11 A). In the first step, the water molecules are coordinated to the MNP surface, leading to a higher boiling point. The weight change between 120 and 170 °C was evidence of the loss of coordinated water, which was only present in a coordination bond between the citrate and the iron oxide core surface. The second step observed the citrate molecules decomposing as expected from 300 °C. This step accounted for a weight loss of 30 %. The weight loss stabilised completely at approx. 400 °C, indicating all organic matter had combusted. In order to calculate the estimated number of functional groups on a MNP, the core surface area and grafting density were required. The surface area for an 8.9 nm sphere is 248.85 nm^2. The grafting density was calculated to be 1.78 nm^{-2}. Therefore, the estimated number of functional groups was calculated per MNP was 443.

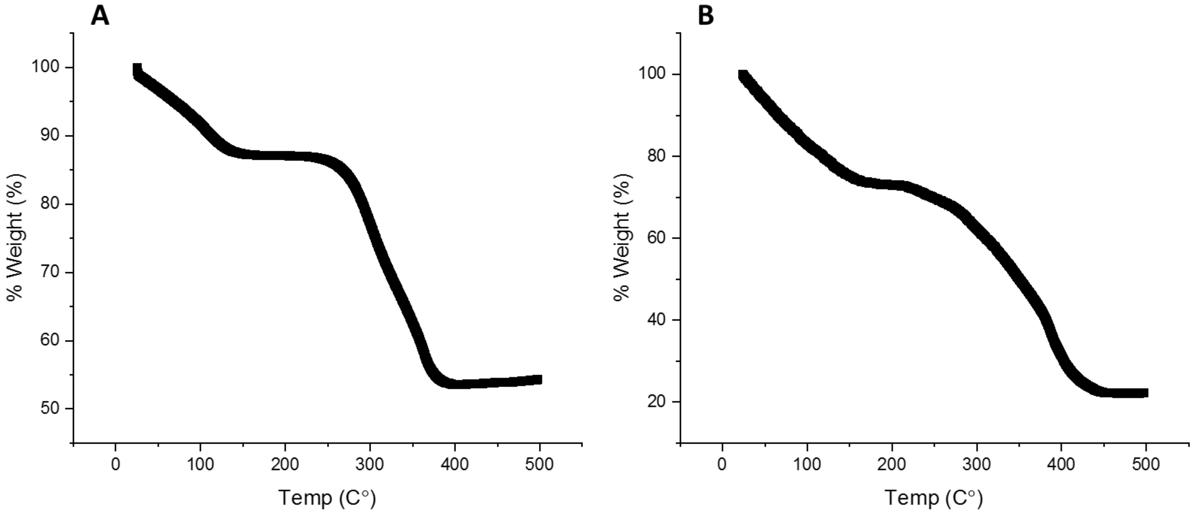

Figure 2.11 TGA analysis of A) citrate-MNPs and B) PEG1000-MNPs ramped to 500 °C. TGA analysis was carried out externally at the Focas Research Institute by Drs Power and Duffy.

For PEG1000-MNPs, TGA analysis was carried out to further characterise the material (Figure 2.11 B). An initial weight loss was seen up to 120 °C, as water evaporated. A significant weight loss of 29.5 wt% occurred between 280 and 378 °C, corresponding to the decomposition of the GLYMO and PEG groups. The GLYMO and PEG groups have a boiling point of 299 and 290 °C respectively and so the decrease in weight over this range was representative of these groups decomposing. Weight loss began to stabilise at 380 °C. In order to calculate the estimated number of functional groups for a PEG-MNP, the core surface area and grafting density were required. The surface area for an 8.9 nm sphere is 248.85 nm^2. The grafting density was calculated to be 1.99 nm^{-2}. Therefore, the estimated number of functional groups was calculated per MNP was 495.

The effect of the ionic strength (IS) of the MNPs environment on population stability was also studied. PEG- and citrate-MNPs were dispersed in PBS of varying IS and DLS measurements after 30 min were taken (Table 2.2). It can be seen that d_{hyd} values for PEG1000-MNPs were not significantly affected by changes in IS. Indeed PEG1000-MNPs remained colloidal disperse in high IS environments for at least 21 days. This is explained by the fact that PEG1000-MNPs are stabilised by steric hinderance as opposed to stabilisation via electrostatics. On the other hand, the citrate-MNPs are electrostatically stabilised, so increases in IS would be expected to diminish the diffuse layer of a charged MNP. However, this was not what was observed for citrate-MNPs. This was most likely due to a weakening of the Stern layer, which lowers the ability of the particle to repel other like-charged particles. When there is not a sufficiently strong charge on a particle to repel another particle, this could lead to some minor aggregation. As well as this, in high IS, citrate MNPs lose responsiveness to a magnetic field and precipitate out of solution within minutes.

Table 2.2 Tabulated DLS data for ~1mg/mL PEG1000- & citrate-MNPs d_{hyd} in PBS with varying IS.

Surface Chemistry	**d_{hyd} (nm)**	**d_{hyd} (nm)**	**d_{hyd} (nm)**	**d_{hyd} (nm)**
	IS – 0	**IS – 0.007 M**	**IS – 0.014 M**	**IS – 0.140 M**
PEG1000	24.0	24.1	24.1	24.6
Citrate	12.0	12.2	12.7	19.3

2.3.3 Characterisation of agarose for magnetophoresis

Agarose gel is regularly used as mimic for soft tissue and other biological systems including the vitreous humour of the eye or brain ECM models[26–28]. Agarose is cost effective, safe to use and its physical properties such as bulk viscosity and pore diameter range can be easily tailored as required. In this research, it is being used as a mimic for the skin tissue-based ECM. Based on literature, concentration ranges of 0.3 – 0.6% agarose are typically used to mimic this enviroment[14,29,30]. The bulk viscosity of agarose is dictated by controlling the agarose concentration per weight volume. Agarose is a polymer; its hydrogel form is a biphasic medium comprising agarose fibres and an aqueous component. Together, these two components form the porous agarose gel. As with bulk viscosity, the mesh size is directly proportional to the concentration of agarose[31,32,33]. Agarose-H_2O gels with varying % w/v agarose were prepared and their viscosities were measured using a rheometer (Figure 2.12).

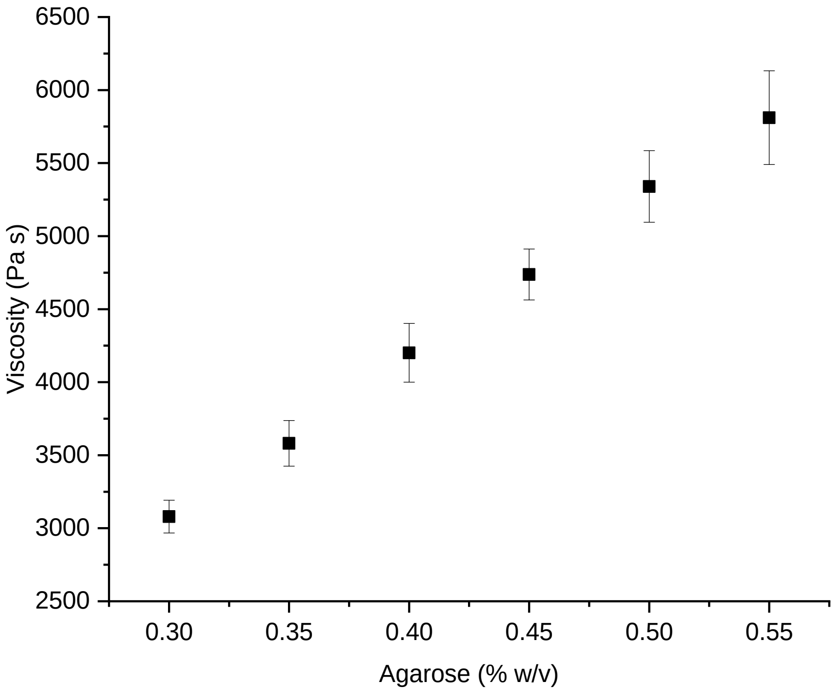

Figure 2.12 Measured bulk viscosity values for agarose-H_2O with varying % w/v agarose, n=3.

Agarose-H_2O gels prepared with a % w/v < 0.3% were found not to solidify fully and were thixotropic in nature. Above 0.6% w/v, the agarose appeared opaque most likely due to the agarose fibres clumping together and not fully dissolving. For these reasons, only the range from 0.3% to 0.55% w/v was investigated. Overall, a linear increase in bulk viscosity was observed as a function of increasing % w/v agarose.

2.3.4 Magnetophoretic transport of MNPs through agarose

To investigate the behaviour of MNPs in external inhomogeneous magnetic fields through hydrated gel networks magnetophoretic transport of PEG1000-MNPs through agarose-H_2O gels was investigated. To perform these studies, agarose-H_2O gels were prepared according to Section 2.2.5. Aliquots of MNP dispersions were dropped onto the top of the gels and a neodymium alloy magnet was then placed under the base of this glass vial to generate the field gradient. The movement of MNPs through the agarose-H_2O was tracked by digitally imaging the MNP front as it moved through the gel. The distance the front travelled was measured over time (Figure 2.13) whereby was possible to determine the front position to a precision of 0.001 mm. The initial data point (t=0) was omitted for all experiments here as turbulent behaviour was associated with the migration front settling and passing through the upper gel surface. Linear behaviour of the front position from 30 min was observed demonstrating a terminal velocity was reached quickly and maintained over the time course of the experiment. A value for the experimental velocity (v_{exp}) of the MNPs was obtained by calculating the slope of the linear regression line fitted to the data. A v_{exp} of 0.374 mm/h was achieved in the case of the PEG1000-MNPs. It can be concluded that the magnetic field gradient exerted is constant over the distance measured and the agarose medium is homogenous over the measurable length scale of the optical image.

It was important to investigate if in the absence of a magnetic field, whether the MNPs can migrate via diffusion through the agarose-H_2O and in what timescales. To investigate this, two experiments were carried out (Figure 2.13). In the first experiment (blue), the PEG-MNPs were placed on top of the agarose gels as before but in the absence of a magnetic field and it was observed that no movement of the particles through the gel occurred over the timescale investigated. In the second experiment, magnetophoresis of the PEG100—MNPs was carried out as before, but where the magnetic was removed after 4 h (red). In this case, it can be observed that the transport of the MNPs is arrested after removal of the magnet. These results show that the MNPs are only transported through agarose-H_2O in the presence of a magnetic field, as expected. The absence of an external magnetic field resulted in no significant transport of the PEG1000-MNPs beyond minor diffusive interactions with the gel surface over the 8 h period of the experiment.

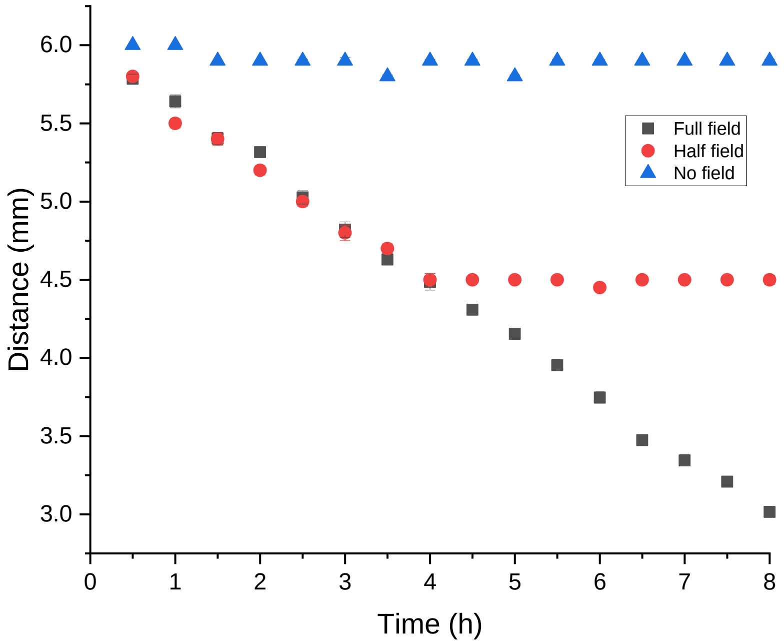

Figure 2.13 Magnetophoretic transport of ~1 mg/ml PEG1000-MNPs (d_{hyd} 24.1 nm (0.16)) through agarose-H_2O (0.3% w/v) under varying magnetic field conditions.

The geometry of a magnet will also impact the strength and direction of these field gradients. Therefore, it is important to examine the effect of positioning of the agarose gel vial on the magnet for magnetophoretic experiments. The outer corners of a square or rectangular magnet will have the strongest field gradient, due to the overlapping gradients projecting from the magnet's edges. In order to investigate this, v_{exp} values for PEG1000-MNPs were measured at six different positions (4 corners, centre and side mid-way points) on the magnet (Figure 2.14). There were no significant differences observed in v_{exp} at the four corners (1-4). There were noted decreases in v_{exp} values for positions 5 and 6 (centre and side mid-way points, respectively), on account of weaker magnetic field gradients. It is interesting to note, that MNP v_{exp} does not vary as its distance from the magnet changes which is consistent with what was observed already. Linear regression models applied to the data show that the regression lines for data generated at Positions 5 and 6 are offset from other data, which may be due to the initial penetration of the gel surface being dependent on magnetic field gradient. This data shows that the field strength and field gradient will have a direct effect on penetration time and v_{exp} as expected.

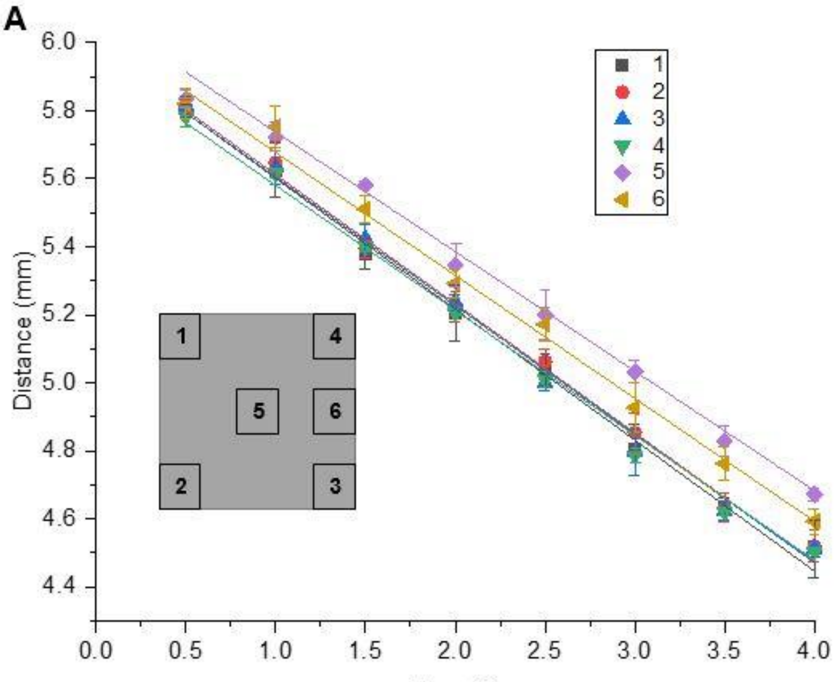

B

Position	v_{exp} (mm/h)	Std Dev
1	0.373	0.001
2	0.374	0.001
3	0.374	0.001
4	0.375	0.002
5	0.354	0.002
6	0.362	0.003

Figure 2.14 A) Magnetophoretic transport of ~2.0 mg/mL PEG1000-MNPs (d_{hyd} 24.1 nm (0.16)) in DI H_2O through agarose-H_2O (0.3% w/v) as a function of time (n=3) for 6 different vial positions on the magnet. Inset is schematic showing vial position. $R^2 > 0.994$ for all linear regression. B) Table showing measured v_{exp} values for PEG1000-MNPs in relation to magnet position with standard deviation, n=3.

2.3.5 Optimisation of agarose for magnetophoresis

The bulk viscosity of agarose was shown earlier to increase linearly with concentration in the range of 0.3% to 0.55% w/v. To investigate the effect of agarose viscosity on MNP velocity, the movement of the MNPs was tracked via imaging as they moved through the gels with varying agarose concentrations (w/v) in this range. Constant velocities were observed across all agarose concentrations (data not shown) and v_{exp}

was seen to decrease with increasing % agarose (Figure 2.15). This demonstrates that in the range of bulk viscosity studied, gel mesh size does not influence MNP velocity. 0.3% w/v agarose has a bulk viscosity that is consistent with that of the skin ECM[14,34] and using it as a medium results the highest MNP velocity. Because of this, all subsequent experiments used 0.3% w/v agarose as the magnetophoretic medium, unless stated otherwise.

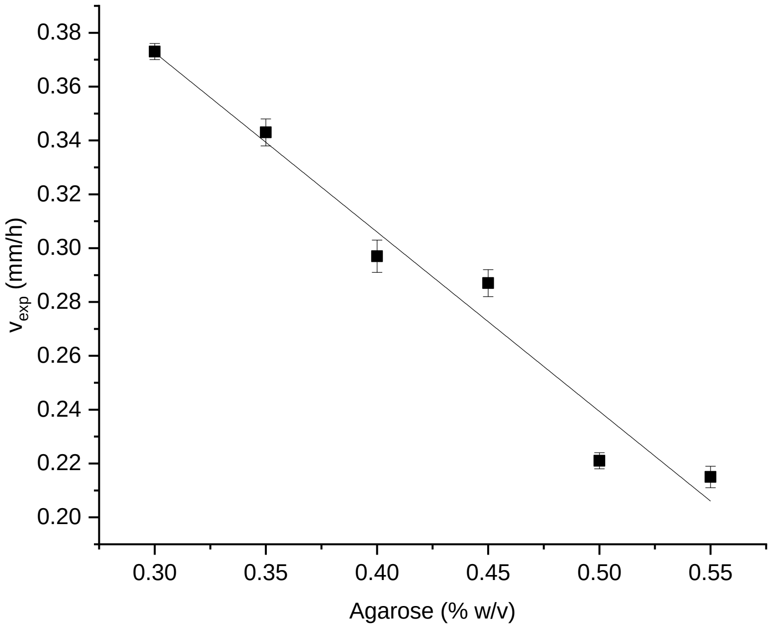

Figure 2.15 v_{exp} values for ~1 mg/ml PEG1000-MNPs (d_{hyd} 24.0 nm (0.16)) in DI H_2O through agarose-H_2O gels with different agarose concentrations, n=3.

A study was undertaken to study the impact of gel depth on magnetophoretic transport. By changing the gel depth, the field strength will also change as it a function of distance. Agarose-H_2O gels of various volumes corresponding to various gel depths between 6 and 24 mm were solidified in glass vials. Citrate-MNPs were magnetophoretically guided through these media for 8 h and imaged every 30 min. Linear transport behaviours were observed at all gel depths over the time, indicating that the field gradients remained constant for each gel depth. v_{exp} values were calculated and plotted as a function of the square root of gel depth (Figure 2.16).

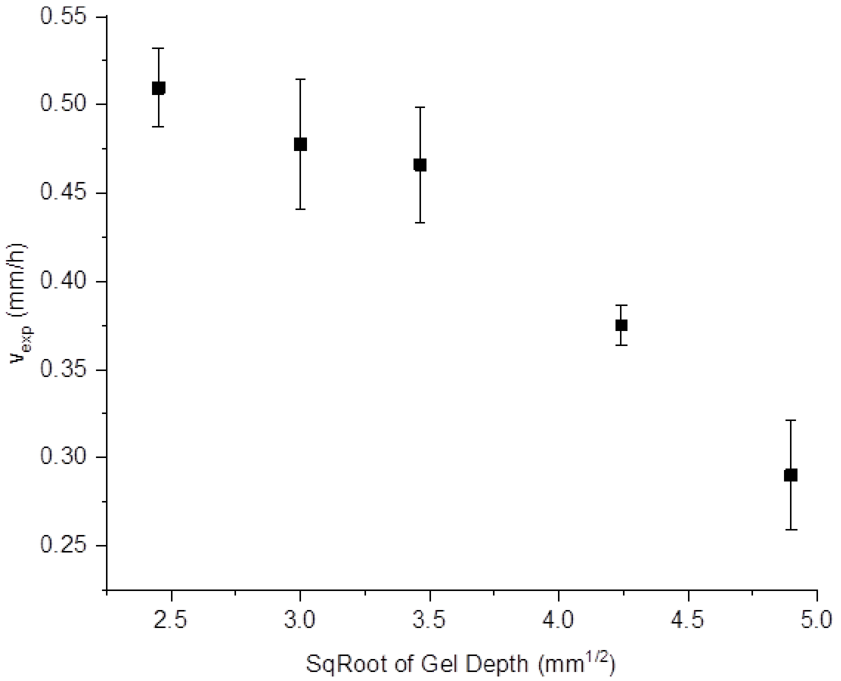

Figure 2.16 v_{exp} values of ~1 mg/ml citrate-MNPs (d_{hyd} 12.1 nm (0.17)) in DI H_2O in agarose-H_2O (0.3% w/v) of varying gel depths (6,9,12,18 & 24 mm). The square root of each of these gel depths is plotted against v_{exp}, n=3.

A linear relationship was observed between v_{exp} and gel depth. The MNPs did not travel the full depth of the higher gel depths and it is likely that at a point after the 8 h of the experiments, the gradient would change and v_{exp} would increase. It can be concluded that the greater the distance between the magnet and the MNPs, the slower the velocity. It would appear that when the gel depth is scaled by a factor of 4, the v_{exp} is halved. This phenomenon is likely due to the change in magnetic responsiveness of the MNP in relation to the changing field strength and gradient. Testing this hypothesis in more gel depths would highlight the ratio between gel depth and v_{exp}. Agarose gel depths of 6 and 12 mm were the optimum depth for maximising v_{exp}. An agarose gel of 6 mm depth was used for all further studies.

2.3.6 Optimisation of magnetic nanoparticles for magnetophoresis

Up to now, it has been shown that it is possible to track bulk MNP transport through a hydrogel under the influence of an external magnetic field using digital imaging. Agarose concentration, depth and magnet positioning have been studied to observe their impact on magnetophoretic transport. Parameters relating to the MNPs were studied here, to understand the impact of concentration, batch to batch variation and whether or not the MNPs damage the agarose during transit.

If MNPs are superparamagnetic they have a single magnetic moment, and should act independently of each other[35]. In this case, the MNPs used have been shown to be superparamagnetic (see Figure 2.9) and therefore, v_{exp} in this case should not be influenced by MNP concentration. To prove this, v_{exp} for different MNP concentrations (0.5, 1, 2 mg/ml) were measured (Table 2.3).

Table 2.3 Tabulated v_{exp} values of PEG1000-MNPs of different concentrations in agarose-H_2O (0.3 % w/v), n=3.

[MNP] (mg/ml)	v_{exp} (mm/h)
0.5	0.369 ± 0.003
1	0.372 ± 0.002
2	0.373 ± 0.003

It was observed that the concentration of the MNPs does not significantly affect v_{exp}, validating their superparamagnetic behaviour observed in Figure 2.9. This result highlights that the MNPs do not aggregate during magnetophoretic transport independent of concentration. The concentration of the MNPs will also influence contrast and hence quality in the digital imaging of the gels. 1 mg/ml was deemed to have maximum contrast and so chosen as the optimum concentration.

The consistency of v_{exp} for different batches of PEG1000-MNPs was investigated. Three different batches of PEG1000-MNPs were synthesised over the course of two weeks. The MNPs were measured by DLS and shown to have a consistent d_{hyd} of 24.1±0.4 nm. To investigate the reproducibility of the MNPs across different batches, transport was studied through agarose-H_2O (Table 2.4). The consistent v_{exp} values for the PEG1000-MNPs demonstrates good reproducibility across the three independent MNP batches.

Table 2.4 Tabulated v_{exp} values of ~1 mg/mL PEG1000-MNPs (24.1±0.1 nm, (0.16)) of different synthesis batches in agarose-H_2O (0.3 % w/v), n=4.

Batch	**v_{exp} (mm/h)**
1	0.371 ± 0.002
2	0.370 ± 0.001
3	0.369 ± 0.002

The final MNP study examined if the MNPs were causing damage to the agarose fibre phase during transit. To investigate this, aliquots of PEG1000-MNPs were magnetophoretically transported through a single gel sequentially to see if previous transits impacted v_{exp} values (Table 2.5). There was a slight increase in v_{exp} after the initial run indicating that that the drag force experienced by the MNPs may have been slightly reduced by causing damage to the agarose fibre network. However, given that the increase is very small, this provides evidence that the MNPs are predominantly being transported in the aqueous phase of the gel (i.e. the water filled pores) as opposed to tunnelling through the polymer fibres. The expected pore diameter range for 0.3% agarose is between 300-600 nm[26,36], an order of magnitude greater than MNP d_{hyd}, which explains why any fibre damage induced during MNP transit is not significant.

Table 2.5 Tabulated v_{exp} values of PEG1000-MNPs through the same agarose-H_2O gel (0.3 % w/v), n=3.

Run	**v_{exp} (mm/h)**
1	0.375 ±0.003
2	0.381 ±0.003
3	0.383 ±0.005

2.3.7 Impact of MNP functionalisation on magnetophoretic transport

A final study was undertaken to measure magnetophoretic velocities of PEG1000, citrate and other surface chemistries through the agarose gel. The magnetophoretic transport of PEG1000, citrate, arginine, DS and boronic acid (BA) were functionalised according to Section 2.2.4. Magnetophoretic transport experiments were carried out on each of these MNP dispersions and v_{exp} values were calculated (Figure 2.17).

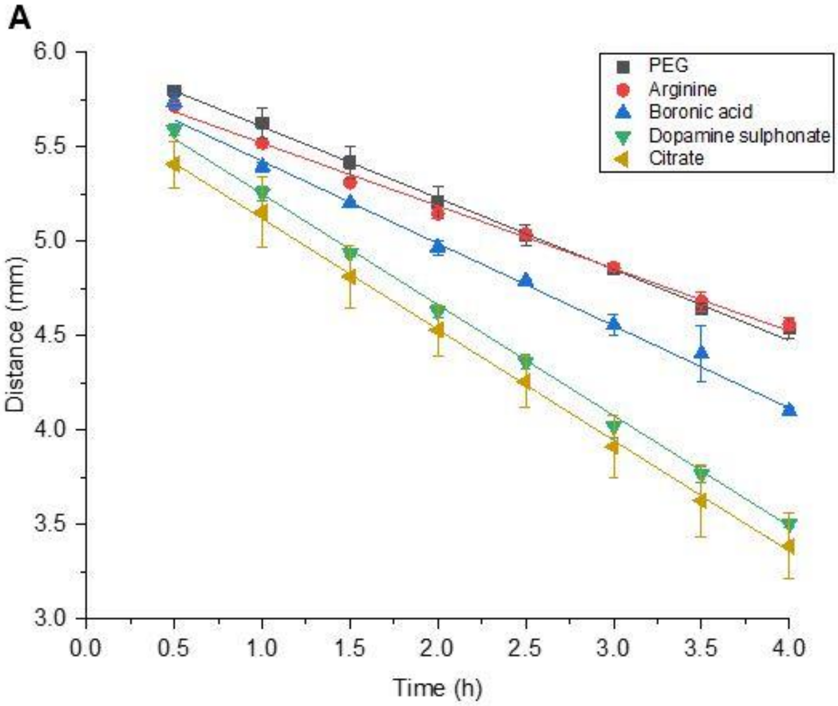

B

Surface chemistry	v_{exp} (mm/h)	ζ_p (mV)	d_{hyd} (nm)
PEG	0.373 ± 0.001	-9.3	24.1
Arginine	0.329 ± 0.003	+30	28.0
Boronic acid	0.436 ± 0.004	-19.5	29.5
Dopamine sulphonate	0.584 ± 0.002	-4.7	10.5
Citrate	0.587 ± 0.10	-27	12

Figure 2.17 A) Magnetophoretic transport of ~1.0 mg/mL MNPs (various surface chemistries) in DI H_2O through agarose-H_2O (0.3% w/v) as a function of time (n=4). B) Tabulated v_{exp} values for each of the different MNP surface chemistries used.

v_{exp} values were observed to vary dramatically as a function of surface chemistry, PEG1000- and arginine-MNPs were observed to be the slowest, BA-MNPs were approx. 30% faster while DS- and citrate-MNPs were found to be fastest. There are various differences between the functionalised MNPs used, e.g., charge, size. These characteristics of a MNP are likely having an effect on magnetophoretic transport behaviour potentially due to interactions with the agarose gel. d_{hyd} values are reported in the table above but it can be seen that these values do not alone explain the differences in v_{exp} values observed. More detailed studies are undertaken in subsequent chapters to understand how significantly MNP characteristics and their interactions with the medium can modulate magnetophoretic transport. In the next Chapter, a subsequent set of experiments were performed to understand what was influencing the velocity at which the MNPs migrate through the agarose gel. Charged MNPs are known to interact with their environment depending on the magnitude and affinity of their surface charge. The magnetophoretic transport of PEG-, citrate- and arginine-MNPs through agarose will be examined.

2.4 Conclusion

In this chapter a digital imaging method was developed to measure magnetophoretic velocities of MNPs through a hydrated gel network. MNP synthesis was carried out whereby three different synthesis protocols based on the Pinna method were compared for iron oxide core synthesis. Microwave digestion was found to yield small uniform MNPs (d_{hyd} 8.9 nm, PDI 0.16). The MNPs were functionalised with a range of surface chemistries including PEG1000 and citrate.

The optimised PEG1000-MNPs were transported through agarose-H_2O using a magnetic field and it was shown that linear behaviour occurred in all magnetophoretic studies. This enabled the calculation of v_{exp} for magnetophoretic transport. For the magnetophoretic study method development, various important parameters were investigated for their impact on MNP transport through agarose-based media. Investigation of certain effects including magnet position, gel depth, bulk viscosity, surface chemistry etc. It was found that viscosity has a direct effect on v_{exp}, as well as the depth of the gel.

The magnetic field gradient was found to be strongest at the corner of the magnet. The agarose gel depth studied showed that the further the distance between the MNPs and the magnet, the slower the measured velocity. The MNPs were independent of concentration effects, indicating the synthesised MNPs were superparamagnetic. This chapter investigated magnetophoresis using functionalised MNPs in an agarose hydrogel acting as a mimic for the ECM. This method was able to obtain reproducible and precise results for magnetophoresis of functionalised MNPs in agarose-H_2O.

In the next chapter, an equation is used to estimate the velocity at which a MNP will travel through a medium of defined viscosity under the influence of an external magnetic field. The electrostatic interactions between a medium containing negative residues and charged MNPs will also be investigated. Understanding the interactions and behaviour a MNP will have in a biological microenvironment is critical for various in vivo applications.

2.5 References

1. Alnaimat, F., Dagher, S., Mathew, B., Hilal-Alnqbi, A. & Khashan, S. Microfluidics Based Magnetophoresis: A Review. *The Chemical Record* **18**, 1596–1612 (2018).
2. Munaz, A., Shiddiky, M. J. A. & Nguyen, N.-T. Recent Advances and Current Challenges in Magnetophoresis Based Micro Magnetofluidics. *Biomicrofluidics* **12**, 031501-01 (2018).
3. Faraudo, J., Andreu, J. S. & Camacho, J. Understanding Diluted Dispersions of Superparamagnetic Particles Under Strong Magnetic Fields: A Review of Concepts, Theory and Simulations. *Soft Matter* **9**, 6654–6664 (2013).
4. Alexander, A. *et al.* Approaches for Breaking the Barriers of Drug Permeation Through Transdermal Drug Delivery. *J. Controlled Release* **164**, 26–40 (2012).
5. Tarn, M. D., Hirota, N., Iles, A. & Pamme, N. On-chip Diamagnetic Repulsion in Continuous Flow. *Sci. Technol. Adv. Mater.* **10**, 01-6 (2009).
6. Leong, S. S., Yeap, S. P. & Lim, J. Working Principle and Application of Magnetic Separation for Biomedical Diagnostic at High- and Low-Field Gradients. *Interface Focus* **6**, 20160048 (2016).
7. Chorny, M., Fishbein, I., Forbes, S. & Alferiev, I. Magnetic Nanoparticles for Targeted Vascular Delivery. *IUBMB Life* **63**, 613–620 (2011).
8. Kye, H. G. *et al.* Dual-Neodymium Magnet-Based Microfluidic Separation Device. *Sci. Rep.* **9**, 1–10 (2019).
9. Pamme, N. & Wilhelm, C. Continuous Sorting of Magnetic Cells via On-Chip Free-Flow Magnetophoresis. *Lab Chip* **6**, 974–980 (2006).
10. Furlani, E. P. Analysis of Particle Transport in a Magnetophoretic Microsystem. *J. Appl. Phys.* **99**, 024912 (2006).
11. Satarkar, N. S. & Hilt, J. Z. Magnetic Hydrogel Nanocomposites for Remote Controlled Pulsatile Drug Release. *J. Control. Release* **130**, 246–251 (2008).
12. Atala, A., Bauer, S. B., Soker, S., Yoo, J. J. & Retik, A. B. Tissue-Engineered Autologous Bladders for Patients Needing Cystoplasty. *The Lancet* **367**, 1241–1246 (2006).
13. Boucard, N. *et al.* The Use of Physical Hydrogels of Chitosan for Skin Regeneration Following Third-Degree Burns. *Biomaterials* **28**, 3478–3488 (2007).
14. Geckil, H., Xu, F., Zhang, X., Moon, S. & Demirci, U. Engineering Hydrogels as Extracellular Matrix Mimics. *Nanomedicine* **5**, 469–484 (2010).
15. Caliari, S. R. & Burdick, J. A. A Practical Guide to Hydrogels for Cell Culture. *Nat Methods* **13**, 405–414 (2016).
16. Salloum, M., Ma, R. H., Weeks, D. & Zhu, L. Controlling Nanoparticle Delivery in Magnetic Nanoparticle Hyperthermia for Cancer Treatment: Experimental Study in Agarose Gel. *Int. J. Hyperthermia* **24**, 337–345 (2008).
17. Mair, L. O. & Superfine, R. Single Particle Tracking Reveals Biphasic Transport During Nanorod Magnetophoresis Through Extracellular Matrix. *Soft Matter* **10**, 4118–4125 (2014).
18. Furlani, E. P. Magnetophoretic Separation of Blood Cells at the Microscale. *J. Phys. D-Appl. Phys.* **40**, 1313–1319 (2007).

19. Pinna, N. *et al.* Magnetite Nanocrystals: Nonaqueous Synthesis, Characterization, and Solubility. *Chem. Mater.* **17**, 3044–3049 (2005).
20. Gupta, A. K. & Gupta, M. Synthesis and Surface Engineering of Iron Oxide Nanoparticles for Biomedical Applications. *Biomaterials* **26**, 3995–4021 (2005).
21. Ninjbadgar, T. & Brougham, D. F. Epoxy Ring Opening Phase Transfer as a General Route to Water Dispersible Superparamagnetic Fe3O4 Nanoparticles and Their Application as Positive MRI Contrast Agents. *Adv. Funct. Mater.* **21**, 4769–4775 (2011).
22. Nigam, S., Barick, K. C. & Bahadur, D. Development of Citrate-Stabilized Fe3O4 Nanoparticles: Conjugation and Release of Doxorubicin for Therapeutic Applications. *J. Mag. Magn. Mater.* **323**, 237–243 (2011).
23. Wei, H. *et al.* Compact Zwitterion-Coated Iron Oxide Nanoparticles for Biological Applications. *Nano Lett.* **12**, 22–25 (2012).
24. Suk, J. S., Xu, Q., Kim, N., Hanes, J. & Ensign, L. M. PEGylation as a Strategy for Improving Nanoparticle-Based Drug and Gene Delivery. *Adv. Drug Deliv. Rev.* **99**, 28–51 (2016).
25. Contreras-Trigo, B. *et al.* Slight pH Fluctuations in the Gold Nanoparticle Synthesis Process Influence the Performance of the Citrate Reduction Method. *Sensors* **18**, (2018).
26. Holligan, D. L., Gillies, G. T. & Dailey, J. P. Magnetic Guidance of Ferrofluidic Nanoparticles in an In Vitro Model of Intraocular Retinal Repair. *Nanotechnology* **14**, 661 (2003).
27. Lake, S. P., Hald, E. S. & Barocas, V. H. Collagen-Agarose Co-Gels as a Model for Collagen-Matrix Interaction in Soft Tissues Subjected to Indentation. *J. Biomed. Mater. Res. A* **99**, 507–515 (2011).
28. Ulrich, T. A., Jain, A., Tanner, K., MacKay, J. L. & Kumar, S. Probing Cellular Mechanobiology in Three-Dimensional Culture with Collagen-Agarose Matrices. *Biomaterials* **31**, 1875–1884 (2010).
29. Feig, V. R., Tran, H., Lee, M. & Bao, Z. Mechanically tunable conductive interpenetrating network hydrogels that mimic the elastic moduli of biological tissue. *Nat. Commun.* **9**, 1–9 (2018).
30. Mustari, A. *et al.* Agarose-based Tissue Mimicking Optical Phantoms for Diffuse Reflectance Spectroscopy. *J. Vis. Exp.* (2018).
31. Fatin-Rouge, N., Starchev, K. & Buffle, J. Size Effects on Diffusion Processes within Agarose Gels. *Biophys. J.* **86**, 2710–2719 (2004).
32. Zucca, P., Fernandez-Lafuente, R. & Sanjust, E. Agarose and Its Derivatives as Supports for Enzyme Immobilization. *Molecules* **21**, (2016).
33. Stellwagen, N. C. & Stellwagen, E. Effect of the matrix on DNA electrophoretic mobility. *J. Chromatogr. A.* **1216**, 1917–1929 (2009).
34. Kuhn, S. J., Hallahan, D. E. & Giorgio, T. D. Characterization of Superparamagnetic Nanoparticle Interactions with Extracellular Matrix in an In Vitro System. *Ann. Biomed. Eng.* **34**, 51–58 (2006).
35. Neuberger, T., Schöpf, B., Hofmann, H., Hofmann, M. & von Rechenberg, B. Superparamagnetic Nanoparticles for Biomedical Applications: Possibilities and

Limitations of a New Drug Delivery System. *J. Magn. Magn. Mater.* **293**, 483–496 (2005).

36. Narayanan, J., Xiong, J.-Y. & Liu, X.-Y. Determination of Agarose Gel Pore Size: Absorbance Measurements vis a vis other Techniques. *J. Phys.: Conf. Ser.* **28**, 83 (2006).

Chapter 3

Theoretical Study and Electrostatically-Modulated Magnetophoretic Transport of MNPs Through Hydrated Polymer Networks

3.1 Introduction

Detailed understanding of the magnetophoretic transport of MNPs, through biological matrices such as the ECM or other collagenous materials[1,2] is a key factor in enabling the realisation of responsive transdermal drug and gene delivery systems, in-vivo target capture[3] and hyperthermic cancer treatment[4]. Particle transport in general in a hydrated polymer matrix such as ECM is influenced by both the physical and chemical nature of the network in several ways; (i) direct electrostatic interactions with matrix fibres for charged particles[5], (ii) direct steric interactions, and (iii) indirect hydrodynamic interactions, i.e. on approaching fibres the restricted motion of water molecules slows particle diffusion. This picture is anticipated for particle motion though any porous network including the ECM and also other polymer structures including hydrogels. Hydrogels can serve as basic physical models of tissue[6,7], for instance as surrogates for brain tissue for infusion studies[8] or mimics of lung or liver tissue for needle insertions studies for surgery[9].

In the case of iron oxide MNPs, inhomogeneous magnetic fields exert a force on the particle proportional to its magnetic volume, to the field strength, and to the gradient of the field[10]. MNPs migrate up the field gradient region, with the opposing drag force governed by properties of the matrix and scaling with the particle (average) d_{hyd}. Significant magnetic forces are required to manipulate movement of MNPs[11], and neodymium alloy or electromagnets can induce sufficient forces over several cm. Hence, as magnetic fields permeate cells and tissue, these fields can be used to guide MNPs through biological tissue. For in vivo and in vitro applications superparamagnetic particles are favoured; their small sizes are likely to minimise tissue damage, the absence of bulk magnetisation at zero field improves colloidal stability and hence shelf life[12]. Magnetophoretic transport of MNPs through porous gels or tissue will be affected by local interactions with polymer chains or ECM, respectively. Specifically, the influence of electrostatic interactions between the surrounding network and the MNPs during magnetophoresis has not yet been described for either hydrogels or ECM to our knowledge. Given the complexity and highly ionic nature of the ECM tissue environment (collagen type I is the most abundant fibrillar protein in connective tissue ECM has ~15–20% ionisable peptide residues)[13], assessment of the electrostatic impact on magnetophoretic motion in simpler charged porous media is required for development of more advanced matrices for magnetophoretic applications.

By equating the magnetic and drag forces, theoretical terminal velocities of MNPs in biological tissue mimics moving in a magnetic field gradient have been previously calculated to support experimental findings. For example, a study based on measuring and predicting the terminal velocity of MNPs through purified ECM matrix was carried out by Kuhn et al[14], and was discussed in detail in Chapter 1. An earlier study by Holligan et al.[15] also studied magnetophoretic transport of iron oxide MNPs in agarose gels (a model for vitreous humour) using magnetic forces[18] and was also discussed in Chapter 1.

In the previous chapter, the motion of functionalised MNPs moving through an agarose gel medium under the influence of an external magnetic field was studied. All MNP suspensions exhibited linear displacements with time under the conditions tested, confirming the attainment of a terminal magnetophoretic (experimental) velocity, v_{exp}. v_{exp} values were measured with high reproducibility. In this chapter, an equation based on relating magnetic and drag forces derived from previously reported literature was used to predict theoretical velocities (v_{th})[14,15] for MNPs undergoing magnetophoresis according to the method developed in Chapter 2. The v_{exp} values were found not to be consistent with v_{th} values, according to this equation which was based on a simple model using the viscosity experienced by the MNPs during transport through the aqueous phase of the polymer network. In this work, a factor was introduced, φ, to account for the tortuous path provided by the polymer network that MNPs experience during magnetophoresis. This modified equation was then used to assess the effect of electrostatic interactions on magnetophoresis. It was found that in the absence of the influence of electrostatic interactions, a single tortuosity value could be used to account for a given agarose content. Critically, MNP surface charge was found to modulate magnetophoretic velocity, with positively charged MNPs travelling faster and negatively charged MNPs travelling slower than predicted. A model for particle transport through porous networks comprised of hydrophilic polymer chains in water is proposed wherein interactions at the pore constrictions (entrances and exits) determine the electrostatic contribution to magnetophoretic velocity. The implications of electrostatic modulation for magnetophoretic-driven movement of particles in porous polymeric networks such as tissue are discussed.

3.2 Materials & methods

3.2.1 Materials

Iron acetylacetonate (14024-18-1), benzyl alcohol (100-51-6), GLYMO (2530-83-8), PEG MW400, MW1000, MW2070 (25322-68-3), acetone (67-64-1), sodium citrate tribasic(III) (6132-04-3), chloroform (67-66-3), THF (109-99-9), potassium hydroxide (1310-58-3), hydrochloric acid (7647-01-0), agarose (9012-36-6) (low electroendosmosis (EEO)) (0.09-0.13), agarose (medium EEO) (0.16-0.19), agarose (high EEO) (0.23-0.26), aqueous ammonia (1336-21-6) and PBS tablets (78392) were all purchased from Sigma-Aldrich. L-arginine (74-79-3) was purchased from Biochemika Int. A 50 mm x 25 mm grade N52 neodymium magnet (F335-N52) was used for all magnetophoresis studies and was purchased from www.first4magnets.com.

3.2.2 Instrumentation

Details as described per Section 2.2.2.

3.2.3 MNP functionalisation

Details as described per Section 2.2.4

3.2.4 Agarose gel preparation

Details described as per Section 2.2.5. For agarose gel with differing EEO content, the necessary agarose was substituted. High EEO agarose needed twice the required time to fully dissolve.

3.2.5 Experimental determination of MNP magnetophoretic velocities (v_{exp})

Details described as per Section 2.2.6.

3.2.6 Theoretical calculation of magnetophoretic velocities (v_{th})

The forces that determine MNP dynamics in homogeneous media of defined viscosity are F_D and F_M. When these two forces are equal, and no other forces are present, a constant or terminal MNP velocity is achieved. Agarose-H_2O gels used in this study are biphasic materials comprising hydrated porous polymer networks with the mesh size dependent on the agarose concentration. Hence, the appropriateness of applying a continuum model for the forces operating to interpret transport in these circumstances is not certain. Nevertheless, relations have been proposed to describe MNP transport through a viscous medium in an external magnetic field gradient[14,15]. Based on previous studies[14,15], Equation 3.1 is proposed to calculate v_{th}, of the MNPs through agarose-H_2O gels of known viscosity under the influence of an external magnetic field gradient.

$$v_{th} = \frac{\chi_v V_m}{2r_{hyd}} . \frac{B\nabla B}{\mu_0} . \frac{1}{3\pi\eta} \qquad (3.1)$$

In this equation, the contributions are grouped (from the left) into those relating to the MNPs, the magnetic force, and the medium/matrix. χ_v is the volumetric magnetic susceptibility (0.281 determined by magnetometry), V_m is the volume of superparamagnetic material in a particle (3.69 x 10^{-25} m^3 determined by TEM, r_{hyd} is the hydrodynamic radius of the MNP (m) taken here from DLS; B is the magnetic field strength (specified to be 0.55 T by the distributor), ∇B is the gradient of the magnetic field (45 T m^{-1})[14], μ_0 is the permeability of free space (4π x 10^{-7} T m A^{-1}) and η is the viscosity of the surrounding fluid, in this case water (0.00089 Pa.s).

The % difference (%D) between v_{exp} and v_{th} can be calculated according to Equation 3.2.

$$\%D = \frac{v_{exp} - v_{th}}{v_{th}} \text{ x } 100 \qquad (3.2)$$

This equation will enable the comparison of v_{th} with the magnetophoretic velocity of the MNPs as they move through the agarose. In theory, the v_{th} should match the v_{exp} if all factors that could influence magnetophoretic transport of the MNPs have been considered. If the %D value is positive or negative will be key in the understanding of what possible interactions may be causing this difference.

3.3 Results & Discussion

3.3.1 Magnetophoretic transport of PEG1000-MNPs in agarose

Magnetophoretic transport of PEG1000-MNPs through agarose-H_2O gels was studied under specific conditions and a v_{exp} value of 0.374 mm/h was measured previously (Section 2.3.4). Using Equation 3.1, a v_{th} value was calculated to be 0.0149 mm/h. It was assumed transport of the MNPs is limited to the aqueous phase and thus experiences only the local viscosity of water. However, using this equation, the v_{th} value calculated is approx. 25 times lower than the v_{exp} value. This was initially surprising, as all parameters in the equation have been measured and accounted for. In Equation 3.1, no parameter accounts for the polymer chains present that would be expected to provide a resistance to MNP transport. Agarose gel comprises a fibre network (defining a bulk viscosity) and an aqueous phase present in the pores of the fibre network (defining a local viscosity). The combination of these two phases result in a tortuous pathway that the MNPs must traverse, when migrating in a magnetic field. This tortuous pathway will be inversely proportional to v_{exp}. The tortuosity is defined as the ratio of effective path length to linear path length. It is dependent in this instance on agarose concentration, which correlates directly with average mesh size. The expected mesh size in this range of agarose is 300-600 nm. Holligan et al.[15], proposed a scaling factor to account for this tortuous pathway (φ) of the agarose hydrogel. A tortuosity value of 0.4 was given to signify the pathway that the MNPs must traverse in a 0.6% w/v agarose gel.

Given that Equation 3.1 did not account for this tortuosity, v_{th} would be faster than expected. However, this was not what was observed in this work. In this work, equation 3.3 is proposed as a modification of equation 3.1 to include a factor describing the tortuosity of the system φ, whereby φ increases for highly tortuous paths (one might consider that $1/\varphi \rightarrow 0$ for increasingly tortuous paths and $1/\varphi \rightarrow 1$ for free diffusion).

$$v_{th} = \frac{\chi_v V_m}{2r_{hyd}} \cdot \frac{B\nabla B}{\mu_0} \cdot \frac{1}{3\pi\varphi\eta} \qquad (3.3)$$

Using equation 3.3, reasonable agreement was possible between v_{exp} and v_{th} using $\varphi = 0.04$. This value was set as the factor required to equate v_{exp} to v_{th} for PEG1000-MNPs which are assumed to be transported solely through the aqueous phase of the network, with no interactions with polymer network. The combination of η and φ can be used to account for the impact of the matrix on magnetophoretic transport. This product reflects an effective viscosity representing the averaged restriction to MNP motion through a connected tortuous pore path. While the two contributions, η and φ, cannot be separated by magnetophoretic measurements, we suggest that the choice of η_{H2O}, suggesting a bulk-like drag force for MNPs within the pores, is useful as it provides a φ value that is reflective of the pore connectivity.

3.3.2 Effect of agarose concentration on magnetophoretic transport

MNPs functionalised with PEG are known to have weak interactions with hydrated polymer matrices due to repulsive steric effects and their near neutral surface charge[16]. To study the effect of the network density on PEG1000-MNP transport, v_{exp} values were measured for different agarose concentrations. In all cases the MNP front moved linearly over the same distance range as before. As agarose concentration was increased, v_{exp} was found to decrease approximately linearly for more dense networks, as expected. Using the extracted v_{exp} values and the measured viscosity for each gel the tortuosity factor, ϕ, was determined for each sample (Figure 3.1). It is found that ϕ increases with agarose concentration (more tortuous paths) as expected.

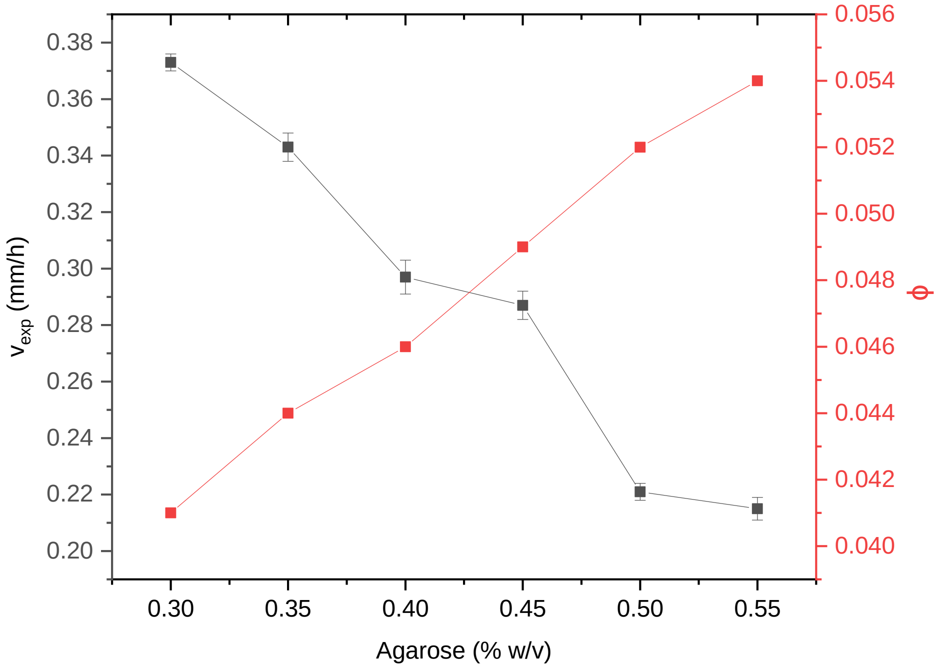

Figure 3.1 v_{exp} and corresponding φ values obtained for ~1.0 mg/mL PEG1000-MNP dispersions (d_{hyd} 24.0 nm (0.16)) in DI H_2O, when magnetophoretically transported through agarose-H_2O (n=4) of varying % w/v.

Over the agarose content range studied, average pore diameters are anticipated to be 300-600 nm[17–19], which is at least an order of magnitude greater than the d_{hyd} values of the MNPs. It is clear that path tortuosity and/or particle graft/network chain entanglement effects are significant for all the gels studied, suggesting that the size of the open pores is not limiting. Previously reported agarose-based ECM mimics used agarose content between 0.3 and 0.6% w/v[15,20]. To maintain a high pore volume (to minimise any pore volume effects on transport) and to maintain high v_{exp}, (so that changes in velocity are more easily measured) for the remainder of the current study 0.3% w/v agarose gels were studied.

In order to observe the physico-chemical factors that influence magnetophoretic motion; MNPs were grafted with PEG of increasing chain length (400, 1000, 2070 MW). The d_{hyd} value was observed to increase with increasing chain length (in the range of 21 – 28 nm) and it was found that v_{exp} decreased with chain length (Table 3.1). This confirms that hydrodynamic size is a primary factor determining transport; we can infer that the magnetic force is similar in each case as there is a single core per particle. The ϕ value extracted for these three suspensions was found not to vary significantly, as expected, hence a value of 0.04 can be taken as representative of the path through 0.3% w/v agarose-H_2O (using η of 0.00089 Pa.s) for suspensions of particles that are not electrostatically stabilised. There may be a small change in the φ value extracted on increasing the chain length. This is difficult to confirm given the precision of the experiments. However, it is correlated with a slight increase in ζ_p (Table 1), which suggests the need to fully assess the effect of MNP surface charge on magnetophoretic transport.

Table 3.1 Magnetophoretic parameters for transport of ~1.0 mg/mL PEG-MNPs dispersions in DI H_2O through agarose-H_2O (0.3% w/v).

PEG mw (Da)	d_{hyd} (nm)	PDI	ζ_p (mV)	v_{exp} (mm/h)	v_{th} (mm/h)	φ
400	21.5	0.17 ± 0.01	-8.6 ± 0.1	0.41 ± 0.01	0.0171	0.041
1000	24.0	0.16 ± 0.01	-9.2 ± 0.4	0.37 ± 0.02	0.0149	0.040
2070	28.0	0.19 ± 0.02	-9.7 ± 0.5	0.32 ± 0.01	0.0128	0.040

3.3.3 Electrostatic effects arising from biphasic network on magnetophoretic transport

The effect of ζ_p on MNP magnetophoretic transport through agarose-H_2O gels (0.3% w/v) was investigated by varying the surface coating of the MNPs. PEG1000-, arginine- and citrate- functionalised MNPs were prepared, see Section 2.2.4. The PEG1000-MNP suspensions were anticipated to be sterically stabilised and were found to have a weakly negative ζ_p (-9.0 mV at pH 7.4), arginine-MNPs were found to have a strongly positive ζ_p (+30 mV), while citrate-MNPs had a strongly negative ζ_p (-27 mV). This data is summarised in Table 3.2.

Table 3.2 Magnetophoretic parameters for transport of ~1.0 mg/mL PEG1000-, arginine-, and citrate-MNP dispersions in DI H_2O through agarose-H_2O (0.3% w/v). Colloidal properties of the same dispersions are included.

Surface chemistry	d_{hyd} (nm)	PDI	ζ_p (mV)	v_{exp} (mm/h)	v_{th} (mm/h)	%D
PEG1000	24.0	0.16 ± 0.01	-9.3 ± 0.1	0.37 ± 0.02	0.37	+0
Arginine	28.0	0.17 ± 0.01	+30 ± 1.0	0.35 ± 0.01	0.32	+8.5
Citrate	12.0	0.18 ± 0.01	-27 ± 1.4	0.63 ± 0.02	0.75	-19

For arginine-MNPs ($\zeta_p > 0$), taking the tortuosity, φ, to be unchanged a %D in the experimental velocity of +8.5% was determined (equation 2), i.e. arginine-MNPs move significantly faster than predicted when compared to PEG1000-MNPs ($\zeta_p \leq 0$) of similar d_{hyd}, demonstrating the influence of surface charge. In the case of the citrate-MNPs ($\zeta_p < 0$), %D was negative (-19%). Note that citrate-MNPs had a lower d_{hyd} than PEG1000 or arginine equivalents and v_{exp} was observed to be greater, but by significantly less than is predicted by equation 1. In all cases, as noted above, a single core per particle is assumed and the measured d_{hyd} value used for calculating v_{th}. Hence, we can attribute the negative %D for citrate-MNPs to surface charge as opposed to size effects, an interpretation we confirm below. In summary, significant positive or negative %D values are associated with large positive or negative ζ_p values, respectively, demonstrating the importance of electrostatic interactions between the MNPs and the network chains.

In order to confirm that the functionalised MNPs remained and acted as individual particles during transport, the MNPS were analysed by DLS (Table 3.3). MNPs were extracted from the bottom of the gel after full transit had taken (>12 h) and washed with DI H_2O before being analysed by DLS. The lack of significant change in d_{hyd} shows that partial clustering or aggregation is not occurring for any of the functionalised MNPs. It is also likely that clustering is not taking place during transit as no significant change in v_{exp} is observed.

Table 3.3 DLS measurements for PEG1000-, citrate- and arginine-MNPs suspensions before and after transit through the agarose gel.

	Before transit through agarose		**After transit through agarose**	
Surface chemistry	d_{hyd} (nm)	ζ_p (mV)	d_{hyd} (nm)	ζ_p (mV)
PEG1000-	24.1	-9.3	24.0	-9.2
Citrate-	12.2	-27.2	12.1	-27.1
Arginine-	28.0	+30.1	28.0	+29.9

3.3.3.1 Effect of agarose anionic residues on magnetophoretic transport

Agarose gels are formed from polysaccharides with the same basic structure but with different substituting groups. The EEO content of the gels is related to the concentration of anionic residues, ester sulphate and pyruvate, present[21]. To further investigate the role of electrostatic interactions between MNPs and the hydrated network during magnetophoresis, three different agarose-H_2O gel classes were used. The EEO was varied and classed as low, medium and high (Aga/Low, Aga/Med, Aga/High, see Section 3.2.4. The magnetophoretic response of three MNP suspensions (PEG1000-, arginine- and citrate-) were tested using each of the three agarose classes. Again, linear transport, the attainment of terminal velocity over the range studied, was observed in all cases. The data is summarised in Figure 3.2, in this case the velocities are normalised with respect to d_{hyd} of the relevant suspension

(v_{exp}*d_{hyd}) to correct for size effects. Note that in all cases d_{hyd} for the recovered suspensions was found to be unchanged after passing through the gels.

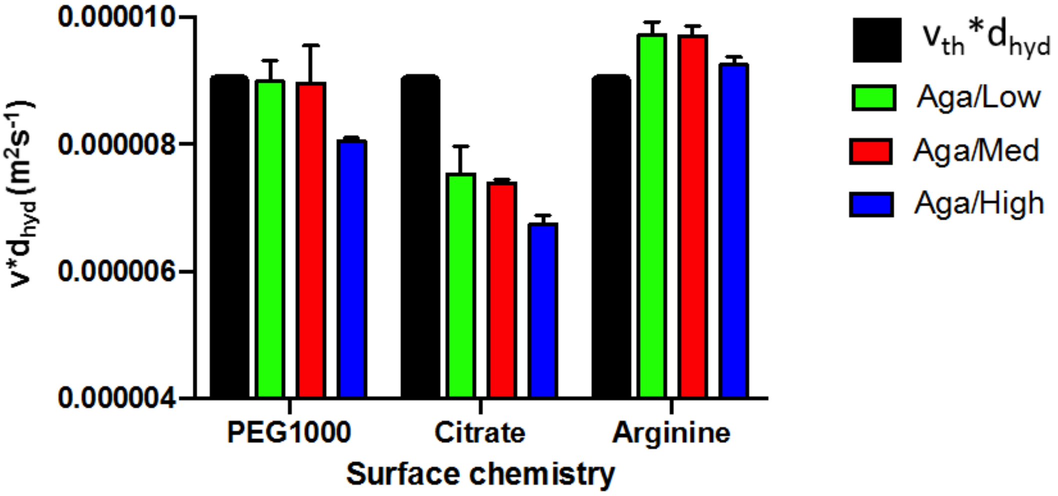

Figure 3.2 Normalised magnetophoretic velocities, v_{exp}*d_{hyd}, for PEG1000, citrate-, and arginine-MNP suspensions through the different classes of agarose-H_2O (Aga/Low, Aga/Med, Aga/High) (0.3% w/v). Error bars are included for all functionalised MNPs. The v_{th}/d_{hyd} values are represented as black bars.

The normalised velocities (v_{exp}*d_{hyd}) for each of the functionalised MNPs in Aga/Low, Aga/Med and Aga/High were seen to have similar charge dependence to the suspensions shown in Table 2; arginine-MNPs moved faster and citrate-MNPs moved slower than PEG1000-MNPs, irrespective of the network charge density. Interestingly, at the highest concentration of fixed anionic charges the normalised velocities of all MNPs decreased, suggestive of an increase in electrostatic interactions between the MNPs and the agarose.

3.3.3.2 Effect of IS on magnetophoretic transport and particle interactions

For agarose-H_2O, the Debye length (λ_D), of the charges along the network chains is anticipated to be at a maximum. Increasing IS of the medium will reduce λ_D for the charges on the network chains and the MNP bound ligands and so should influence magnetophoretic transport. Magnetophoretic velocities were measured for transport of PEG1000-, citrate-, arginine-MNPs through Aga/High gels prepared at different IS, again terminal velocities were measured and the results are summarised in Figure 3.3. Note that the d_{hyd} values of the MNP suspensions were independent of IS across the range studied. It was found that on increasing IS the velocity of the almost neutral PEG1000-MNPs remained unchanged, consistent with minimal electrostatic interactions with the network irrespective of IS. The velocity of negatively charged citrate-MNPs, which was lower than v_{th} in agarose-H_2O, was found to progressively increase with increasing IS, and the velocity of positively charged arginine-MNPs, higher than v_{th} in DI H_2O, was found to progressively decrease. For both electrostatically stabilised suspensions the normalised velocities approach v_{th} (fixed φ of 0.04, corresponding to the path tortuosity observed for PEG-MNPs) at higher IS, presumably as electrostatic interactions are largely suppressed.

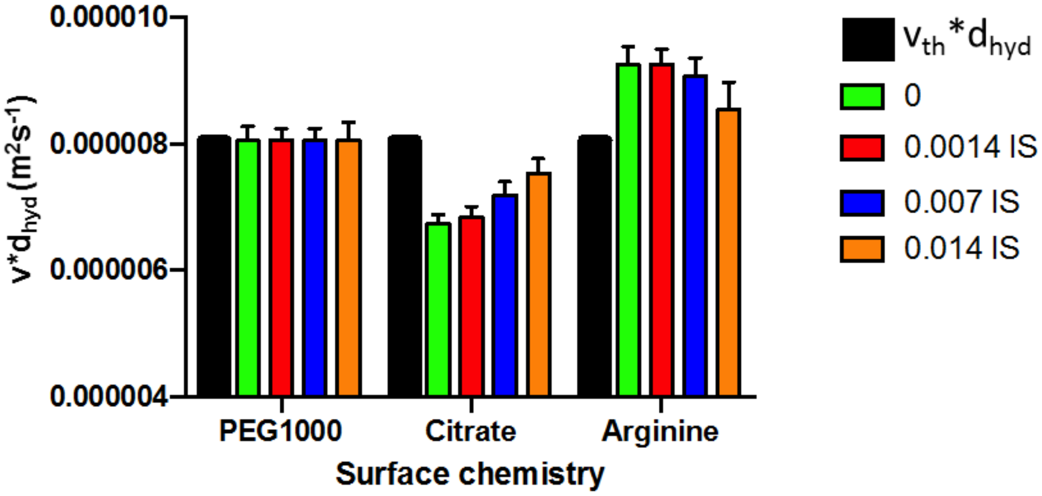

Figure 3.3 Normalised magnetophoretic velocities, v_{exp}*d_{hyd}, for PEG1000-, arginine- and citrate-MNP suspensions through agarose-PBS (Aga/High, 0.3% w/v). MNP suspensions and agarose gels were prepared in PBS buffer to give IS of 0, 0.0014, 0.007 and 0.014 at pH 7.0. The v_{th}/d_{hyd} values are represented as a black bar.

We suggest that during magnetophoresis, negatively charged citrate-MNPs are located predominantly towards the centre of the pores in the agarose-PBS gel due to electrostatic repulsion with the pore entrances and walls. The presence of a depleted free void volume close to the pore walls reduces the MNP concentration (and hence flux) and/or reduces the free path, as a result v_{exp} is found to be lower than expected (negative %D, Table 3.2 and Figure 3.4). On increasing IS, λ_D is decreased and these electrostatic effects are reduced, increasing v_{exp} for citrate-MNPs (Figure 3.3). For arginine-MNPs the relative magnetophoretic velocity was greater than expected (positive %D, Table 3.2 and Figure 3.4) and decreased with increasing IS. When moving through the network, positively charged arginine-MNPs should undergo attractive interactions with the pore walls. Again, on increasing the IS, these electrostatic effects are reduced, decreasing v_{exp} for arginine-MNPs. Given the large mesh sizes it is likely that these effects, which modulate v_{exp} significantly, occur at the pore constrictions (entrances/exits).

3.3.4 Effect of polymer chain residue manipulation on magnetophoretic transport

The observation that repulsive interactions impede citrate-MNP transport and attractive interactions enhance arginine-MNP transport through the pores is reminiscent of the exclusion enrichment (EE) effect previously described[12,13], for molecular motion in charged nanofluidic channels. For example, Plecis et al.[22], reported that for channels with dimensions ranging from 2-250 nm, the permeability for small anions and cations undergoing purely electrophoretic transport depends on channel charge as well as the IS of the medium, with reduced motion for anions which are constrained to the channel centre, and enhanced motion for the counter-cations[22], largely due to the concentration dependence of the flux. Both effects were found to be suppressed at higher IS.

A similar picture emerges for magnetophoretic transport of charged MNPs though negatively charged agarose pore networks; a schematic representation of pore transport is shown in Figure 3.4. It is suggested that the electrostatic effect is more pronounced at the pore entrances/exits, where the physical constriction is more comparable to those in nano-channels. Electrostatic effects in soft materials such as polymer gels can be greater than those observed for rigid materials[23], due to their dynamic nature allowing the charges to be flexible forming mobile electrostatic clouds[22], and hence would be expected to exert a strong effect at the constrictions. In the scheme the electric double layer (EDLs) of the anionic charges of the pore walls form an electrostatic cloud at the entrance of the pore. For negatively charged citrate-MNPs at low IS (A) repulsive electrostatic forces slow particle movement through the pore. At high IS (B), the EDLs on both the charged MNPs and at the pore entrances are decreased, reducing repulsion and increasing flux through the pore under the influence of the magnetic force. Essentially this is due to an increase in the free void volume of the pore. For positively charged arginine-MNPs at low IS (C), attractive electrostatic forces between the particles and the fixed negative sites enhance MNP transport through the pore, effectively the EE effect. At high IS (D) reduced EDL overlap weakens this effect reducing MNP velocity.

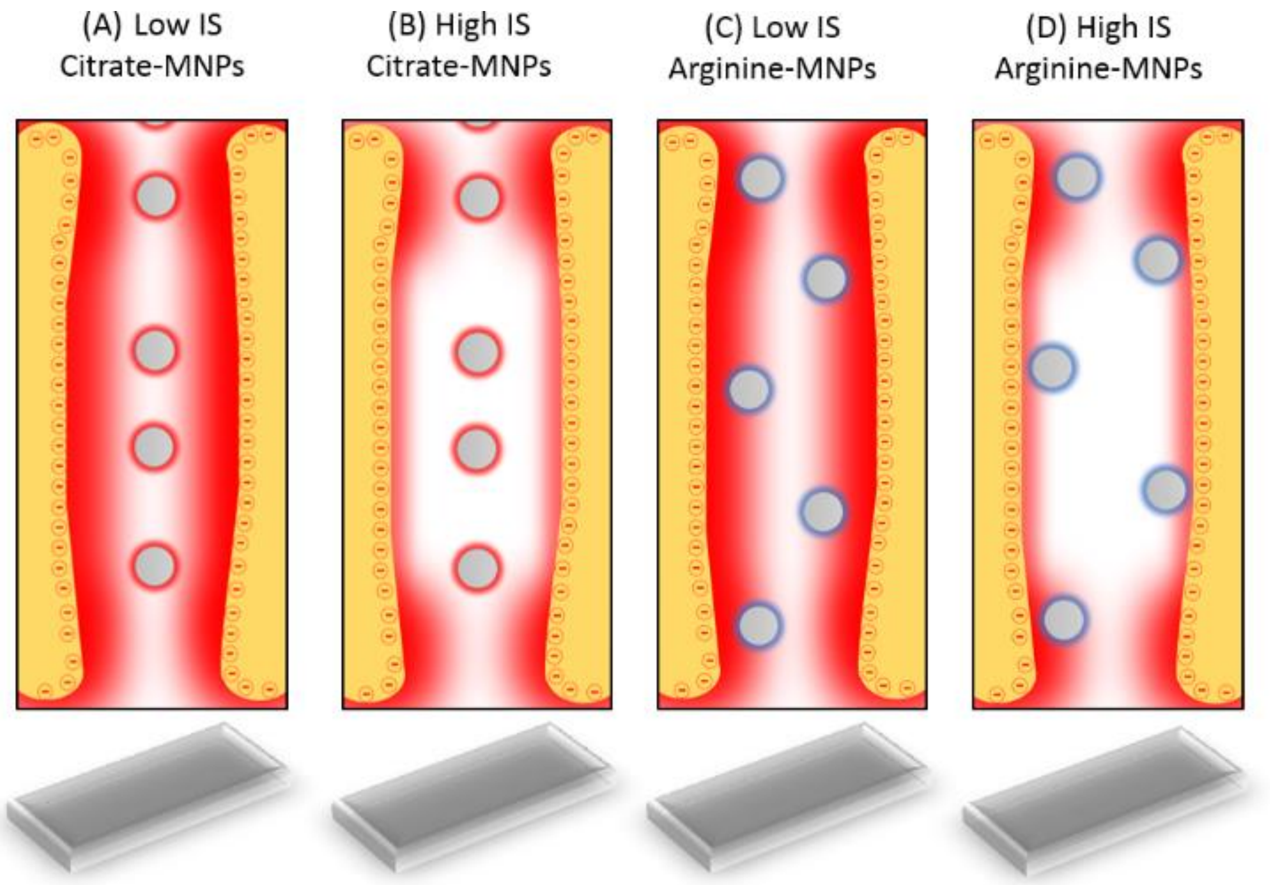

Figure 3.4 Schematic representation of transport of citrate- and arginine-MNPs through a pore in agarose-PBS gels in low and high IS media.

It is important to note that in smaller pores, these electrostatic effects may not be observed. This has been observed where the channel is similar in size scale to the moving particle. A study by Bruno et al.[24], investigated the effect of channel size on charged particles moving through a microfluidic system. When the channel size decreased to 5 nm, an abrupt drop in diffusion through the channel was observed for all molecules. They state that this result is due to a charge-independent transport only observed in small channels. There is also another consideration to take into account, that in smaller porous networks in agarose. It is known that MNPs can deposit themselves on the fibre structure of the polymer phase. This is regardless of charge of the MNP, although some functionalisation's may help avoid this behaviour.

Finally, the magnetophoretic transport of positively charged arginine-MNPs through Aga/Low and Aga/High gels in both low and high IS media were measured. The data is summarised in Table 3.4. The differences in velocity are small in this case, so it is difficult to draw strong conclusions. However, for both EEO types increasing IS reduced v_{exp}, as before, this is again consistent with weaker favourable interactions at the constrictions. However, for both IS values reducing EEO, which should suppress favourable interactions, resulted in an increase in v_{exp}. This suggests the two effects are not strictly additive, but that IS as the more dominant factor for arginine-MNPs, perhaps because higher IS leads to a reduction in λ_D on both the MNPs and the fixed anionic residues.

Table 3.4 Magnetophoretic parameters for transport of ~1 mg/mL arginine-MNP dispersions in agarose-PBS of varying IS through the different classes of agarose (0.3% w/v) (Aga/Low, Aga/High).

Experiment No.	**IS**	**Agarose class (EEO)**	**v_{exp} (mm/h)**	**v_{th} (mm/h)**	**%D**
1	Low (0.0014)	Low	0.35 ± 0.01	0.32	+8.5
2	High (0.014)	Low	0.32 ± 0.02	0.32	0
3	Low (0.0014)	High	0.33 ± 0.01	0.32	+3
4	High (0.014)	High	0.31 ± 0.01	0.32	-3

Similar data recorded for citrate-MNP suspensions supports the suggestion that IS is predominant factor (Table 3.5). High EEO and low IS increased v_{exp}, consistent with weaker unfavourable interactions at the constrictions. The increase in IS leads to a direct increase in v_{exp}, whereas the addition of more anionic residues in high EEO decreases v_{exp}. These results are a mirror of the trend observed for the positively charged arginine-MNPs. This indicates that electrostatics in a charged medium can be manipulated to enhance or hinder a MNP depending its charge.

Table 3.5 Magnetophoretic parameters for transport of ~1 mg/mL citrate-MNP suspension in agarose-PBS of varying IS through agarose gels (0.3% w/v) of different EEO.

Experiment No.	IS	Agarose class (EEO)	v_{exp} (mm/h)	v_{th} (mm/h)	%D
1	Low (0.0014)	Low	0.63 ± 0.01	0.75	-19
2	High (0.014)	Low	0.66 ± 0.02	0.75	-12
3	Low (0.0014)	High	0.65 ± 0.01	0.75	-13.3
4	High (0.014)	High	0.68 ± 0.01	0.75	-9.3

3.4 Conclusion

A detailed study into magnetophoretic transport of charged MNPs through agarose hydrogels was undertaken. The equation used to calculate theoretical velocities, a factor was proposed to account for the tortuosity of the agarose hydrogel, φ and allowed for v_{th} values to be in agreement with v_{exp} values (Equation 3.3). It was possible to focus on the response of the gel, which is parameterised by the product $\eta\varphi$. This provided a measure of the matrix influence on MNP transport. This product represented the averaged restriction to magnetophoretic transport through a connected tortuous pore path. While the two contributions, η and φ, cannot be separated by measuring magnetophoretic transport it was suggested that the choice of water viscosity, demonstrates a bulk-like drag force for MNPs within the pores, is useful as it provided a φ value that was reflective of the pore connectivity[15]. This view is supported by the monotonic increase in φ with agarose % w/v (Figure 3.1), by the single φ value extracted for 0.3% w/v agarose when only d_{hyd} is varied, and by the collapse of the velocities measured for arginine- and citrate-MNP suspensions back to close to this value when the charge interactions (associated primarily with passage through the pore constrictions) are sufficiently suppressed.

For electrostatically stabilised MNPs we have observed a soft hydrogel equivalent of the EE effect that is established for transport of charged molecules through hard nano-pores. Negatively charged MNPs are forced to the centre of the pore constrictions and travel slower than near-neutral MNPs. Positively charged MNPs are attracted by the chains at the constriction and travel faster. These effects can be suppressed by tuning the λ_D. IS adjustment allows v_{exp} to be reduced by approx. 8%, for arginine-MNPs and to be increased by approx. 11%, for citrate-MNPs (for high EEO agarose). Detailed analysis of the interplay of fixed charge content and IS suggested that the latter is the critical factor in determining magnetophoretic transport through pore restrictions.

The picture that emerged for magnetophoretic transport was a complex interplay of surface charge, pore volume and pore constriction factors combining to effect the magnetophoretic response[32-35]. It was demonstrated that it was possible to modulate terminal velocities during magnetophoretic transport significantly.

3.5 References

1. Koester, K. J., Ager, J. W. & Ritchie, R. O. The True Toughness of Human Cortical Bone Measured with Realistically Short Cracks. *Nat. Mater.* **7**, 672–677 (2008).
2. Wang, X., Bank, R. A., TeKoppele, J. M. & Agrawal, C. M. The Role of Collagen in Determining Bone Mechanical Properties. *J. Orthop. Res.* **19**, 1021–1026 (2001).
3. Friedman, A. D., Claypool, S. E. & Liu, R. The Smart Targeting of Nanoparticles. *Curr. Pharm. Des.* **19**, 6315–6329 (2013).
4. Chatterjee, D. K., Diagaradjane, P. & Krishnan, S. Nanoparticle-Mediated Hyperthermia in Cancer Therapy. *Ther. Deliv.* **2**, 1001–1014 (2011).
5. Stylianopoulos, T. *et al.* Diffusion of Particles in the Extracellular Matrix: The Effect of Repulsive Electrostatic Interactions. *Biophys. J.* **99**, 1342–1349 (2010).
6. Murphy, N. P. & Lampe, K. J. Mimicking Biological Phenomena in Hydrogel-Based Biomaterials to Promote Dynamic Cellular Responses. *J. Mater. Chem. B* **3**, 7867–7880 (2015).
7. Tibbitt, M. W. & Anseth, K. S. Hydrogels as Extracellular Matrix Mimics for 3D Cell Culture. *Biotechnol. Bioeng.* **103**, 655–663 (2009).
8. Chen, Z.-J. *et al.* A Realistic Brain Tissue Phantom for Intraparenchymal Infusion Studies. *J. Neurosurg.* **101**, 314–322 (2004).
9. Tan, Z., Dini, D., Rodriguez y Baena, F. & Forte, A. E. Composite Hydrogel: A High Fidelity Soft Tissue Mimic for Surgery. *Materials & Design* **160**, 886–894 (2018).
10. Williams, C. *et al.* Cardiac Extracellular Matrix-Fibrin Hybrid Scaffolds with Tunable Properties for Cardiovascular Tissue Engineering. *Acta Biomater.* **14**, 84–95 (2015).
11. Lim, J., Yeap, S. P., Che, H. X. & Low, S. C. Characterization of Magnetic Nanoparticle by Dynamic Light Scattering. *Nano. Res. Lett* **8**, 381 (2013).
12. Tokarev, A., Yatvin, J., Trotsenko, O., Locklin, J. & Minko, S. Nanostructured Soft Matter with Magnetic Nanoparticles. *Adv. Funct. Mater.* **26**, 3761–3782 (2016).
13. Freudenberg, U. *et al.* Electrostatic Interactions Modulate the Conformation of Collagen I. *Biophys. J.* **92**, 2108–2119 (2007).
14. Kuhn, S. J., Hallahan, D. E. & Giorgio, T. D. Characterization of Superparamagnetic Nanoparticle Interactions with Extracellular Matrix in an In Vitro System. *Ann Biomed. Eng.* **34**, 51–58 (2006).
15. Holligan, D. L., Gillies, G. T. & Dailey, J. P. Magnetic Guidance of Ferrofluidic Nanoparticles in an In Vitro Model of Intraocular Retinal Repair. *Nanotechnology* **14**, 661 (2003).
16. Ninjbadgar, T. & Brougham, D. F. Epoxy Ring Opening Phase Transfer as a General Route to Water Dispersible Superparamagnetic Fe3O4 Nanoparticles and Their Application as Positive MRI Contrast Agents. *Adv. Funct. Mater.* **21**, 4769–4775 (2011).
17. Suk, J. S., Xu, Q., Kim, N., Hanes, J. & Ensign, L. M. PEGylation as a Strategy for Improving Nanoparticle-Based Drug and Gene Delivery. *Adv. Drug Deliv. Rev.* **99**, 28–51 (2016).

18. Narayanan, J., Xiong, J.-Y. & Liu, X.-Y. Determination of Agarose Gel Pore Size: Absorbance Measurements vis a vis other Techniques. *J. Phys.: Conf. Ser.* **28**, 83 (2006).
19. Viovy, J.-L. Electrophoresis of DNA and Other Polyelectrolytes: Physical Mechanisms. *Rev. Mod. Phys.* **72**, 813–872 (2000).
20. Ulrich, T. A., Jain, A., Tanner, K., MacKay, J. L. & Kumar, S. Probing Cellular Mechanobiology in Three-Dimensional Culture with Collagen-Agarose Matrices. *Biomaterials* **31**, 1875–1884 (2010).
21. Stellwagen, N. C. & Stellwagen, E. Effect of the Matrix on DNA Electrophoretic Mobility. *J. Chromatogr. A.* **1216**, 1917–1929 (2009).
22. Plecis, A., Schoch, R. B. & Renaud, P. Ionic transport Phenomena in Nanofluidics: Experimental and Theoretical Study of the Exclusion-Enrichment Effect on a Chip. *Nano Lett.* **5**, 1147–1155 (2005).
23. Wu, S. *et al.* Composite Hydrogel-Loaded Alumina Membranes for Nanofluidic Molecular Filtration. *J. Membr. Sci* **477**, 151–156 (2015).
24. Bruno, G. *et al.* Unexpected Behaviors in Molecular Transport Through Size-Controlled Nanochannels Down to the Ultra-Nanoscale. *Nat. Commun.* **9**, 1682 (2018).

Chapter 4

Magnetophoretic Transport of Functionalised Iron Oxide Nanoparticles Through Collagen-Based and Cultured ECM Gels

4.1 Introduction

The ECM is the non-cellular component present in all biological tissues, providing a physical scaffold for other cellular constituents[1]. The ECM regulates the biochemical and biomechanical cues required for tissue morphogenesis, differentiation and homeostasis[2]. The ECM is of great interest for biodiagnostic applications, as biomarkers are found in higher concentrations when compared to other biological matrices[3]. The ECM is composed of two classes of macromolecules: fibrous proteins and a non-fibrous matrix composed of proteins (proteoglycans and other glycoproteins). Fibrous proteins in the ECM include collagen, elastin and fibronectin[4]. Collagen is the main structural protein in ECM, which provides tensile strength, regulates cell adhesion and aids in tissue development[1]. Elastin fibres provide recoil for tissues that undergo repeated stretching (muscles, skin)[5]. Elastin is tightly associated with the collagen fibrous network. Fibronectin is involved in the organisation of the interstitial ECM by regulating cell attachment and function[6].

Inside the collagen fibrous network, lies the interstitial space. This space is occupied by a non-fibrillar matrix formed by proteoglycans and interstitial fluid (ISF). Proteoglycans fill the interstitial space within the fibrous network to form a second structural network[7]. Proteoglycans have a variety of functions that use their unique buffering, hydration, binding and force-resistance properties for the ECM. ISF is the aqueous component of the ECM and plays an important role within the human body[8]. The interstitial space comprises approx. one-sixth of the body volume and mediates the exchange of oxygen, nutrients and waste products between the vascular system and cells[9]. The composition of the ISF varies by location within the body, containing a mixture of interstitial water, proteins and salts[10,11], namely phosphate, lactate, sulphate, magnesium, calcium, sodium, potassium and albumin[12,13]. Considering the importance of the ECM and ISF to so many fundamental cellular processes, a myriad of tissue-culture models have been developed to study the interplay between its biochemical and biophysical properties, and to understand the molecular origins of cellular behaviours regulated by ECM ligation[14].

Hydrogels are used to mimic the ECM, whereby a variety of natural and synthetic polymers are used as these hydrogels[15]. Collagen, hyaluronic acid, fibrin, agarose and alginate are commonly used natural polymers for tissue mimics and engineering[16–19]. Commonly used synthetic polymers for ECM mimics include PEG, PVA and poly (2-hydroxyethyl methacrylate). To fabricate the fibrous structures of the ECM, several fabrications methods can be used including electro-spinning, phase separation and self-assembly. Electro-spinning uses an electric field to melt a polymer solution (e.g. polycaprolactone, PVA or polyacrylonitrile[20,21]), and generates a continuous charged jet stream that solidifies upon hitting a substrate to form a non-woven fibrous mat. These mats are often used as scaffolding for growth of cells[21]. The next approach is phase separation, whereby the separation of two phases (e.g. polymer and aqueous phase) can be triggered when a homogeneous dual-component system (e.g. dissolved polymer in solvent) becomes thermodynamically unstable under certain conditions (e.g. change in temperature) and separates into a biphasic system[22].

An example of this is whereby agarose is dissolved in an aqueous phase at an elevated temperature and when this solution is cooled to room temperature (20 °C), phase separation occurs to produce a polymer-rich phase (agarose fibres) and a polymer-lean phase (H_2O)[23]. The polymer-rich phase is used to replicate the fibrous microstructures present in the ECM[15,23,24].

Self-assembly, the third method, is defined as the spontaneous organisation of components into patterns or structures by an external trigger. One such example is the self-assembly of collagen fibrils that structure themselves into fibres that form a network. Self-assembly is triggered by raising the temperature of an unorganised collagen solution to 37°C. The resulting self-assembled structures are maintained by non-covalent bonds[25]. Although non-covalent bonds such as hydrogen bonds, ionic bonds, and hydrophobic interactions are weak in isolation, in concert they govern the self-assembly of biological macromolecules[26].

The most abundant structural protein of ECM is collagen[27,28]. To improve biological, biophysical and mechanical characteristics of tissue mimics, combinations of polymers are often used, for example, collagen combined with agarose. Ulrich et al.[29], reported an agarose/collagen hydrogel and investigated the effect of agarose concentration on collagen fibre network formation. The agarose/collagen gels were prepared by adding collagen (1.5 mg/ml), agarose (2% w/v) and a trace amount of sodium hydroxide to Dulbecco’s modified Eagle’s medium. This was incubated at 37°C to trigger collagen self-assembly followed by agarose gelation. It was found that increasing the concentration of agarose increased the elasticity of the collagen fibres, changing the way the fibril network formed. As such, a combination of polymers can mimic the multiple fibrillar microstructures present in the ECM. The agarose was then used to mimic the non-fibrillar matrix present inside the collagen networks within the ECM.

Another study by Lake et al.[30], also investigated the structural effect that the non-fibrillar material around the collagen network plays in the same agarose/collagen gels prepared using the same method[29]. It was found that agarose added to collagen formed a fine web-like matrix, which was interspersed among the collagen fibres. Agarose did not alter the formation or structural topology of the collagen network, nor did the self-assembly of collagen fibres disrupt agarose gelation. These two processes happen sequentially, the collagen self-assembly takes place, then the agarose network solidifies inside the established collagen network. The addition of agarose improved collagen mechanical and structural properties in this study.

Collagen forms the base network that provides tensile strength to the ECM, while other fibrillar proteins in ECM form networks around the collagen. The use of collagen in ECM mimics enables good fibrillar microstructure formation, a distinct physical property of ECM. Agarose mimics the non-fibrillar matrix that forms within the interstitial space of the ECM. By combining polymers to mimic both the fibrillar and non-fibrillar structures, it allows for a more representative physical structure of the ECM in tissue (Figure 4.1).

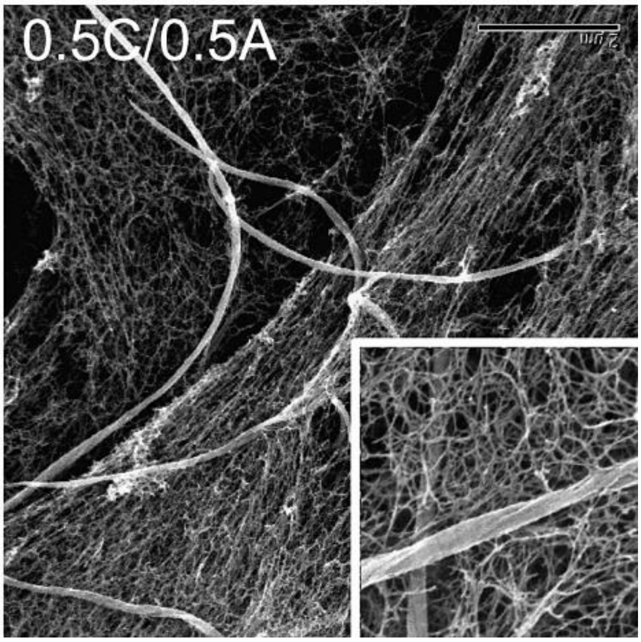

Figure 4.1 Scanning electron microscopy (SEM) imaging of collagen–agarose gels synthesised by a self-assembly process. Agarose forms a web-like network between the entangled collagen fibres that becomes progressively denser as the concentration of agarose is increased, agarose (0.5 % w/v) in a 0.5 mg/ml collagen gel (0.5 % w/v). Scale bar: 2 µm (main panels) and 500 nm (insets)[29].

Manipulating NPs in ECM tissue can be challenging due to the presence of fibrillar and non-fibrillar proteins[31-32]. As demonstrated in Chapters 2 and 3, MNPs can be magnetophoretically guided through basic hydrated polymer networks whereby agarose acted as a basic mimic for the ECM network, whereby it is assumed that they are limited to the aqueous phase of the gels. However, one limitation of this experimental approach has been that the gels investigated did not incorporate an extracellular protein component, limiting their representation of the ECM environment. Another important factor for magnetophoretic studies for in vivo applications is the consideration of the strength of the magnetic field being used. The magnetic field strength will influence the gradient and susceptibility of the MNPs. Up to now, a neodymium magnet of strength 0.23 T has been used (N52) which is similar in strength to what has been reported in the literature. For instance, MNPs (starch, chitosan, lipid and PEG (d_{hyd} 100-1000 nm)) were transported under an external magnetic field of 0.4 T through excised rat tissue over a distance range of 5-7 mm[33]. It was shown that the chitosan-MNPs (d_{hyd} 100 nm) penetrated the tissue the furthest in this study, attributed to their positive charge and their interactions with the tissue environment. Other studies have used similar field strengths of 0.23 T in ECM[31] and 0.16 T in agarose[34] to induce MNP motion.

In previous chapters, magnetophoresis was carried out in agarose as a basic mimic for the ECM. In this chapter, collagen gels were investigated where the fibrillar structure by way of collagen protein is represented. Magnetophoretic transport of functionalised MNPs was studied in agarose/collagen gels and cultured ECM (prepared from Engelbrecht-Holm-Swarm murine sarcoma). Linear magnetophoretic transport was observed for agarose/collagen and ECM gels, MNP velocities were calculated and discussed in the context of our understanding of transport behaviour in earlier chapters. Furthermore, in previous chapters, a low magnetic field strength magnet (N52, 0.23 T) was used for motion studies. In the work here, a higher field strength magnet (Giamag, 1.1 T), was investigated to understand its impact on MNP magnetophoresis.

4.2 Materials & methods

4.2.1 Materials

Collagen Type IV from bovine skin (9007-34-5), Dulbecco's Modified Eagle Medium (DMEM) (143-74-8), ECM gel liquid prepared from Engelbrecht-Holm-Swarm murine sarcoma (E1270), isopropyl alcohol (67-63-0) were purchased from Sigma Aldrich. All other materials used are listed in earlier chapters.

4.2.2 Magnets

A N52 neodymium magnet was used for low field magnetophoretic experiments and is referred to as N52 in this chapter. A customised magnet from Giamag Technologies (accessed through Prof. Brougham, University College Dublin) was used for high field magnetophoretic experiments and is referred to as Giamag in this chapter. The Giamag was comprised of several strips of neodymium encased in a diamagnetic material, causing the field gradient to be concentrated in a single area. This concentrated gradient is expressed at the top of the Giamag (Figure 4.2), which is not covered with diamagnetic material. It possesses a strong magnetic field (1.1 T) over a small concentrated field gradient.

See Section 2.2.2 for details of all other instrumentation used in this chapter.

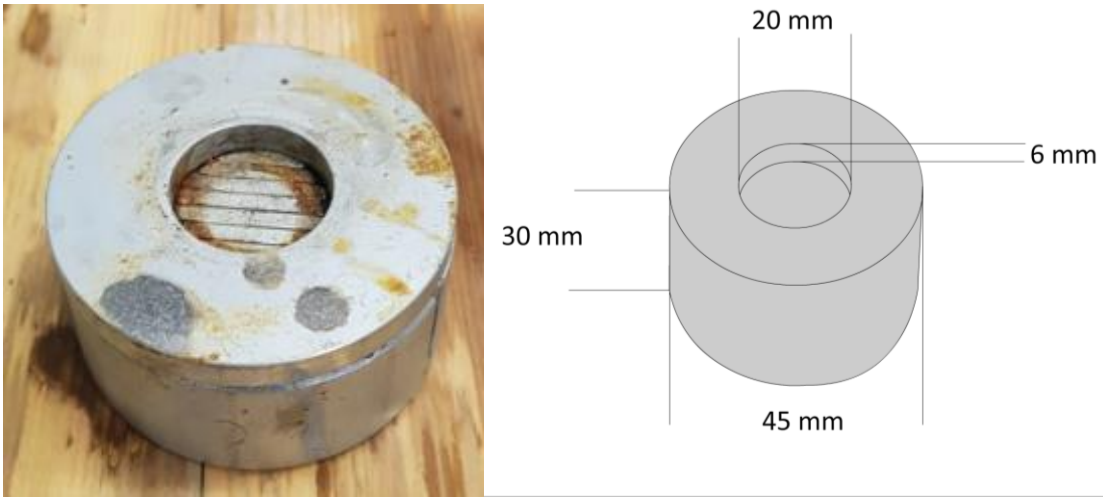

Figure 4.2 Image of the Giamag (left) with dimensions shown (right).

4.2.3 MNP synthesis and functionalisation

MNP synthesis was performed as per Section 2.2.3.3. PEG1000-, citrate- and arginine- functionalisation protocols are described as per Section 2.2.4.

4.2.4 Extracellular matrix mimic preparation

4.2.4.1 Agarose-interstitial fluid

Agarose gels were prepared as per Section 2.2.5, whereby instead of dissolved agarose in DI H_2O, synthetic ISF was used. To prepare synthetic ISF, calcium chloride (0.222 g), HEPES (2.383 g), glucose (0.99 g), potassium chloride (0.261 g), magnesium sulphate (0.084 g), sodium chloride (7.188 g), monosodium phosphate (0.179 g), and saccharose (0.31 g) were added to a 1 L volumetric flask, filled to the mark with DI H_2O and stirred vigorously for 1 h to ensure all components had fully dissolved. The pH of the synthetic ISF was measured to be 7.4.

4.2.4.2 Agarose/collagen

Agarose was dissolved in DI H_2O or synthetic ISF (Agarose/collagen-H_2O or agarose-collagen/ISF respectively) as previously described, and 600 µL of agarose solution was added to a glass vial (instead of 700 µL). Agarose solutions were kept in the oven for 2 h at 37°C. 100 µL of stock collagen solution (1 mg/ml) was then added to each vial and vortexed for 30 s. The glass vial was then placed back into the oven at 37 °C for 1 h to induce self-assembly of the collagen fibres[29]. The gel was removed from the oven and left to solidify for 1 h at room temperature. The vial was then refrigerated at 4 °C until required. All gels were allowed to reach room temperature before use.

4.2.4.3 In-vitro extracellular matrix

Prior to handling ECM, all workplace surfaces were washed down with isopropyl alcohol to ensure a sterile environment. ECM liquid was removed from the freezer and thawed overnight at 4°C. 700 µL of the solution was transferred to a 7 mL glass vial. The vial was stored for 12 h at 4°C to allow release of trapped air. The ECM was then incubated at 37°C for 40 min to induce ECM polymerisation by self-assembly processes (Figure 4.3). ECM gels were used within 24 h of being prepared to avoid degradation. All glassware was treated with methanol to ensure sterility to avoid contamination.

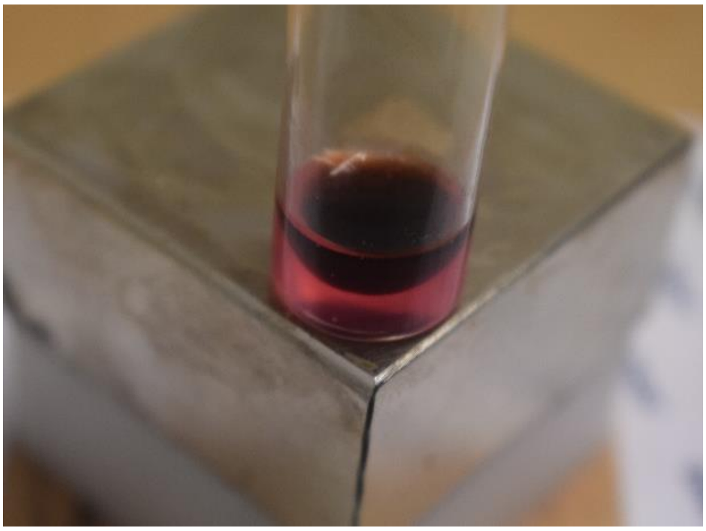

Figure 4.3 Cultured ECM in glass vial placed on N52.

4.2.5 Magnetophoretic studies

A glass vial containing either agarose-ISF, agarose/collagen-ISF or ECM was placed directly in the centre of the Giamag or on a corner of the N52, as specified. MNPs were then transferred to the top of the gels to allow transport through the gels. In the case of the Giamag, the vials were removed from the magnet at specified time intervals and imaged to measure MNP front position. In the case of the N52, the vials were imaged in situ.

4.3 Results & Discussion

4.3.1 Magnetophoretic transport studies in agarose-ISF

In Chapter 3, the influence of electrostatic interactions on magnetophoretic transport of MNPs was observed in agarose. Briefly, the presence of the fixed negatively charged groups in agarose decreased the v_{exp} of negatively charged MNPs and increased the v_{exp} of the positively charged MNPs. By increasing the IS of the aqueous phase of the gel, the EDLs on both the MNPs and the agarose fibres decreased which led to relative increases in v_{exp} for the negatively charged MNPs and relative decreases in v_{exp} for the positively charged MNPs.

In this study, it was investigated if the same behaviour would be observed using synthetic ISF (IS 0.16 M) as agarose solvent in place of PBS (IS 0.14 M). Experiments were performed and linear velocities were observed for all MNPs throughout the full agarose-ISF gel depths. v_{exp} values were calculated and compared to v_{exp} values for agarose-H_2O (previously reported in Chapter 2) (Table 4.1). The EDLs of the fixed anionic charges on the agarose chains are expected to be similar in strength to those of agarose-PBS and weaker than those in agarose-H_2O.

Table 4.1 v_{exp} values for ~1 mg/mL PEG1000- (d_{hyd} 24.1 nm (0.16)), arginine- (d_{hyd} 28.0 nm (0.16)), and citrate-MNPs (d_{hyd} 12.1 nm (0.17)), through agarose-H_2O (0.3 % w/v), agarose-PBS (IS 0.14) and agarose-ISF (IS 0.16), n=4, R^2>0.99 for all data sets.

Surface Chemistry	v_{exp} in agarose-H_2O (mm/h)	v_{exp} in agarose-PBS (mm/h)	v_{exp} in agarose-ISF (mm/h)
PEG1000	0.374 ± 0.01	0.372 ± 0.02	0.371 ± 0.02
Arginine	0.348 ± 0.02	0.311 ± 0.02	0.315 ± 0.01
Citrate	0.632 ± 0.02	0.673 ± 0.04	0.684 ± 0.03

The impact of using synthetic ISF was consistent with the results observed in PBS in Chapter 3 (Table 1). v_{exp} of PEG1000-MNPs was not impacted by the presence of ISF when compared to PBS or H_2O, while the v_{exp} of arginine-MNPs decreased on account of high IS. Citrate-MNPs experienced an increased v_{exp} in ISF compared to H_2O, again fully consistent with what was observed previously for citrate-MNPs in agarose-PBS. This study shows, that the presence of synthetic ISF in agarose gels influenced v_{exp} in the manner expected. It is attributed to a decrease in EDLs on the MNPs and the fixed anionic charges on the agarose fibres compared to H_2O, modulating the influence of the EE effect on both negatively and positively charged MNPs.

4.3.2 Magnetophoretic transport studies in agarose/collagen-ISF

Collagen was combined with agarose[29] to assemble gels (agarose/collagen-ISF) comprising of the fibrillar network and the non-fibrillar matrix to more closely resemble the structure of ECM. In this case, the agarose component of the gel was at the same concentration as before (0.3%) but was solidified in the presence of self-assembled collagen fibres. Agarose/collagen-ISF hydrogels were prepared according to Ulrich et al.[29], and as described in Section 4.2.4.2. Synthetic ISF was used as the aqueous phase, again to more closely resemble the ECM environment. The resulting gels were expected to be homogenous with a greater tortuosity when compared to agarose-ISF on account of the collagen fibres formed as the network. While no morphological characterisation of the gels was performed in this work, based on the literature, the diameters of the collagen fibres is expected to be in the range of 20-50 nm in diameter [35–37]. Within the aqueous phase of these gels, it is important to consider that there may be residual collagen oligomer present which could increase phase viscosity[38]. These change in viscosity and tortuosity of the gel compared to agarose alone would likely result in an increase in the product $\eta\varphi$ in equation 3.3, relevant for calculating v_{th} values for MNPs.

To investigate the effect of the presence of the collagen on magnetophoretic transport, experiments were carried out using PEG1000-, arginine- and citrate-MNPs (Figure 4.4). It was observed that none of the MNPs penetrated the surface of the gels instantaneously as expected (as observed previously for all agarose-based gels), but instead remained on the surface of the gel within spherical droplets for a period of time before a front could be observed moving into the bulk gel. Collagen self-assembly is driven by the hydrophobicity effect and may thus be plausible that at the air-water interface, the self-assembled collagen has a greater hydrophobic character at the surface of the gel due to the absence of water, explaining the delayed penetration. It was noted that after ~1 h the spherical droplet began to collapse in all cases, overcoming the required surface energy to wet the surface. Time-based differences were observed for the penetration of the different MNPs (Figure 4.4).

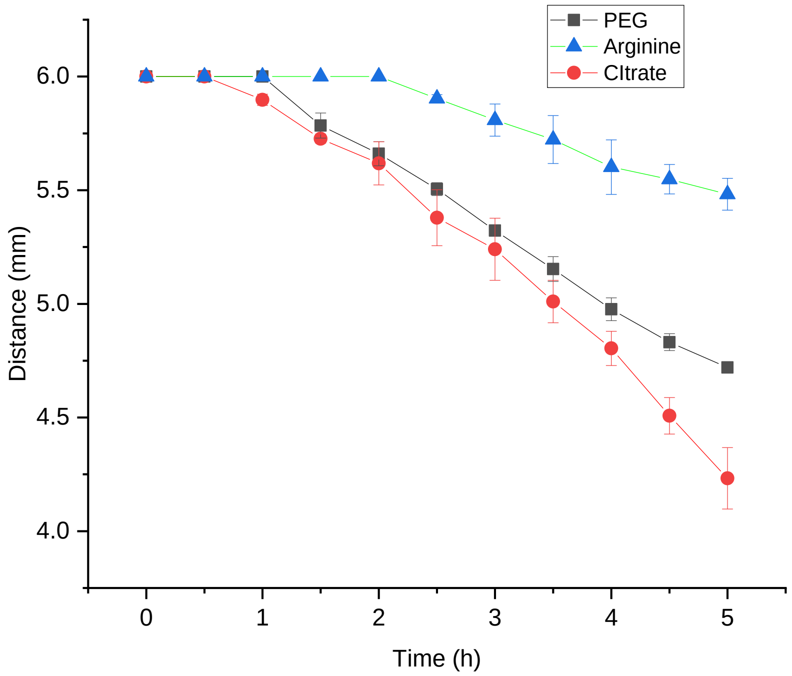

Figure 4.4 Magnetophoretic transport of 0.5 mg/mL PEG1000-MNPs (d_{hyd} 24.0 nm) arginine-MNPs (d_{hyd} 28.0 nm), and citrate-MNPs (d_{hyd} 12.0 nm) dispersions in DI H_2O through agarose/collagen-ISF gels (0.3 %w/v, low EEO), n=4. R^2 > 0.98 in all cases after penetration into the gel.

PEG1000-MNPs took approx. 1.5 h to penetrate the gel, which was faster than arginine-MNPs by approx. 1 h but slower than citrate-MNPs by less than 0.5 h. Given that the d_{hyd} of PEG1000-MNPs is close to that of arginine-MNPs, MNP size cannot fully explain the behaviour observed. PEG is less polar in nature than the charged MNPs, which may explain the earlier penetration time than would be expected based solely on size.

Arginine-MNPs took longest to penetrate the gel (approx. 2 h) and are the largest of all the MNPs (d_{hyd} 28 nm) (Figure 4.4). The combination of this large d_{hyd} combined with surface hydrophobicity effects, this could explain arginine-MNPs taking the longest to penetrate the surface.

Citrate-MNPs penetrate the agarose/collagen-ISF surface after 30 min**.** They are the smallest of the MNPs (d_{hyd} 12 nm) and as such, may be the reason they penetrated the surface at the earliest timepoint.

Linear regression was performed on the data in Figure 4.4 for each surface chemistry once penetration into the gel had taken place and a terminal velocity reached. v_{exp} values in this agarose/collagen-ISF gel were compared to v_{exp} values obtained previously from transport in agarose-ISF (Table 4.2) whereby decreases in v_{exp} values were observed for all surface chemistries. The addition of collagen to agarose is likely to change gel character, described by the viscosity and tortuosity (ηφ), which could partly explain decreases in v_{exp} observed[39].

Table 4.2 v_{exp} values for ~1 mg/mL PEG1000- (d_{hyd} 24.1 nm), arginine- (d_{hyd} 28.0 nm), and citrate-MNPs (d_{hyd} 12.1 nm), through agarose/collagen-ISF (0.3 % w/v) and agarose-ISF gels, n=4.

Surface Chemistry	v_{exp} in agarose/collagen-ISF (mm/h)	v_{exp} in agarose-ISF (mm/h)	v_{exp} change (%)
PEG1000	0.322 ± 0.02	0.371 ± 0.02	-13.2
Arginine	0.155 ± 0.02	0.315 ± 0.01	-50.8
Citrate	0.462 ± 0.03	0.684 ± 0.03	-32.5

The v_{exp} of PEG1000-MNPs decreased by 13.2% in agarose/collagen-ISF when compared to v_{exp} in agarose-ISF. As PEG would not be expected to interact significantly with the network, this decrease was attributed to the increased ηφ of the gel. It is plausible that there are weak interactions between the zwitterionic residues of the collagen and the charges on the MNPs taking place. Although collagen has a net charge close to zero, the individual charges on the collagen may interact electrostatically over short timescales with the positive or negative changes on the MNPs resulting in an equivalent impact on both the citrate and the arginine and no effect for the neutral PEG1000-MNPs.

Taking this into account the arginine-MNP v_{exp} decreased dramatically (-50.8%) compared to arginine in agarose-ISF. By subtracting the influence of ηφ in agarose/collagen (-13.2%) from the v_{exp} decrease, a -37.6% change is observed for the arginine-MNPs. The interactions between the individual charges on the collagen fibres and the arginine-MNPs work to slow their v_{exp}. Studies have shown that collagen fibres interact with charged molecules even though it has an overall neutral charge[32,33,38]. This significant decrease in v_{exp} could be due to the d_{hyd} of the MNPs or the orientation of exposed charges on the collagen after fibril formation[40].

Citrate-MNPs also exhibited a decrease in v_{exp} (-32.5%), in agarose/collagen-ISF compared to agarose-ISF, again most likely due to the increase in ηφ of the gel. Given that the difference is larger than what was observed for PEG1000, it is likely that there is also another factor at play, similar to the arginine-MNPs. By subtracting the influence of ηφ (13%) from the v_{exp} decrease, a -19.3% change is observed for the citrate-MNPs. This is consistent with the theory of the electrostatic interactions between the collagen fibre network and the charged MNP surface.

It is important to note, that after the citrate-MNPs penetrate 1.5 mm into the agarose, a notable increase in v_{exp} is observed. The v_{exp} increases from 0.462 mm/h to 0.571 mm/h for the citrate-MNPs. This is the first time this behaviour is observed for any MNP in any gel. The field gradient has shown to be constant in previous experiments, so it is assumed that this is still the case here. The agarose/collagen gels have shown to exhibit different properties at the gel surface, it may be possible that the gel is not homogenous. It is plausible that the gel further from the surface may be collagen-lean when compared to the initial gel area near the surface.

Potential future experiments to confirm this theory involve measuring v_{exp} of PEG1000- and arginine-MNPs over a longer timeframe to observe if they accelerate after 1.5 mm of gel has been traversed as observed for the citrate-MNPs. These experiments provide evidence that electrostatic behaviour from the presence of collagen modulates magnetophoretic transport in collagen-agarose networks. Further studies will be needed to fully understand why the individual charges on the collagen fibre interact more with certain surface chemistries than others.

Another way to analyse the data for magnetophoretic transport through agarose/collagen gels is to eliminate the influence of the ISF observed in Table 4.1. This led to a -8% difference in v_{exp} for arginine-MNPs and a + 8% difference in v_{exp} for citrate-MNPs. If we account for this difference in Table 4.2 for arginine- and citrate MNPs, a %D between v_{exp} and v_{th} is -42% and -40% respectively. This data agrees with published literature that collagen will interact with charged species in an equal manner[41]. Irrespective of the details, the presence of collagen leads to a decrease in v_{exp} for all surface chemistries. It is plausible to state that this is due to an increased ηφ and interactions between the collagen fibres and the charged MNPs.

4.3.3 Magnetophoretic transport studies in ECM

Cultured ECM represents a substantially different environment compared to agarose-based gels. The ECM is mainly comprised of fibrillar proteins like laminin, collagen type IV and non-fibrillar proteoglycans including negatively charged proteoglycans such as heparin sulphate[5]. Proteoglycans are responsible for maintain hydration within the ECM by the binding of counter-ions such as sodium[38].

The cultured ECM used for this work is derived from Engelbrecht-Holm-Swarm murine sarcoma. The collagen IV and other proteins in the ECM form the structural network, where the interstitial space is filled with peptides, non-fibrillar proteins and other biomolecules. These biomolecules include the negatively-charged bound and free proteoglycans (hyaluronic acid, dermatan sulphate, chondroitin sulphate and heparan sulphate for example)[42]. Once assembled, it is assumed to be homogenous and, given its composition will likely have a significantly different $\eta\varphi$ when compared to previously studied agarose and agarose/collagen hydrogels.

To investigate magnetophoretic transport in this cultured ECM media, MNPs (100 µL) were deposited on the ECM surface. The MNP dispersion droplet was observed to collapse immediately indicating the ECM surface had a higher surface energy (e.g. greater hydrophilicity) than agarose/collagen-ISF. All MNPs penetrated the surface immediately and were linearly transported magnetophoretically through the ECM, exhibiting the typical front profile observed previously in agarose (Figure 4.5).

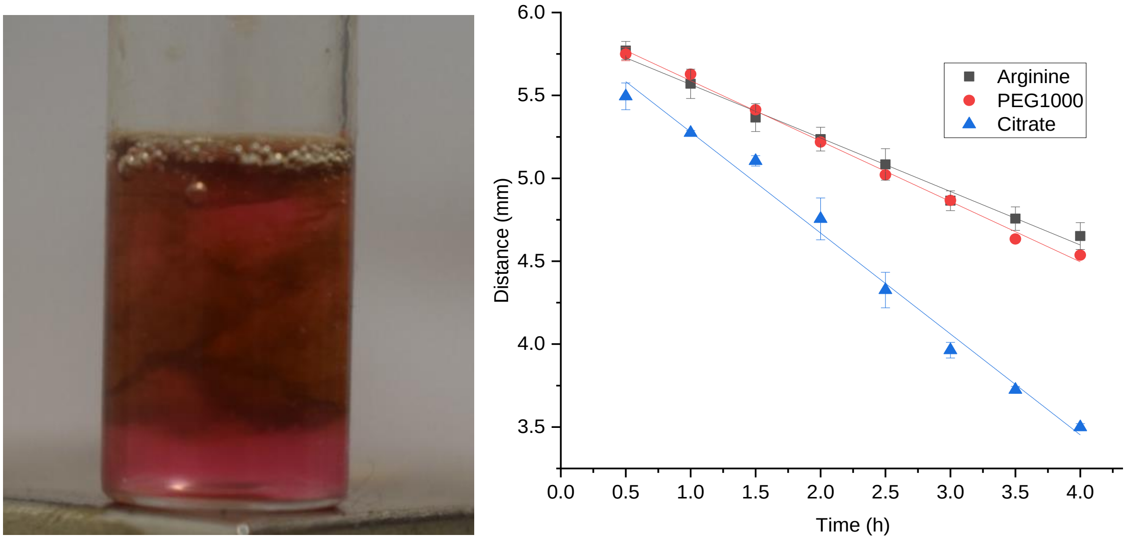

Figure 4.5 Left: Image of cultured ECM in glass vial after 6 h of magnetophoretic transport of 1 mg/ml PEG1000-MNPs (d_{hyd} 24.0 nm (0.16)) under the influence of the N52. **Right:** Magnetophoretic transport of functionalised MNPs (1 mg/ml) through cultured ECM, n=4. $R^2 > 0.98$ in all cases.

From Figure 4.5, v_{exp} values were calculated for PEG1000-, arginine-, and citrate MNPs and are tabulated below (Table 4.3), along with values for agarose/collagen-ISF for comparison purposes. v_{exp} for PEG1000-MNPs in ECM was calculated to be 0.265 ± 0.03 mm/h, which was 17.7% slower than in collagen/agarose-ISF. This was the lowest v_{exp} value measured for PEG1000-MNPs in any matrix. Given that PEG1000MNP should not interact electrostatically with its environment, it is proposed here that the main contribution to this change is a significantly greater $\eta\varphi$ for the ECM medium compared to agarose-collagen. This is reasonable because the presence of multiple fibrous and non-fibrous networks and more complex components that form the ECM compared to the simpler agarose-based media. It may also be possible that during transit, some of the non-fibrillar proteins that are present in the interstitial space (Proteoglycans, albumin, etc.) may have adsorbed onto the surface. The protein corona that could form would lead to an increase in d_{hyd} for the particles. Measurement of the MNPs after magnetophoretic transport by DLS as seen in Chapter 3 (Table 3.4), would confirm if protein adsorption has taken place in the ECM.

Table 4.3 v_{exp} values for ~1 mg/mL PEG1000- (d_{hyd} 24.1 nm), arginine- (d_{hyd} 28.0 nm), and citrate-MNPs (d_{hyd} 12.1 nm), through ECM and agarose/collagen-ISF, n=4.

Surface chemistry	ECM v_{exp} (mm/h)	Agarose/collagen-ISF v_{exp} (mm/h)	v_{exp} change (%)
PEG1000	0.265 ± 0.03	0.322 ± 0.01	-17.7
Arginine	0.222 ± 0.02	0.156 ± 0.02	+29.8
Citrate	0.413 ± 0.02	0.462 ± 0.04	-10.6

v_{exp} for the arginine-MNPs in ECM compared to agarose/collagen-ISF was greater by 29.8%. The increased $\eta\varphi$ effect, it is suggested must be a significant factor influencing any change in v_{exp}. By accounting for the influence of $\eta\varphi$ (-17.7%, based on the PEG1000 data), a net +47.5% change in v_{exp} is calculated for the arginine-MNPs. It is likely that the electrostatic environment in ECM is different to that of the agarose-collagen gels, whereby it is expected that the presence of the negatively charged proteoglycans could be significant. These proteoglycans form the gel network inside the collagen and may be present as free or bound to collagen. The electrostatic attractive interactions between the negatively charged proteoglycans and the positively arginine-MNPs could potentially enhance transport. However further studies are required to confirm this.

Citrate-MNPs experience a 10.6% decrease in v_{exp} in ECM when compared to agarose/collagen-ISF. Again, by subtracting the influence of $\eta\varphi$ (17.7%) from the v_{exp} decrease, a net +7.1% change is calculated for the citrate-MNPs. An increase in v_{exp} on this scale was observed in Chapter 3 for these MNPs for an increase in ionic strength of the aqueous phase of agarose gels. This change in v_{exp} indicates again that the electrostatic interactions are likely influencing transport in a manner consistent with the theory proposed for arginine-MNPs whereby, the negatively charged citrate-MNPs velocity would be expected to be reduced.

4.3.4 Effect of high field gradients on magnetophoresis in agarose gel

Magnetophoretic experiments using the Giamag were carried out to investigate the effect of high magnetic field strength on MNP transport. All experiments up until now have used the N52 (field strength of 0.23 T). In the following experiments, an increased magnetic field strength (1.1 T) was applied using the Giamag to investigate the effect on v_{exp}. PEG1000-, arginine- and citrate-MNPs were magnetically guided through agarose-H_2O, using the Giamag to induce the magnetic field gradient (Figure 4.6). Linear transport behaviour was observed for all MNPs indicating that the magnetic field gradient was constant for the full depth of the gel. The v_{exp} values were 4.691 ± 0.37 mm/h for PEG1000-, 4.734 ± 0.15 mm/h for arginine- and 5.350 ± 0.07 mm/h for citrate-MNPs, all significantly faster than with the N52 (approx. 12.5-times) as would be expected given the increased field strength and gradient.

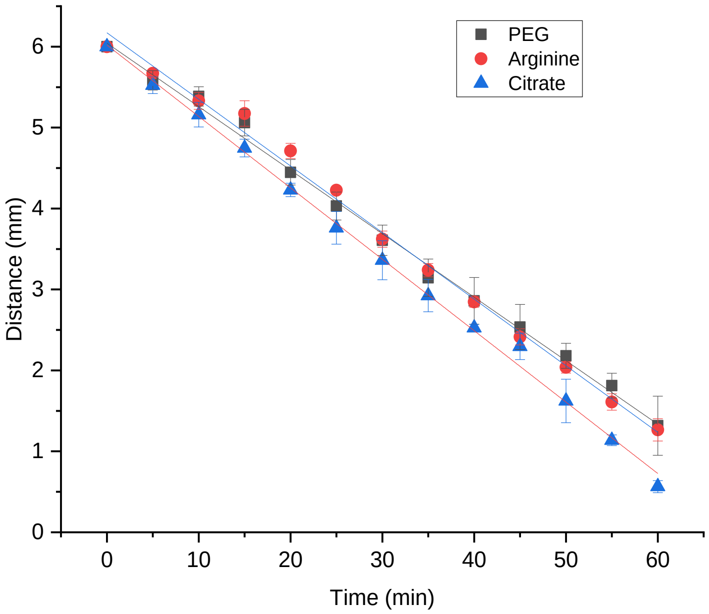

Figure 4.6 Magnetophoretic transport of ~1.0 mg/mL PEG1000-MNPs (d_{hyd} 24.0 nm (0.17)) arginine-MNPs (d_{hyd} 28.0 nm(0.16)), and citrate-MNPs (d_{hyd} 12.0 nm (0.17)) dispersions in DI H_2O through agarose-H_2O (0.3 %w/v, low EEO) in a magnetic field gradient exerted by the Giamag (n=3).

Based on this higher field strength of 1.1 T, the magnetic susceptibility of the MNPs (magnetisation obtained from the data in Figure 2.9) has changed from 0.289 to 0.137. Using this new value for χ, v_{th} values were calculated for these Giamag experiments using equation 3.1. All other parameter values were based on the values used for the N52 experiments (Section 3.3.3). v_{exp} for PEG1000-MNPs (Figure 4.6) was found to be 8.2% slower than v_{th} with the Giamag, this difference would suggest that when using higher magnetic field strengths, the tortuosity that the MNP experiences changes (assuming all other parameters remain constant across the Giamag and N52 experiments). Thus, the φ value calculated based on the PEG1000-MNPs in the N52 experiments (0.040) was re-calculated for the Giamag and found to be 0.031. These different tortuosity values are likely a result of the role the electrostatic interactions play in the different field strengths. Weak electrostatic interactions will repel MNPs from the polymer phase as they travel through the agarose – this is likely the case in weaker magnetic field strengths. In higher magnetic field strengths, it is speculated that this no longer occurs and so the MNPs undergo direct physical contact with the fibres and potential penetration through the pore walls, resulting in a different pathway within pores.

Using this new φ value, %D values were calculated (equation 3.2) to quantify differences between v_{exp} and v_{th} for the MNPs for the N52 and the Giamag (Table 4.4). It can be observed that the %D values calculated for the Giamag were approx. double that observed for the N52 for the charged MNPs, arginine- and citrate-MNPs.

Table 4.4 Magnetophoretic v_{exp} and v_{th} values for PEG1000-, arginine- and citrate-MNPs through agarose-H_2O (0.3% w/v, low EEO) under the influence of the Giamag and N52 magnets. A φ value of 0.031 was used for Giamag calculations, while a value of 0.040 was used for N52 calculations.

	Giamag (φ = 0.031)			N52 (φ = 0.040)		
Surface Chemistry	**v_{exp} (mm/h)**	**v_{th} (mm/h)**	**%D**	**v_{exp} (mm/h)**	**v_{th} (mm/h)**	**%D**
PEG1000	4.691 ± 0.37	4.691	0	0.374 ± 0.02	0.374[	0
Arginine	4.734 ± 0.15	4.071	+16.3	0.352 ± 0.01	0.320	+10
Citrate	5.350 ± 0.07	8.992	-40.5	0.635 ± 0.02	0.750	-18

Based on these observations, a study was undertaken to observe if electrostatic interactions could be used to manipulate magnetophoretic transport as was shown for the N52 in Chapter 3. Experiments were performed with the Giamag whereby the EEO content of the agarose and IS of the aqueous phase of the gel were varied. PEG1000-, arginine-and citrate-MNPs were transported through these media using H_2O and PBS as the aqueous phases respectively, and v_{exp} values calculated (Table 4.5). Interestingly, v_{exp} values were likely not influenced by surface chemistry using the Giamag but their velocities were likely dictated by MNP d_{hyd}. The increase in agarose EEO and IS was shown previously to reduce arginine-MNP v_{exp} and increase citrate-MNP v_{exp}, but neither of these factors impacted on velocities here. Therefore, by increasing the magnetic field strength, the impact of electrostatic interactions is diminished significantly. This preliminary result would indicate that the higher field gradient produced by the Giamag is so great that electrostatic interactions can no longer modulate transport. More comprehensive experiments will need to be undertaken to examine the extent to which the Giamag can override electrostatic interactions. By increasing the bulk viscosity of the agarose to levels that would decrease v_{exp}, it may be possible to indicate a specific velocity at which electrostatics take effect.

Table 4.5 v_{exp} values ~1 mg/mL PEG1000- (d_{hyd} 24.1 nm), arginine- (d_{hyd} 28.0 nm), and citrate-MNPs (d_{hyd} 12.1 nm), through agarose-H_2O (0.3 % w/v low EEO) and agarose-PBS (IS 0.14 M, (0.3% w/v high EEO), n=4.

Surface chemistry	**v_{exp} agarose-H_2O Low EEO (mm/h)**	**v_{exp} agarose-PBS High EEO (mm/h)**
PEG1000	4.691 ± 0.37	4.723 ± 0.02
Arginine	4.736 ± 0.15	4.751 ± 0.02
Citrate	5.351 ± 0.07	5.425 ± 0.06

4.3.5 Effect of high field gradients on magnetophoresis in agarose/collagen

Magnetophoretic experiments using the Giamag were also carried out in the agarose/collagen-ISF medium to investigate the effect of high magnetic field strengths on MNP transport in this network. In previous experiments using the N52, the hydrophobic nature of the surface of these gels was shown to delay MNP penetration into the gel for all surface chemistries. After transferring the MNP dispersion droplet to the top of the same gel in the presence of the Giamag, a similar behaviour was observed for the N52 experiments (Section 4.3.2) whereby all MNPs experienced a delay entering the gel. However, irrespective of surface chemistry in this case, all MNPs penetrated the gel surface after 1 h. However, once the MNPs entered the bulk gel under the influence of the Giamag, the MNP front profile was different from that observed in N52 experiments (Figure 4.7). Here, the MNPs moved through the gel as a narrow-elongated stream of dispersion, likely to minimise interaction of the MNPs with the network. This was unexpected and could be due to MNPs disrupting the self-assembled collagen protein structures due to direct penetration of the polymer network on account of the stronger magnetic field. Disruption of this structure could expose hydrophobic moieties causing the MNPs to take on this different front profile, minimising interactions with the collagen. Clear irreversible damage to the agarose/collagen gels was observed after magnetophoretic transport had taken place (Figure 4.7).

Figure 4.7 Left: PEG1000-MNPs in agarose/collagen-ISF under the influence of the Giamag; t=2 h. **Right:** Damage caused to agarose/collagen-ISF gel taken after MNP transport through the gel.

4.4 Conclusion

This chapter investigated a collagen-based hydrogel and cultured ECM for magnetophoretic transport under low and high field strengths. The agarose/collagen-ISF gels exhibited surface hydrophobic properties, an increased $\eta\varphi$ and enhanced electrostatic interactions (compared to agarose only gels), likely due to the addition of self-assembled collagen. Magnetophoretic transport studies in cultured ECM exhibited no observable surface hydrophobicity effects and v_{exp} values observed were consistent with an increased $\eta\varphi$ (compared to agarose/collagen) and enhanced electrostatic interactions, potentially arising from the fixed and mobile negatively charged proteoglycans present within the gel. The influence of electrostatic forces in ECM agreed with previous studies undertaken in Chapter 3 in agarose.

The effect of a significantly higher magnetic field strength was also investigated in agarose and agarose/collagen gels. It was observed that, in agarose, v_{exp} increased by a factor of 12.5 for all MNPs on account of increased susceptibility and gradient. %D values were found to increase two-fold for the Giamag when compared to the N52. It is theorised that the MNPs will take a different route through the same pathway in the gel, leading to an increased φ in agarose-H_2O gels. Interestingly, electrostatic modulation of magnetophoretic transport, observed previously, was found to be significantly supressed in the presence of the higher field strengths. Magnetophoretic transport behaviour through agarose/collagen-H_2O using the Giamag was observed to be different to that of agarose-H_2O, whereby a linear chain profile of the MNPs during movement could be visualised. This was attributed to the greater magnetic force experienced by the MNPs which resulted in disruption or damage of the assembled collagen fibres. This damage to the gel would result in the exposure of hydrophobic moieties of the collagen. This may induce this very different linear chain profile in order to minimise MNP interactions with the exposed hydrophobic moieties of the collagen.

4.5 References

1. Frantz, C., Stewart, K. M. & Weaver, V. M. The Extracellular Matrix at a Glance. *J. Cell Sci.* **123**, 4195–4200 (2010).
2. Netti, P. A., Berk, D. A., Swartz, M. A., Grodzinsky, A. J. & Jain, R. K. Role of Extracellular Matrix Assembly in Interstitial Transport in Solid Tumors. *Cancer Res.* **60**, 2497–2503 (2000).
3. Wiig, H., Tenstad, O., Iversen, P. O., Kalluri, R. & Bjerkvig, R. Interstitial Fluid: The Overlooked Component of the Tumor Microenvironment? *Fibrog. Tissue Repair* **3**, 12 (2010).
4. Mouw, J. K., Ou, G. & Weaver, V. M. Extracellular Matrix Assembly: A Multiscale Deconstruction. *Nat. Rev. Mol. Cell Biol.* **15**, 771–785 (2014).
5. McKee, T. J., Perlman, G., Morris, M. & Komarova, S. V. Extracellular Matrix Composition of Connective Tissues: A Systematic Review and Meta-Analysis. *Sci. Rep.* **9**, 1–15 (2019).
6. Kular, J. K., Basu, S. & Sharma, R. I. The Extracellular Matrix: Structure, Composition, Age-Related Differences, Tools for Analysis and Applications for Tissue Engineering. *J. Tissue Eng.* **5**, 2041731414557112 (2014).
7. Järveläinen, H., Sainio, A., Koulu, M., Wight, T. N. & Penttinen, R. Extracellular Matrix Molecules: Potential Targets in Pharmacotherapy. *Pharmacol. Rev.* **61**, 198–223 (2009).
8. Cengiz, E. & Tamborlane, W. V. A Tale of Two Compartments: Interstitial Versus Blood Glucose Monitoring. *Diabetes Technol. Ther.* **11**, S-11-S-16 (2009).
9. Heldin, C. H., Rubin, K., Pietras, K. & Ostman, A. High Interstitial Fluid Pressure - An Obstacle in Cancer Therapy. *Nat. Rev. Cancer* **4**, 806–813 (2004).
10. Swartz, M. A. & Fleury, M. E. Interstitial Flow and its Effects in Soft Tissues. *Annu. Rev. Biomed. Eng.* **9**, 229–256 (2007).
11. Wiig, H. & Swartz, M. A. Interstitial Fluid and Lymph Formation and Transport: Physiological Regulation and Roles in Inflammation and Cancer. *Phys. Rev.* **92**, 1005–1060 (2012).
12. Fogh-Andersen, N., Altura, B. M., Altura, B. T. & Siggaard-Andersen, O. Composition of Interstitial Fluid. *Clin. Chem.* **41**, 1522–1525 (1995).
14. Yao, W. J., Li, Y. & Ding, G. Interstitial Fluid Flow: The Mechanical Environment of Cells and Foundation of Meridians. *J. Evidence-Based Complementary Altern. Med.* **1,** 1-9, (2012).
14. Jain, R. K. & Stylianopoulos, T. Delivering Nanomedicine to Solid Tumors. *Nat. Rev. Clin. Oncol.* **7**, 653–664 (2010).
15. Kyburz, K. A. & Anseth, K. S. Synthetic Mimics of the Extracellular Matrix: How Simple is Complex Enough? *Ann. Biomed. Eng.* **43**, 489–500 (2015).
16. Williams, C. *et al.* Cardiac Extracellular Matrix-Fibrin Hybrid Scaffolds with Tunable Properties for Cardiovascular Tissue Engineering. *Acta Biomater* **14**, 84–95 (2015).
17. Wade, R. J. & Burdick, J. A. Engineering ECM signals into Biomaterials. *Materials Today* **15**, 454–459 (2012).

18. Ma, P. X. Biomimetic materials for Tissue Engineering. *Adv. Drug Deliv. Rev.* **60**, 184–198 (2008).
19. Shin, H., Jo, S. & Mikos, A. G. Biomimetic Materials for Tissue Engineering. *Biomaterials* **24**, 4353–4364 (2003).
20. Fernández-Pérez, J., Kador, K. E., Lynch, A. P. & Ahearne, M. Characterization of Extracellular Matrix Modified Poly(ε-caprolactone) Electrospun Scaffolds with Differing Fiber Orientations for Corneal Stroma Regeneration. *Mater. Sci. Eng.: C* **108**, 110415 (2020).
21. Han, D. & Gouma, P.-I. Electrospun Bioscaffolds That Mimic the Topology of Extracellular Matrix. *Nanomedicine* **2**, 37–41 (2006).
22. Jun, I., Han, H.-S., Edwards, J. R. & Jeon, H. Electrospun Fibrous Scaffolds for Tissue Engineering: Viewpoints on Architecture and Fabrication. *Int. J. Mol. Sci.* **19**, (2018).
23. Lei, B. *et al.* Nanofibrous Gelatin–Silica Hybrid Scaffolds Mimicking the Native Extracellular Matrix (ECM) Using Thermally Induced Phase Separation. *J. Mater. Chem.* **22**, 14133–14140 (2012).
24. Papavasiliou, G., Sokic, S. & Turturro, M. Synthetic PEG Hydrogels as Extracellular Matrix Mimics for Tissue Engineering Applications. *Biotechnology - Molecular Studies and Novel Applications for Improved Quality of Human Life* (2012).
25. Patel, D., Menon, R. & Taite, L. J. Self-Assembly of Elastin-Based Peptides into the ECM: The Importance of Integrins and the Elastin Binding Protein in Elastic Fiber Assembly. *Biomacromolecules* **12**, 432–440 (2011).
26. Whitesides, G. M. & Grzybowski, B. Self-Assembly at All Scales. *Science* **295**, 2418–2421 (2002).
27. Deshmukh, S. N., Dive, A. M., Moharil, R. & Munde, P. Enigmatic Insight into Collagen. *J. Oral. Maxillofac. Pathol.* **20**, 276–283 (2016).
28. Gordon, M. K. & Hahn, R. A. Collagens. *Cell Tissue Res.* **339**, 247–257 (2010).
29. Ulrich, T. A., Jain, A., Tanner, K., MacKay, J. L. & Kumar, S. Probing Cellular Mechanobiology in Three-Dimensional Culture with Collagen-Agarose Matrices. *Biomaterials* **31**, 1875–1884 (2010).
30. Lake, S. P., Hald, E. S. & Barocas, V. H. Collagen-Agarose Co-Gels as a Model for Collagen-Matrix Interaction in Soft Tissues Subjected to Indentation. *J. Biomed. Mater. Res. A.* **99**, 507–515 (2011).
31. Kuhn, S. J., Hallahan, D. E. & Giorgio, T. D. Characterization of Superparamagnetic Nanoparticle Interactions with Extracellular Matrix in an In Vitro System. *Ann. Biomed. Eng.* **34**, 51–58 (2006).
32. Hansen, U. *et al.* WARP Interacts with Collagen VI-Containing Microfibrils in the Pericellular Matrix of Human Chondrocytes. *PLOS ONE* **7**, (2012).
33. Kulkarni, S. *et al.* Quantifying the Motion of Magnetic Particles in Excised Tissue: Effect of Particle Properties and Applied Magnetic Field. *J. Magn. Magn. Mater* **393**, 243–252 (2015).

34. Holligan, D. L., Gillies, G. T. & Dailey, J. P. Magnetic Guidance of Ferrofluidic Nanoparticles in an In Vitro Model of Intraocular Retinal Repair. *Nanotechnology* **14**, 661 (2003).
35. Ushiki, T. Collagen Fibers, Reticular Fibers and Elastic Fibers. A Comprehensive Understanding from a Morphological Viewpoint. *Arch. Histol. Cytol.* **65**, 109–126 (2002).
36. Ushiki, T. The Three-Dimensional Ultrastructure of the Collagen Fibers, Reticular Fibers and Elastic Fibers: A Review. *J. Anat.* **67**, 186–199 (1992).
37. Jansen, K. A. *et al.* The Role of Network Architecture in Collagen Mechanics. *Biophys. J.* **114**, 2665–2678 (2018).
38. Stylianopoulos, T. *et al.* Diffusion of Particles in the Extracellular Matrix: The Effect of Repulsive Electrostatic Interactions. *Biophys. J.* **99**, 1342–1349 (2010).
39. Ramanujan, S. *et al.* Diffusion and Convection in Collagen Gels: Implications for Transport in the Tumor Interstitium. *Biophys. J.* **83**, 1650–1660 (2002).
40. Mesquida, P. *et al.* Evaluation of Surface Charge Shift of Collagen Fibrils Exposed to Glutaraldehyde. *Sci. Rep.* **8**, 1–7 (2018).
41. Wang, D., Ye, J., Hudson, S. D., Scott, K. C. K. & Lin-Gibson, S. Effects of Nanoparticle Size and Charge on Interactions with Self-Assembled Collagen. *J. Colloid Interface Sci.* **417**, 244–249 (2014).
42. Iozzo, R. V. & Schaefer, L. Proteoglycan Form and Function: A Comprehensive Nomenclature of Proteoglycans. *Matrix Biol.* **42**, 11–55 (2015).

Chapter 5

Biomarker capture from hydrated polymer networks and cultured extracellular matrix

5.1 Introduction

During earlier chapters, magnetophoretic transport of MNPs has been explored in polymer networks and biological mimics to aid in the understanding of MNP motion in soft tissue. This research serves as a foundation for future in-vivo applications of MNPs as a vehicle for drug delivery, a platform for sensing or for the targeting of biomarkers in tissue.

Magnetic capture methods have already been applied for targeting biomarkers in biological media and has been discussed in detail in Chapter 1. One such study[1] synthesised functionalised MNPs designed to target key biomarkers of osteoarthritis (OA) in a synovial fluid model. This model consisted of bovine serum mixed with hyaluronic acid to mimic the chemical and physical composition of rat synovial fluid. Iron oxide MNPs were conjugated to antibodies to target specific antigens in the synthetic synovial fluid. The MNPs were incubated in the synovial fluid for a period of time until equilibrium binding was reached for 40 min. A magnetic probe (1 x 1 mm N50 Neodymium, no field strength stated) was used to extract the MNPs from the synovial fluid. The MNP-bound antigens were detached from the MNP by heat (85°C) and quantified by an enzyme linked immunosorbent assay (ELISA). Building on this study, a subsequent paper was published by the same group a year later where the method was applied to an in-vivo study[2]. Antibody-functionalised MNPs were injected into the synovial fluid of rats immediately after euthanasia and the binding and extraction of a specific antigen biomarker was demonstrated. This new magnetic capture method was compared with the established lavage method to determine biomarker concentration in a knee joint of a rat post-mortem. Although no limit of detection was reported, the MNPs were able to target biomarkers for subsequent quantification in pg/ml concentrations. It was found that the magnetic capture method was able to capture ~twice the number of antigen biomarkers as the lavage method.

Affinity-based binding can be achieved using antibodies as described above, but also with other biological molecules such as DNA and aptamers and chemical reagents such as cyclodextrins, boronic acids (BA) etc[3]. BA for example can undergo affinity binding with specific molecules such as sugars. BA is a Lewis acid and has a ~pKa=9. The pKa value is a measure of the strength of an acid (pKa is the negative log of the acid dissociation constant (Ka)). At a pH=pKa of BA, 50% of the acidic boronate groups are dissociated and ionised. At pHs below this pKa, BA will become increasingly protonated and at pHs above this pKa, BA will become increasingly deprotonated and hence ionised.

Lewis acidic BA reversibly binds to *cis*-1,2-diol or cis-1,3-diol substituents of molecules such as saccharides glucose, fructose or galactose via the formation of cyclic boronate esters (Figure 5.1) as mentioned earlier[4,5]. Under optimal pH conditions, typically between the pKa of the BA (~9) and the boronate ester (~6)[6], the introduction of sugar will lead to strong binding. The formation of the boronate ester upon binding of cis-diols will lead to an overall increase in acidity, i.e., decrease in pKa.

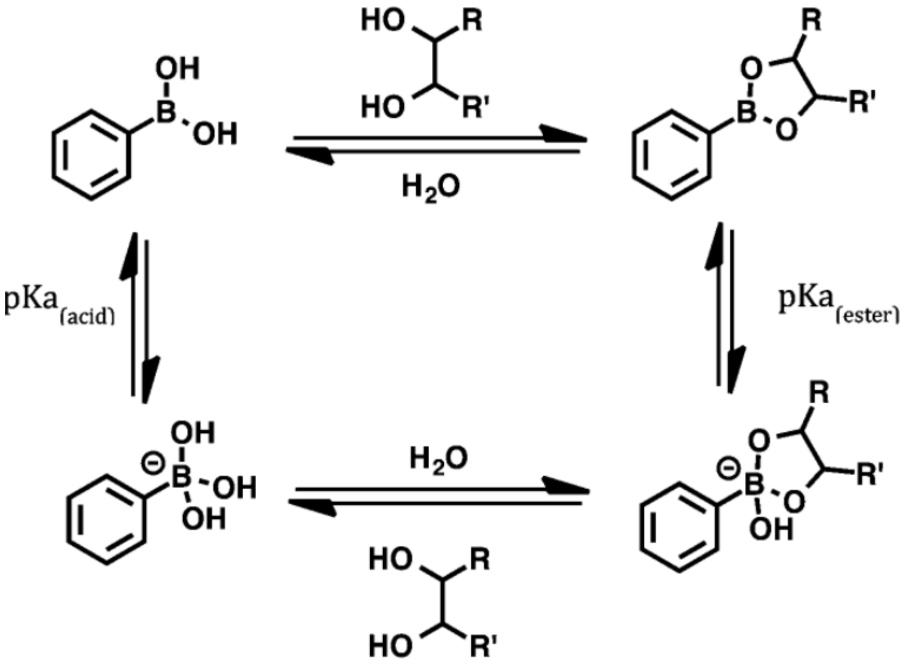

Figure 5.1 The relationships between phenylBAs and diol esters[7].

Reversible covalent interactions of BAs with cis-1,2- or 1,3-diols to form five- or six-membered cyclic esters, respectively, have proved efficient. The strength of the binding to saccharides is determined by the orientation and relative position of the hydroxyl groups[8–10]. The formation of the boronate ester results in an increase in acidity, i.e. a decrease in pKa, meaning the ester formation, and hence diol binding can be easily monitored. This has led to increasing interest in their use as saccharide sensors and drug delivery systems[11–14]. BA-MNPs have been used to capture many classes of molecules, including sugars[15,16], antibodies[17,18] and catecholamines[19,20] for applications in capture, extraction or enrichment.

In order to functionalise MNPs with BA functional groups to target biomarkers such as glucose, careful consideration of the functionalisation approach is needed. BA will not bind to metal ions strongly and so ligand modification is often used to attach BA. Aminosilanes can be used to attach BA functional groups to iron oxide cores[21], whereby surface silanization is used to provide strong silanol bonds. These aminosilanes can be modified to covalently bind the BA via epoxy-amine chemistry. Another approach is the use of silica oxide to functionalise the MNP to provide stability and allow further modification with an incoming BA ligand. Xue et al.[22] for example used a silica oxide (APTES) and covalently modified it with 4-formylphenylBA.

In order to bind a target molecule, BA-MNPs are typically incubated in media containing target until equilibrium binding is reached. One example[21] used BA-functionalised MNPs for the quantification of dopamine (DA). MNPs were used to extract DA from tris-HCl buffer (pH 8.5) for 60 min and subsequently magnetically extracted (no magnet specifications are given). DA has an affinity for BA ($K=448\ M^{-1}$)[23]. DA levels in solution before and after exposure to MNPs were quantified by measuring the change in fluorescent intensity arising from polydopamine. This fluorescence originated from the self-polymerisation of the DA under the alkaline conditions used. The maximal adsorption capacity of the BA-MNPs was 108.46 µg/g at pH 8.5 demonstrating the suitability of BA-MNPs for extracting compounds containing diols available for binding due to formation of boronate esters.

Various quantification methods have been used to measure target binding to boronic acids and includes fluorescence[24], surface plasmon resonance[25] and colourimetric sensing arrays[26]. Traditional colourimetric enzyme assays can be used to quantify enzymatic substrates such as glucose due to high sensitivity and specificity[27]. Glucose oxidase is often used as the enzyme to catalyse the oxidation of glucose for subsequent UV analysis[28] to allow for rapid quantification. Glucose oxidase catalyses glucose to yield gluconic acid and hydrogen peroxide (H_2O_2). The H_2O_2 that is produced is reacted with *o*-dianisidine in the presence of a peroxidase enzyme to form a pink coloured product (oxidised *o*-dianisidine). The concentration of glucose present is proportional to the amount of coloured product produced and is quantified using Beer's Law.

In this work, a non-invasive method has been proposed to magnetically capture glucose from biological tissue mimics using BA-MNPs. GLYMO-MNPs were functionalised via the base-catalysed epoxide ring opening reaction using 3-

aminophenylBA. The BA-MNP ζ_p was shown to vary with solution pH, which, it is demonstrated here, is dependent on the ionisation state of the BA. Upon incubation with glucose, changes in BA-MNP ζ_p and size were observed, attributed to glucose binding. At specified pHs, the ζ_p of the BA-MNPs was shown to decrease in magnitude upon glucose binding, likely due to an increase in acidity due to the formation of boronate esters. Linear magnetophoretic velocities were measured for the MNPs in agarose in the absence and presence of glucose and the presence of glucose was shown to reduce MNP velocity. Finally, an investigation into the capture efficiency of the BA-MNPs of glucose from solution, agarose polymer networks and cultured ECM was assessed. This work is an initial proof of concept to demonstrate that magnetically guided BA-MNPs could be a potential viable candidate for minimally-invasive biomarker capture from tissue in the future.

5.2 Materials & methods

5.2.1 Materials

D-(+)-glucose (50-99-7), iron (III) acetylacetonate (14024-18-1), benzyl alcohol (100-51-6), GLYMO (2530-83-8), THF (109-99-9), 3-aminophenylboronic acid (30418-59-8), calcium chloride (10043-52-4), HEPES (7365-45-9), potassium chloride (7440-09-7), magnesium sulphate (7487-88-9), sodium chloride (7440-23-5), hydrochloric acid (HCL) (7647-01-0) monosodium phosphate (53408-95-0) and saccharose (57-50-1) were purchased from Sigma. Chloroform (67-66-3) was purchased from Fisher Chemical (Geel, Belgium). Glucose (Hexokinase) assay kit (GAGO-20) was purchased from Sigma.

5.2.2 Instrumentation

See Section 2.2.2 for details of all instrumentation used.

5.2.3 MNP synthesis

The MNP cores were synthesised via the microwave digestion protocol as described in Section 2.2.3.3.

5.2.4 Boronic acid–MNP functionalisation

BA-MNPs were functionalised as per Section 2.2.4.4. Briefly, an initial ligand exchange with GLYMO formed the silanol bonds on the MNP surface. The epoxy ring was then opened via base hydrolysis, using 3-aminophenylBA to yield BA-MNPs. The chemical functionalisation of the MNP is shown below (Figure 5.2).

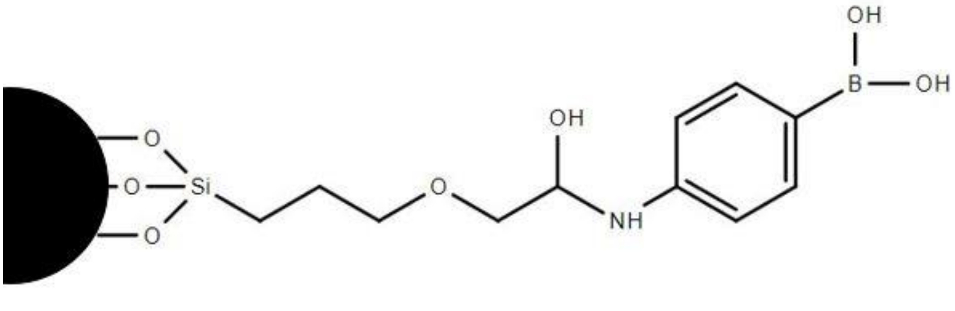

Figure 5.2 Chemical structure of BA functionalisation group whereby the BA group is in trigonal form.

5.2.5 Boronic acid–MNP characterisation

Synthesised BA-MNPs were characterised by DLS to determine their d_{hyd} and surface charge. FTIR was then performed to confirm that surface functionalisation had taken place successfully.

5.2.6 Media preparation

Agarose-H_2O gels (Section 2.2.5); agarose-interstitial fluid (ISF) gels (Section 4.2.4.1); cultured ECM (Section 4.2.4.3) were prepared as described previously except that plastic cuvettes were used in lieu of glass vials. The plastic cuvette was modified for MNP extraction by carefully cutting the base of the cuvette off. A square of masking tape was placed on the bottom of the hollow cuvette to prevent the agarose solution from leaking while it solidified. After solidifying overnight at 4 °C, gels were placed tape edge facing down onto one of the four corners of the N52 magnet. The tape was removed 1 h after full transit through the media had taken place. A magnetic tip (1 x 1 x 2 mm, Neodymium N40 magnet) was used to extract MNPs from the bottom of the gel. The magnet was washed vigorously with water to detach MNPs for subsequent quantification, once dispersed in deionised water (DI H_2O).

5.2.7 Extraction and quantification of glucose from buffer solution

BA-MNPs (200 µL) in DI H_2O (2 mg/mL) were transferred to a 7 mL glass vial. Glucose (2 mL) in DI H_2O was transferred into the same glass vial and the mixture agitated via plate-shaker for 90 min. NaCl (500 µL, 2 M) was then added and vortexed for 1 min to precipitate the MNPs from solution. The mixture was placed on a corner of the N52 magnet for 1 min to allow for magnetic separation of the BA-MNPs from bulk solution. The solution was removed and the MNP material was washed with DI H_2O 3 times to remove unbound glucose. The bound glucose was then quantified enzymatically. Briefly, the assay reagent (250 µL) containing hexokinase was added to the MNPs and incubated for 30 min. The vial was then placed on top of the magnet to precipitate out the glucose-bound MNPs, the absorbance of this solution was measured at 340 nm.

Standard glucose solutions were prepared in the range of 5-50 ppm and were quantified enzymatically in the same way as described above for the preparation of the calibration curve. All analysis was carried out in triplicate.

5.2.8 Extraction and quantification of glucose from agarose gels

BA-MNPs (200 µL) in DI H_2O (2 mg/mL) were transferred to the top of an agarose-H_2O or agarose-ISF gels containing known concentrations of glucose as specified. The cuvettes were placed on a corner of the magnet and capped to prevent dehydration and left overnight. Once the MNPs migrated through the full depth of the gels, the base of the cuvette was removed and a small magnet was used to collect the BA-MNPs for transfer into a glass vial. The BA-MNPs were washed 3 times with DI H_2O to remove unbound glucose. Glucose quantification was performed as described in Section 5.2.7.

5.3 Results & Discussion

5.3.1 Characterisation of BA-MNPs

BA-MNPs were first characterised in PBS (pH 7.4) by DLS (Figure 5.3). ζ_p of the BA-MNPs was measured to be -21 ± 0.2 mV, indicating stable, negatively charged particles which agrees with literature[29]. The PDI value of 0.18 is representative of a monodisperse population. The pKa of free aminophenylBA is in the region of 8.8[7,30] and therefore the pKa of the MNP-bound aminophenylBA is likely to be in this region also, where the effect the surface attachment chemistry may have some small effect on the BA pKa. Nevertheless, it is reasonable to hypothesise that at a pH of 7.4, the immobilised BA may be partially ionised and so the negative surface charge observed here could therefore be attributed to this. There may also be a contribution from residual hydroxyl groups from the functionalisation process. It is also important to note that there is a basic ionisable amine group attached to the phenyl ring; however, this would not be expected to be charged at neutral pH.

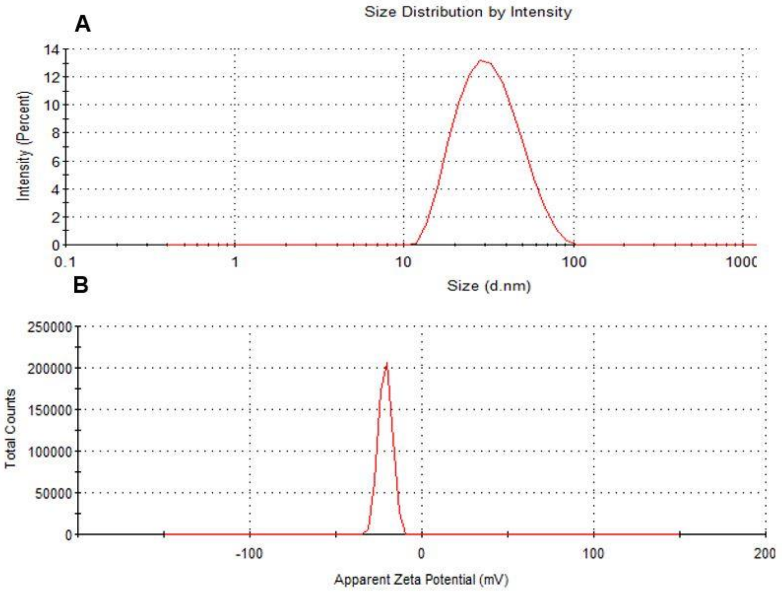

d_{hyd}:	**29.5 ± 0.5**
PDI	**0.18 ± 0.01**
ζ_p	**-21 ± 0.2**

Figure 5.3 A) Size distribution profile of BA-MNPs measured (PDI 0.18) and **B)** ζ_p profile of BA-MNPs in PBS pH 7.4 (0.1 M).

FTIR was used to verify the attachment of 3-aminophenylBA to the MNPs had taken place (Figure 5.4). This confirmed the covalent linkage between the BA and GLYMO precursor attached to the MNPs after the opening of the epoxy ring. Bands at 3212 and 2932 cm^{-1} are indicative of C-H stretches in an aromatic ring, the band at 1600 cm^{-1} indicate N-H bonds, when combined with the absence of bands at 1200, 950 and 800 cm^{-1}, show that the epoxy ring of the GLYMO opened and 3-aminophenylBA successfully attached via covalent bonds. Bands at 1452 cm^{-1} show the Si-O bond that indicate binding between the iron and the aminosilane of the GLYMO. The phenyl ring can be seen in the region of 1300-1500 cm^{-1}, the band at 1650 cm^{-1} shows a C=C stretch that is also present on the ring.

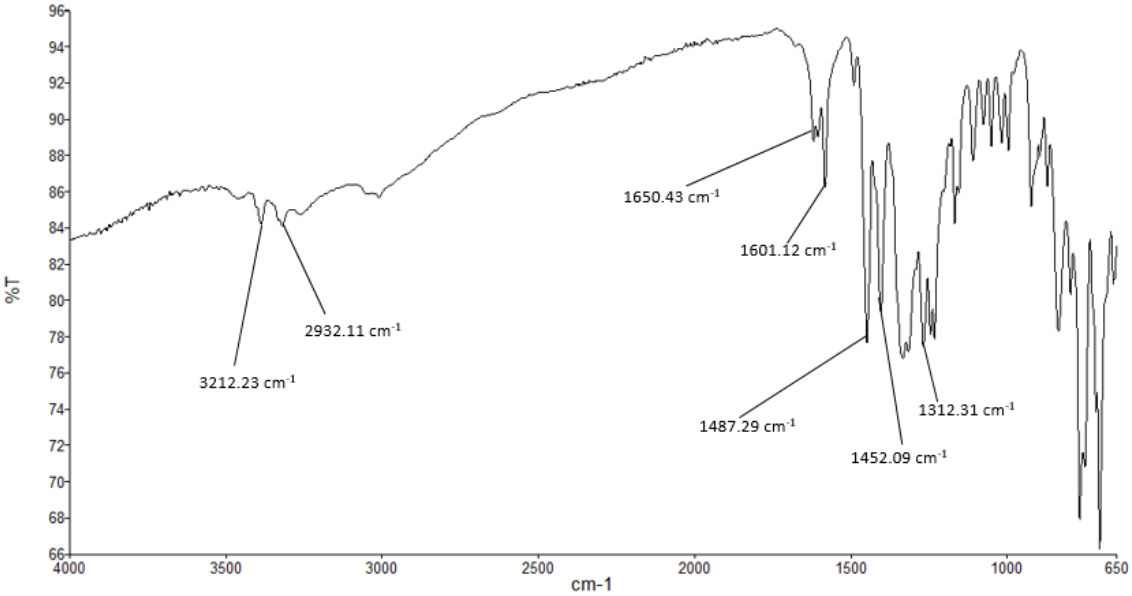

Figure 5.4 FTIR performed on BA-MNPs to confirm functionalisation.

5.3.2 Characterisation of BA-MNPs as a function of pH

The ionisation state of the BA will be dependent on pH (Figure 5.1). The ionised tetrahedral form, which will dominate at higher pHs will carry a negative charge due to the deprotonated BA. This negative charge will increase the electrostatic stability of the BA-MNPs. To investigate the effect of pH on the colloidal stability and ionisation state, BA-MNPs were dispersed in mixed solutions of HCL (0.1 M) and NaOH (0.1 M) in the pH range 6-12. The effect of pH was monitored in relation to changes to d_{hyd} (Figure 5.5 A), PDI (Figure 5.5 A) and ζ_p (Figure 5.5 B).

In Figure 5.5 A, d_{hyd} shows small diameter increases across the pH range 6-9, with d_{hyd} increasing from ~29 to 32 nm. This increase observed in d_{hyd} is not due to agglomeration effects as PDI values of <0.2 across this range suggests a monodisperse MNP population. The change in d_{hyd} maybe due to changes in the EDL of the BA-MNP over this pH range and is consistent with the increase in magnitude of the negative ζ_p observed as described below. Below ~pH 5, MNP d_{hyd} was highly variable and had corresponding high PDI values (data not shown). This behaviour was likely on account of destabilisation due to iron oxide dissolution that takes place in acidic conditions[31] leading to possible aggregation. The d_{hyd} of the BA-MNPs increased sharply above ~pH 10 and was mirrored by a sharp increase in PDI. The formation of aggregates may be responsible for this increase in PDI. The high ζ_P would indicate presumed stability that should prevent aggregation formation. The high pH may cause a change in the surface chemistry of the MNPs that is not yet known. This remains to be verified with further experimentation. Despite this, the effect is clear that above pH 10, the BA-MNPs consistently aggregate and precipitate out of solution. Thus, it is evident from these experiments, that strongly basic or acidic conditions cause aggregation and/or irreversible damage to the iron oxide core.

In Figure 5.5 B, several distinct values for ζ_p were observed across the pH range. From pH 6 to 9, a steady increase in ζ_p for the BA-MNPs was observed, going from weakly stable (-15 mV) at pH 6 to strongly stable (-30 mV) at pH 9. This increase in magnitude of the negative surface charge and hence stability may be due to a decrease in ionisation of the secondary amine present and/or partial ionisation of the BA. It is also possible that there are additional effects playing a role on the functionalisation that have yet to be elucidated.

At ~pH 9, the increasingly negative trend in ζ_p was disrupted and a sharp decrease in ζ_p was observed. This sharp decrease (-31 to -15 mV over pH range 9.0-9.6) is attributed to the ionisation of the BA which is likely becoming dominant in relation to dictating the overall surface charge at this point. This dramatic effect was also observed in a pH study of previously synthesised BA-MNPs[33] (decreasing from -23 mV at pH 7.4 to -14 mV over the pH range 9-10).

At ~pH 9.6, a sharp increase in magnitude of the negative ζ_p was observed, which plateaus at ~pH 11. This negative ζ_p increase is attributed here to an increasing ionisation of the BA, expected at pHs above the pKa of the BA, on account of the conversion of the neutral trigonal form of BA to its ionised, tetrahedral form. From this data, it is reasonable to assume that from ~pH 9, the charge on the BA dominates the overall surface charge of the BA-MNP. From pH 9.6 upward, the data is seen to be sigmoidal in nature, likely representing a portion of a classical pH response curve for BA above its pKa. At a ~pH 11, ζ_p plateaus to reach a constant negative value (-60 mV) likely due to the full conversion of the neutral BA to its ionised form.

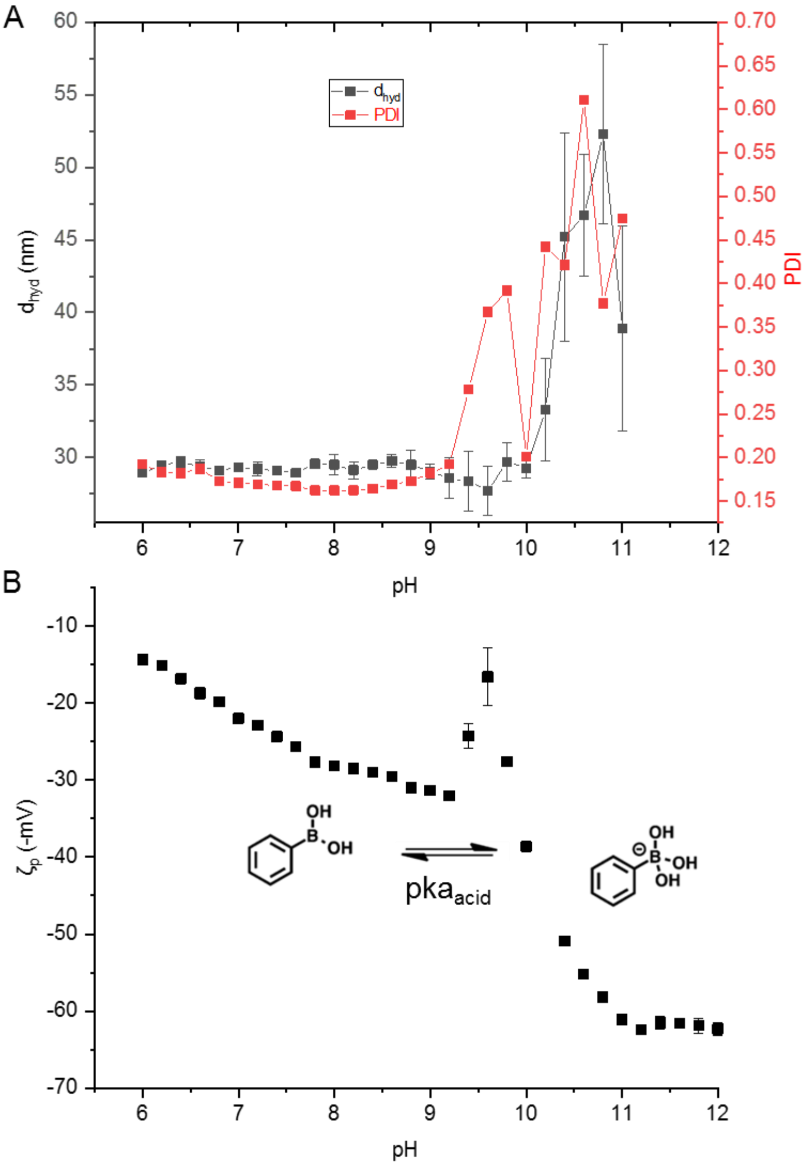

Figure 5.5 A) d_{hyd} and corresponding PDI values for BA-MNPs plotted as a function of pH 6-12, ionic strength 0.1 M. **B)** ζ_p of BA-MNPs (~1.0 mg/mL, PDI 0.18) as a function of pH 6-12 (n=4), ionic strength 0.1 M. Images of the BA functional groups in different ionisation state dependent on the pH are inset where appropriate.

In Figure 5.5 B, the point at which the direction of change of ζ_p reversed (pH 9.6) is hypothesised here to be as a result of the ionisation state of the BA becoming significant and beginning to dominate the surface charge of the MNP. This point (9.6 in this case) is taken here as a relative measure of pKa, and referred to herein as the experimental pKa (pKa_{exp}). Above this pH, the data is sigmoidal in nature, representing a theoretical pH response curve. From theory, it would be expected that the inflection point of this sigmoidal curve would represent the pKa of the BA. In our case, we are using pKa_{exp} as an estimate of this inflection point. In Figure 5.5 B, pKa_{exp} was taken as 9.6, close to the actual pKa of the free aminophenylBA (~8.8)[7]. The attachment of the aminophenylBA to the GLMO-MNP may cause the pKa of the BA to shift upwards and this shift has been reported to reach 9.2[33] previously. This study demonstrates that ζ_p can be used to track the surface charge of the BA-MNPs as a function of pH, where it is proposed that the surface charge measured correlates with the ionisation state of the BA at pHs>~9. At physiological pH 7.4, the BA-MNPs are demonstrated to be stable and slightly negatively charged, making them a viable targeting system for glucose in tissue.

5.3.3 Effect of glucose binding on BA-MNP properties as a function of pH

In the presence of glucose, BA binds to glucose and converts to a boronate ester (Figure 5.1) resulting in an increase in acidity and a decrease in pKa. In this section, d_{hyd} and ζ_p of the BA-MNPs are measured in the presence of glucose to understand the effect of glucose binding on these parameters. The d_{hyd} and ζ_p of the BA-MNPs were measured by DLS before and after incubation with glucose (1 min incubation time) across a pH range 6-12 (Figure 5.6). In Figure 5.6 A, d_{hyd} increased by ~2-3 nm in the presence of glucose and was consistent across the pH range 6-10. (Above pH 10 the BA-MNPs aggregate and precipitate out of solution). Free glucose molecules were measured here to have a d_{hyd} of 1.1 nm (data not shown), and it is therefore realistic that d_{hyd} of the BA-MNPs would increase by 2-3 nm upon glucose binding. This data supports that no aggregation is taking place in the presence of glucose and that the MNP hydrodynamic size increase observed was due to the onset of BA binding of glucose.

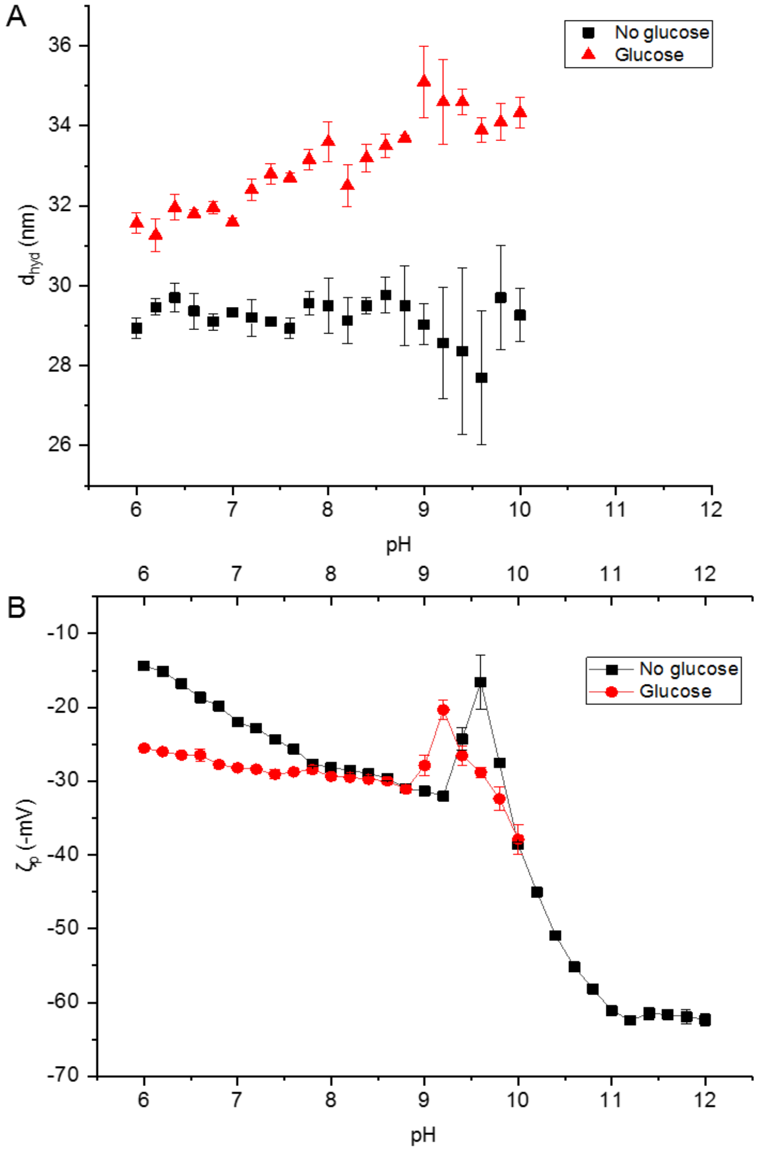

Figure 5.6 A) d_{hyd} measurements for MNP suspensions (1.0 mg/mL), in the presence and absence of glucose (20 ppm) as a function of pH (n=4). **B)** ζ_p of BA-MNPs (~1.0 mg/mL, PDI 0.18) in the presence and absence of glucose (20 ppm) as a function of pH (n=4). Incubation time for all experiments was 1 min.

In Figure 5.6 B, it can be observed that the measured ζ_p value at pH ~6 in the presence of glucose was -26 mV, ~10 mV less than when no glucose was present. This increase in negative surface charge is likely due to the bound glucose which as a free species has a ζ_p of -11.1 mV in PBS (data not shown). Interestingly, the onset of a decreasing trend in ζ_p observed previously in the absence of glucose was also observed in the presence of glucose. However, the pKa_{exp} shifted negatively to pH 9.2 (from pH 9.6 without glucose). This shift is attributed to binding of glucose to the BA-MNPs which leads to the formation of the more acidic boronate ester and hence lowering the pKa. This is consistent with theory explained earlier, whereby the formation of the boronate ester upon cis-diol binding is well-known to increase the acidity of the BA, and leads to a shift in pKa. The consistent changes in both d_{hyd} and ζ_p qualitatively support the uptake of glucose by the BA-MNPs from aqueous solution after incubation.

5.3.4 Effect of incubation time and binding affinity on pKa_{exp}

The incubation time is an important factor to consider in any process that involves affinity binding interactions whereby binding will progress as a function of time until an equilibrium state is reached between free and bound species. This incubation time required to reach equilibrium will depend the affinity binding constant of the target molecule (glucose in this instance) to BA but also other characteristics of the incubation medium (viscosity, IS, temp, etc.). In this study, the effect of incubation time on glucose uptake by BA-MNPs was investigated in relation to pKa_{exp}. As incubation time is increased, (until equilibrium is reached), it would be expected that increasing amounts of boronate esters would form, increasing the acidity of the BA and therefore result in negative pKa shifts of the BA. Once equilibrium binding is reached, no further change in pKa_{exp} would be expected.

For these experiments, BA-MNPs were incubated in glucose solutions (20 ppm) for time periods 1-240 min. For each incubation time, a range of glucose solutions were prepared in the pH range 6-10 (0.2 pH increments) and the ζ_p measured. The ζ_p was then plotted as a function of pH for each incubation time (Figure 5.7 A). From this data, the pKa_{exp} was taken as the point of directional change of the ζ_p as described earlier. It can be seen that increasing the incubation time results in an earlier onset of this directional change in ζ_p (i.e. a decreasing pKa_{exp}) for incubation times up to 90 min. After 90 min incubation time, no further change in the pKa_{exp} was observed indicating that at ~90 min, equilibrium binding between the BA-MNPs bound and the free glucose was reached (Figure 5.7 B). This is supported by a finding from Ni et al.[34], which shows that initial binding of boronates to sugars proceeds quickly (<1 min) but can take up to ~80 min to reach equilibrium depending on sugar concentration and type of BA[34].

Interestingly, the electrostatic stability of the BA-MNP population was also observed to increase upon glucose binding whereby the magnitude of the ζ_p minimum was taken as a measure of this stability. It was measured to be -16 mV prior to glucose binding and decreased to -20 mV after ~30 min glucose incubation times and longer.

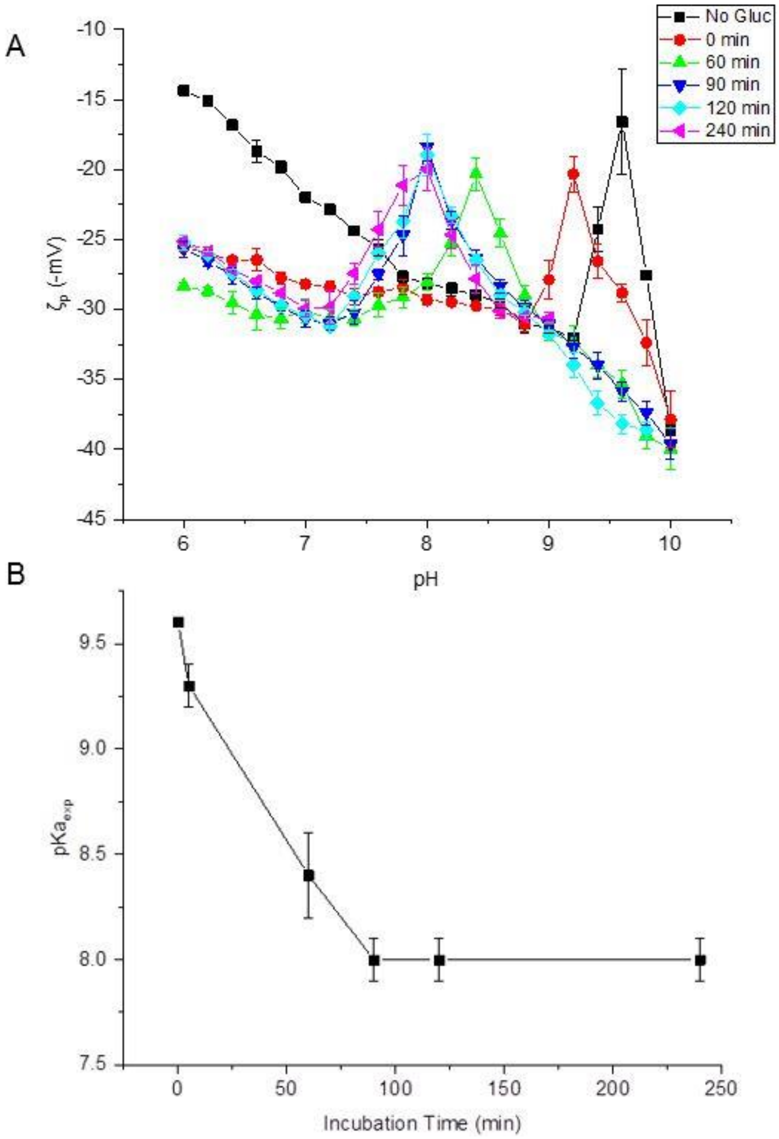

Figure 5.7 A) ζ_p values for dispersions of BA-MNPs before and after incubation with glucose (20 ppm) for periods of time over the pH range 6-10 (sampling at 0.2 pH intervals). **B)** pKa$_{exp}$ values (estimated from data in A) plotted as a function of glucose incubation time.

In order to investigate the effect of sugar type on pKa changes over time, fructose and galactose were incubated separately with BA-MNPs for different incubation times across a pH range and compared to glucose. These sugars have different binding affinities for BA (glucose: 110 M^{-1} [8,35]; galactose: 370 M^{-1} [36]; fructose: 4370 M^{-1} [7]). Studies were performed in a similar fashion to Figure 5.7 A, where individual ζ_p measurements were taken at 0.2 pH increments in the pH range 6-10 at each incubation time. pKa$_{exp}$ values were extracted as already described (data not shown). and plotted as a function of incubation time for each sugar (Figure 5.8).

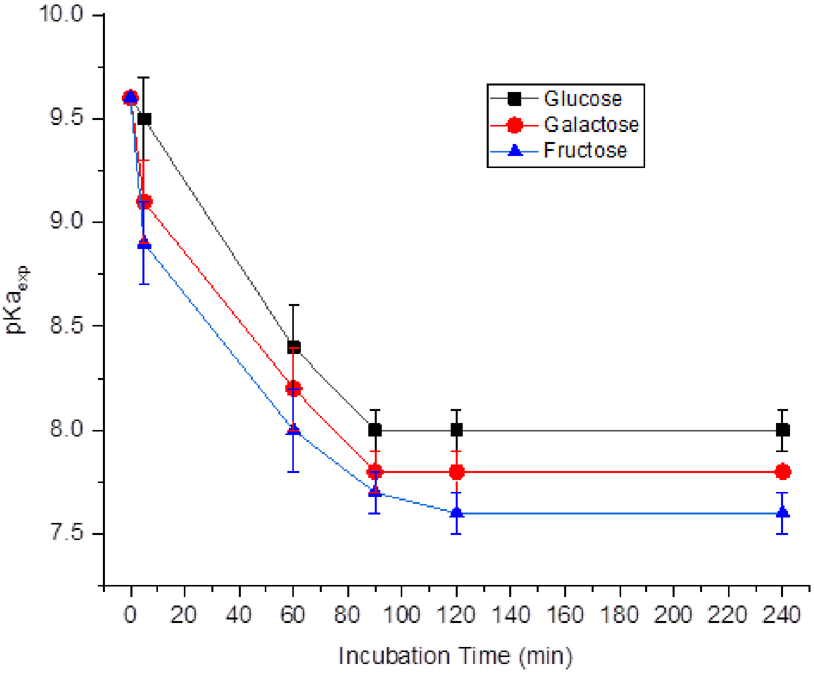

Figure 5.8 Extracted pKa$_{exp}$ values for BA-MNPs incubated with different sugars plotted as a function of time (n=4).

After an incubation time of 1 min, the pKa$_{exp}$ values shifted negatively for all three sugars as expected. The magnitude of these shifts correlated with binding strength where glucose has the lowest pKa (and smallest shift in pKa$_{exp}$) and fructose the highest pKa (and greatest shift in pKa$_{exp}$). At 90 min, both glucose and galactose have reached equilibrium, however fructose has not. By 120 min, fructose has reached equilibrium as the extracted pKa$_{exp}$ does not shift further after this timepoint. Glucose binding exhibited the smallest shift in pKa$_{exp}$ to 8.1, galactose pKa$_{exp}$ shifted to 7.8 and fructose exhibited the largest shift in pKa$_{exp}$ to 7.6. The theoretical pKa for a fructose-binding to BA is 4.7[37] and for a galactose-bound boronate ester is 6.3[7]. This significant difference in pKa values, show the limitation of using the point of ζ_p disruption as the pKa. It may also be plausible that some other factor besides time is acting as a limiting factor in the shifting of pKa$_{exp}$ values toward an acidic pH. In order to observe if sugar concentration was a limiting factor, a subsequent study was performed for glucose and fructose.

To test this hypothesis, a set of incubation experiments were carried out for glucose and fructose where the incubation time was fixed at 90 min. The concentration of glucose and fructose were varied from 0-500 ppm. Individual ζ_p measurements were taken at 0.2 pH increments in the range of 6-10 at each of the designated incubation times for each of the sugars (data not shown). The pKa_{exp} values were again extracted as before and plotted as a function of sugar concentration (Figure 5.9). It is clear from the data that the concentration of sugar had a significant impact on the magnitude in which the pKa_{exp} values shifted. The shift in pKa_{exp} was shown to be dependent on sugar concentration up to a concentration of 250 ppm. At 250 ppm sugar, the pKa_{exp} shifted to a pH of 7.6 for glucose and a pH of 6.6 for fructose. Both of these shifts in pKa_{exp} values are greater than observed for 20 ppm of each sugar in Figure 5.8. At a concentration of 250 ppm, it appears that sugar in excess and is no longer limiting the amount of complex formed.

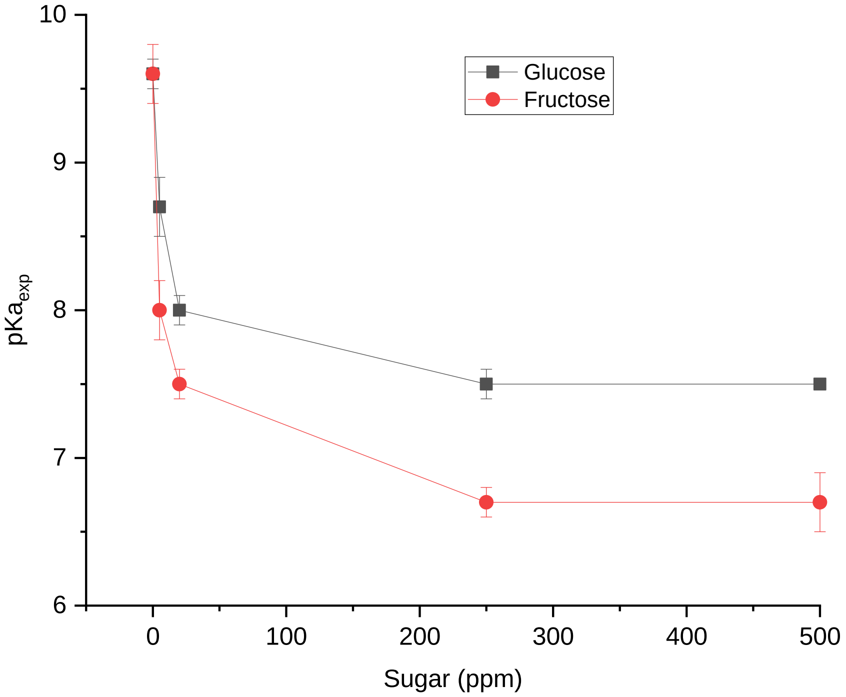

Figure 5.9 pKa_{exp} for BA-MNPs plotted as a function of sugar concentration. The BA-MNPs were allowed to bind with glucose or fructose for 90 min.

5.3.5 Effect of glucose binding on BA-MNP magnetophoretic transport

In earlier chapters, the magnetophoretic transport of functionalised MNPs was investigated and it was demonstrated that electrostatic interactions between the MNP and its environment can have significant effects on v_{exp}. In all cases up to now, it was assumed that the functionalised MNPs (PEG-, arginine-, citrate-) remained stable and unchanged over the transit through agarose. In this case, magnetophoretic transport of the BA-MNPs through agarose in the absence and presence of glucose is studied whereby the BA-MNPs in the presence of glucose would undergo binding of glucose in real-time and so their physiochemical characteristics would be expected to be dynamic over the agarose transit. It has already been shown that the BA-MNPs binds glucose which leads to increases in ζ_p and d_{hyd} and that binding is dependent on incubation time up to 90 min in aqueous solution. Based on this, it was investigated here how real-time glucose binding would affect the magnetophoretic transport of BA-MNPs. Given the earlier data relating to the increasing d_{hyd} of the BA-MNPs in the presence of glucose as well as the changes in ζ_p observed (which could modulate the electrostatic repulsive interactions between the BA-MNPs and the agarose) as a function of glucose binding, it would be expected that the uptake of glucose by the BA-MNP would have an impact on v_{exp}.

In order to carry out the experiments to investigate the effect of glucose on magnetophoretic transport, BA-MNPs were deposited onto the top surface of the agarose hydrogels (6 mm depth) which were prepared in DI H_2O and synthetic ISF in the presence of glucose (20 ppm), and also in DI H_2O in the absence of glucose as a control. Transport through the gels was induced by an N52 magnet (Figure 5.10). Linear velocity was observed in all cases, however the velocities differed across the different conditions. In agarose gels containing glucose, a notable decrease in v_{exp} was observed (0.28 ± 0.01 mm/h) when compared to agarose with no glucose in DI H_2O (0.33 ± 0.02 mm/h). Glucose binding in solution, even over short incubation periods has been shown to increase MNP size and the magnitude of the negative surface charge (Figure 5.5 A & B, respectively) and this is likely contributing to this decrease in velocity observed. The linearity of the data ($R^2>0.98$, in the cases of ISF and DI H_2O) would suggest that after 30 min, the binding of glucose to BA is occurring at a linear rate, or at least at a rate that can be approximated to be linear.

It is interesting to note that the velocity of BA-MNPs is slowest when the agarose in prepared in DI H_2O (compared to ISF 0.30 ± 0.01) containing glucose. This is expected as the electrostatic effects that would typically enhance velocity of negatively charged MNPs (Chapter 3) in DI H_2O will be minimised. Coupling this with the fact that d_{hyd} would be expected to be higher on account of the bound glucose could explain why this velocity is slowest of all conditions investigated.

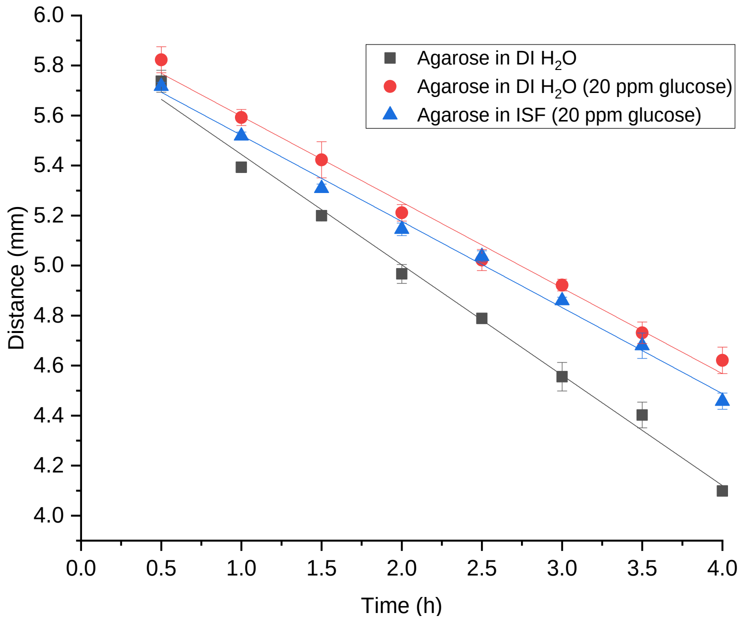

Figure 5.10 Magnetophoretic transport of ~2 mg/mL BA-MNPs (d_{hyd} 29.5 nm, (0.17)) through agarose-H_2O (0.3% w/v) with and without glucose (20 ppm). R^2 >0.98 for all data sets (n=4).

5.3.6 Quantitative analysis of glucose- binding to BA-MNPs

So far in this chapter, parameters that effect the formation of boronate esters related to glucose binding to BA-MNPs have been investigated. From this work, it is clear that the ζ_p of the MNPs can reflect the extent of binding of BA with sugars such as glucose. In this section, glucose uptake by the BA-MNPs from PBS solution will be examined quantitatively using an enzymatic assay approach. In order to quantify binding, the number of BA groups per mg of BA-MNPs was estimated. For this calculation, it was assumed that all GLYMO functional groups on the MNPs successfully coupled with an incoming BA. A grafting density of 1.99 GLYMO molecules per nm^2 was taken (Chapter 2), which equates to 495 BA functional groups per MNP. Hence, there is an estimated 2.53×10^{18} BA groups per mg of BA-MNPs.

Different masses of BA-MNPs were incubated with glucose solutions (50 ppm, 4 mL) for 90 min, at which point is was assumed that equilibrium binding was reached. MNPs were then magnetically extracted from solution, and the bound glucose quantified using a hexokinase (HK)-based glucose assay according to Section 5.2.6. The % glucose captured was plotted against MNP mass used (Figure 5.11).

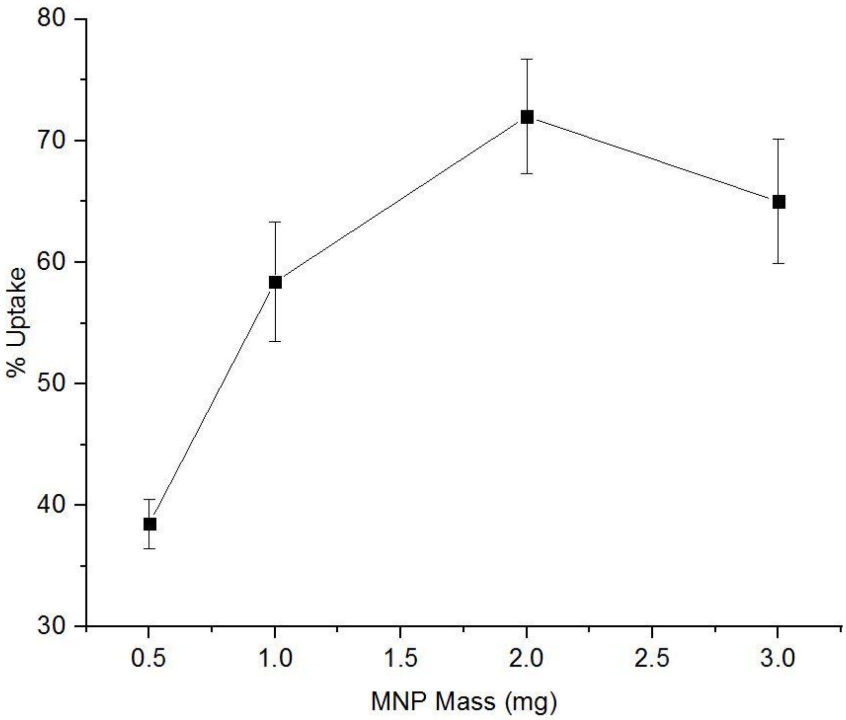

Figure 5.11 % glucose captured from PBS (4 mL, pH 7.4, 50 ppm glucose) for different masses of BA-MNPs (d_{hyd} 29.5 (0.17)) after 90 min (n=4). Glucose quantified using enzymatic assay.

It can be seen that increasing the mass of MNP increased the % glucose uptake up to a mass of 2 mg. Above 2 mg BA-MNPs, no further increase in the amount of glucose captured was observed, indicating the glucose became limiting at this point.

5.3.7 Glucose capture from agarose gel using BA-MNPs

In order to investigate glucose extraction efficiency for BA-MNPs from agarose gels, BA-MNPs were magnetophoretically transported through agarose-H_2O and agarose-ISF gels spiked with glucose (20 ppm). After full magnetophoretic transit, the BA-MNPs were extracted from the base of the gel (see Section 5.2.9). The glucose bound to the extracted BA-MNPs was quantified by colorimetric enzyme assay according to Section 5.2.7.

The estimated bound number of glucose molecules per BA-MNP after transit in these experiments were calculated based on the following numbers. The number of available BA groups per mg of material was taken to be 2.53×10^{18} as calculated previously. This calculation is based on the estimated 495 BA groups per individual MNP, obtained from TGA data (Chapter 2). The number of total glucose molecules available for binding is calculated by determining the mass of an individual glucose molecule. The number of glucose molecules per mg of glucose was calculated to be 3.34x10^{18}.

The total number of available glucose molecules was then divided by the % uptake by the MNPs to find the theoretical number of bound glucose molecules. The resulting number of theoretically bound glucose molecules is then divided by the number of BA sites to determine the number of bound glucose molecules per MNP in these experiments.

From the data in Table 5.1, it can be seen that BA-MNPs captured 56.2 ± 2.8% of available glucose in an agarose-H_2O gel under the conditions tested. This value is 13.8% lower than glucose capture in PBS solution (data taken from Figure 5.11). Impeded mass transport of the glucose and the BA-MNPs in the polymer network may account for this decrease in % uptake. There is also a small decrease in % uptake of glucose from agarose-ISF (51.2%) by the BA-MNPs when compared to the agarose-H_2O gel. This could be due to the presence of saccharose in the synthetic ISF (1.2 ppm) whereby competitive binding between the two sugars for the BA groups may have led to a decrease in glucose % uptake[34].

Table 5.1 % uptake of glucose by 2 mg of BA-MNPs (d_{hyd} 29.5 nm) in agarose gels (700 µL initial volume) in H_2O and synthetic ISF spiked with 20 ppm glucose (n=6).

Agarose solvent	BA-MNP mass (mg)	% uptake (20 ppm)	Bound glucose per MNP
H_2O	2	56.2 ± 2.8	133 ± 14
Synthetic ISF	2	51.2 ± 1.3	121 ± 6

These experiments show that the BA-MNPs were capable of capturing glucose from agarose gels whilst undergoing magnetophoretic transport. In order to characterise the method analytically, a calibration plot was generated. A range of agarose-ISF gels were prepared with varying amounts of glucose (0-50 ppm). Each individual gel contained a specific concentration of glucose. BA-MNPs (2 mg) were transported through a gel under the influence of an external magnetic field. The BA-MNPs were extracted from the bottom of the agarose gel. The resulting MNPs were washed to remove any physiosorbed glucose. The bound glucose was then quantified via the HK kit as it will react with the bound glucose present on the MNP surface. The response was linear across the full range and the method precision was good ($R^2 = 0.99$) (Figure 5.12). The theoretical limit of detection (LOD) was calculated based on this calibration curve (3s/m) and found to be 0.72 ppm. To quantify reproducibility, 10 agarose gels were prepared, all containing 10 ppm glucose. Glucose was extracted from each gel using the BA-MNPs and extracted glucose was quantified using the calibration curve. The glucose concentration measured was 10.0 ± 0.54 ppm, indicating excellent accuracy and precision for the method.

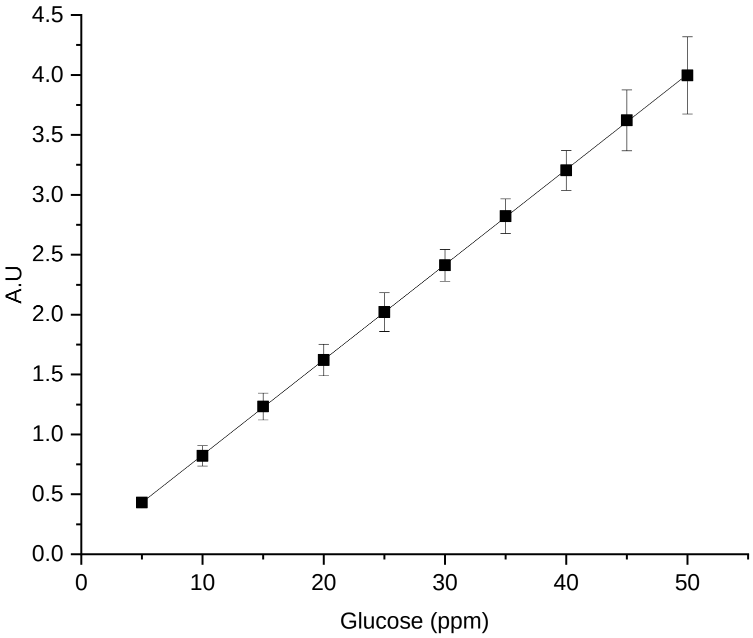

Figure 5.12 Calibration plot for quantification of glucose extracted from agarose-ISF using ~2 mg/mL BA-MNPs (d_{hyd} 29.5 nm), y= 0.0615x + 0.9757, $R^2 = 0.9996$, n=6.

The developed quantification method is suitable for relevant glucose levels in biological tissue fluid, ISF. The glucose concentration in the ISF fluctuates, but is directly correlated with blood glucose levels and is in the range of 150-500 ppm[38–41]. In relation to diagnostics, there have been challenges with accessing ISF for glucose and other diagnostic markers. Magnetophoretically-driven functionalised MNPs may provide an interesting opportunity for providing access to ISF biomarkers in a minimally invasive fashion for new diagnostic platforms in the future.

5.3.8 Effect of high field gradients on glucose capture

In Chapter 4, high magnetic field strengths induced using the Giamag (1.1 T) were shown to enhance magnetophoretic transport. It was demonstrated that at these higher field strengths electrostatic interactions between the BA-MNPs and the polymer network were ignored and influenced the MNPs to take a different pathway through the agarose compared to lower field strengths. In this experiment, the influence of a high field strength on glucose capture was studied. In order to investigate this, agarose-H_2O (0.3 %w/v) was spiked with glucose (20 ppm) and BA-MNPs (2 mg/ml) were magnetically guided through the agarose using the Giamag. MNPs were extracted from the base of the gel (Section 5.2.8), and bound glucose quantified. The results are tabulated below (Table 5.2).

Table 5.2 % uptake of glucose by BA-MNPs (2 mg, d_{hyd} 29.5 nm) in agarose-H_2O gels (700 µL initial volume) using Giamag and N52 magnets (n=6).

Magnet	Glucose (ppm)	% Uptake	Bound glucose per MNP
N52	20	56.2 ± 2.8	132 ± 14
Giamag	20	41.3 ± 1.8	97 ± 9

It can be seen that there was a decrease in glucose uptake of ~15% when using the Giamag when compared to the N52. The BA-MNPs take ~72 min to move through the full depth of the agarose under the influence of the Giamag (~12 times faster than N52). This faster transit reduces the effective incubation time of the MNPs with glucose. Earlier studies showed equilibrium binding was reached after 90 min in solution. The time required to reach equilibrium binding may indeed be longer that this in the agarose hydrogel on account of a slowed mass transport due to the presence of the polymer network. The reduced incubation time may be the reason for the decreased % uptake observed.

5.3.9 Investigation of glucose uptake by BA-MNPs in cultured ECM

The ability of the BA-MNPs to capture glucose from cultured ECM was investigated. Studies in Chapter 4 showed that functionalised MNPs were able to be magnetophoretically transported through cultured ECM. Hence BA-MNPs were investigated here to capture glucose from this medium during magnetophoretic transport using the N52. The ECM was diluted with Dulbecco's Modified Eagles Medium (DMEM) in a 1:1 ratio[42] and spiked with sterile glucose (10, 20 and 50 ppm). MNPs were magnetophoretically guided through the glucose-spiked ECM, and extracted from the base of the gel after a transit time of 10 h. Given the long transit time, it was assumed equilbrium binding was achieved in these experiments. The % uptake of glucose by the BA-MNPs in ECM is tabulated below (Table 5.3).

Table 5.3 % Uptake of glucose (10-50 ppm) by BA-MNPs (2 mg, d_{hyd} 29.5 nm (0.18)) in ECM and agarose-ISF (both 700 µL initial volumes) for comparison using the N52 magnet, n=4.

	ECM	
[Glucose] (ppm)	**% uptake**	**Bound glucose per MNP**
10	50.2 ± 1.3	59 ± 6
20	49.2 ± 0.9	116 ± 4
50	41.3 ± 2.4	243 ± 12

	Agarose-ISF	
[Glucose] (ppm)	**% uptake**	**Bound glucose per MNP**
10	54.4 ± 1.1	64 ± 5
20	51.2 ± 1.3	121 ± 6
50	46.2 ± 1.7	272 ± 8

It can be seen that the % uptake of glucose increases with increasing glucose concentration in solution which is what is expected as the maximum binding capacity (estimated to be 495 glucose molecules per MNP) was not reached in these experiments. Future experiments will involve increasing the glucose concentration to see at what point this mass of MNPs reach binding capacity experimentally. The % uptake decreased by ~5% in cultured ECM when compared to agarose-ISF. This decrease may be due to the increased tortuosity of the ECM, as it is a significantly more complex environment than agarose. It is also possible that the presence of other sugars in the ECM may competitively bind the BA. The low variance between samples and data sets demonstrates reproducibility of the developed extraction method. This study demonstrates the ability of functionalised MNPs to capture biomarkers whilst undergoing magnetophoretic transport in cultured ECM for the first time. It highlights the viability of other functionalisation’s (e.g. antibody, aptamer, etc) to allow the capture of other biomarkers from biological tissue mimics and ultimately in vivo in the future.

5.4 Conclusion

In this chapter, BA-MNPs were investigated for their ability to bind glucose from polymer gels and ECM during magnetophoretic transport. BA-MNPs were synthesised and characterised. The effect of pH on colloidal stability and ζ_p were investigated. It was hypothesised that BA-MNP ζ_p values were directly linked to the ionisation state of the immobilised BA. Changes in d_{hyd} and ζ_p in the presence of glucose were observed, which were attributed to glucose binding. pKa_{exp} values, a measure of the pKa of the BA, were extracted from the ζ_p plots as a function of pH and shown to decrease upon glucose- and other polysaccharide-binding.

Quantitative glucose uptake by the BA-MNPs from agarose gels was demonstrated. It was shown that glucose could be taken up by the BA-MNPs and quantified via enzymatic assay, demonstrating its usefulness for future in-vivo biocapture applications in tissue.

The influence of a high magnetic field strength was show to decrease the glucose captured by the BA-MNPs. These findings support the earlier findings that 90 min is needed for optimum glucose binding. BA-MNPs were then used to capture glucose in varying concentration from cultured ECM. The promising results obtained lay the foundation for further functionalisation to target more complex biomarkers in vivo.

To our knowledge, this is one of the first studies to use an understanding of magnetophoretic transport for the capture of glucose from an agarose gel under the influence of a magnetic field. The effect of glucose binding on BA-MNP magnetophoretic motion has not been studied previously. It opens up the possibility of extended biomarker capture using functionalised MNPs whereby BA can be used to target other biologically-relevant targets such as catecholamines and steroids. In addition, the MNPs can be functionalised with antibodies or aptamers to induce selectivity for different biomarkers.

5.5 References

1. Yarmola, E. G., Shah, Y., Arnold, D. P., Dobson, J. & Allen, K. D. Magnetic Capture of a Molecular Biomarker from Synovial Fluid in a Rat Model of Knee Osteoarthritis. *Ann. Biomed. Eng.* **44**, 1159–1169 (2016).
2. Yarmola, E. G., Shah, Y. Y., Kloefkorn, H. E., Dobson, J. & Allen, K. D. Comparing Intra-Articular CTXII Levels Assessed via Magnetic Capture or Lavage in a Rat Knee Osteoarthritis Model. *Osteoarthr. Cartil.* **25**, 1189–1194 (2017).
3. Sperling, R. A. & Parak, W. J. Surface Modification, Functionalization and Bioconjugation of Colloidal Inorganic Nanoparticles. *Philos. Trans. A. Math Phys. Eng. Sci.* **368**, 1333–1383 (2010).
4. Lavigne, J. J., James, T. D., Phillips, M.D and Shinkai, S. Boronic Acids in Saccharide Recognition *J. Am. Chem. Soc.* **129**, 10964–10964 (2007).
5. Martínez-Aguirre, M. A., Villamil-Ramos, R., Guerrero-Alvarez, J. A. & Yatsimirsky, A. K. Substituent Effects and pH Profiles for Stability Constants of Arylboronic Acid Diol Esters. *J. Org. Chem.* **78**, 4674–4684 (2013).
6. Chen, J.-X., Shi, Y., Zhang, Y.-R., Teng, L.-P. & Chen, J.-H. One-Pot Construction of Boronate Ester Based pH-Responsive Micelle for Combined Cancer Therapy. *Colloids Surf. B Biointerfaces* **143**, 285–292 (2016).
7. Springsteen, G. & Wang, B. A Detailed Examination of Boronic Acid–Diol Complexation. *Tetrahedron* **58**, 5291–5300 (2002).
8. Wu, X. *et al.* Selective Sensing of Saccharides using Simple Boronic Acids and their Aggregates. *Chem. Soc. Rev.* **42**, 8032–8048 (2013).
9. Egawa, Y., Miki, R. & Seki, T. Colorimetric Sugar Sensing Using Boronic Acid-Substituted Azobenzenes. *Materials* **7**, 1201–1220 (2014).
10. Forrester, M. & Kusmartsev, F. The Nano-Mechanics and Magnetic Properties of High Moment Synthetic Antiferromagnetic Particles. *Phys. Status Solidi (a)* **211**, 884–889 (2014).
11. Bruen, D. *et al.* Boronic Acid Homopolymers as Effective Polycations for Sugar-Responsive Layer-by-Layer Assemblies. *ACS Appl. Polym. Mater.* **1**, 990–996 (2019).
12. Elsherif, M., Hassan, M. U., Yetisen, A. K. & Butt, H. Glucose Sensing with Phenylboronic Acid Functionalized Hydrogel-Based Optical Diffusers. *ACS Nano,* **12**, 2283–2291 (2018).
13. Resendez, A. & Malhotra, S. V. Boronic Acid Appended Naphthyl-Pyridinium Receptors as Chemosensors for Sugars. *Sci. Rep.* **9**, 1–10 (2019).
14. Zhang, X., Liu, G., Ning, Z. & Xing, G. Boronic Acid-Based Chemical Sensors for Saccharides. *Carbohydr. Res.* **452**, 129–148 (2017).
15. Ma, R. & Shi, L. Phenylboronic Acid-Based Glucose-Responsive Polymeric Nanoparticles: Synthesis and Applications in Drug Delivery. *Polym. Chem.* **5**, 1503–1518 (2014).
16. Zhao, L. *et al.* Boronic Acid as Glucose-Sensitive Agent Regulates Drug Delivery for Diabetes Treatment. *Materials* **10**, (2017).

17. Qian, X. *et al.* Targeting and Microenvironment-Improving of Phenylboronic Acid-Decorated Soy Protein Nanoparticles with Different Sizes to Tumor. *Theranostics* **9**, 7417–7430 (2019).
18. Wang, X., Wei, B., Cheng, X., Wang, J. & Tang, R. Phenylboronic Acid-Decorated Gelatin Nanoparticles for Enhanced Tumor Targeting and Penetration. *Nanotechnology* **27**, 385101 (2016).
19. Fang, G. *et al.* Recent Development of Boronic Acid-Based Fluorescent Sensors. *RSC Adv.* **8**, 29400–29427 (2018).
20. He, X., Yu, Y. & Li, Y. Facile Synthesis of Boronic Acid-Functionalized Magnetic Metal–Organic Frameworks for Selective Extraction and Quantification of Catecholamines in Rat Plasma. *RSC Adv.* **8**, 41976–41985 (2018).
21. Kook, J. K., Phung, V.-D., Koh, D.-Y. & Lee, S.-W. Facile Synthesis of Boronic Acid-Functionalized Magnetic Nanoparticles for Efficient Dopamine Extraction. *Nano Convergence* **6**, 30 (2019).
22. Xue, X. *et al.* A Facile and General Approach for the Preparation of Boronic Acid-Functionalized Magnetic Nanoparticles for the Selective Enrichment of Glycoproteins. *Analyst* **144**, 641–648 (2019).
23. Scarano, W., Lu, H. & Stenzel, M. H. Boronic Acid Ester with Dopamine as a Tool for Bioconjugation and for Visualization of Cell Apoptosis. *Chem. Commun.* **50**, 6390–6393 (2014).
24. Mello, G. P. C. *et al.* Glucose Sensing by Fluorescent Nanomaterials. *Crit. Rev. Anal. Chem.* **49**, 542–552 (2019).
25. Stephenson-Brown, A. *et al.* Glucose Selective Surface Plasmon Resonance-Based Bis-Boronic Acid Sensor. *Analyst* **138**, 7140–7145 (2013).
26. Lim, S. H., Musto, C. J., Park, E., Zhong, W. & Suslick, K. S. A Colorimetric Sensor Array for Detection and Identification of Sugars. *Org. Lett.* **10**, 4405–4408 (2008).
27. Zhao, Z. *et al.* Nanocaged Enzymes with Enhanced Catalytic Activity and Increased Stability Against Protease Digestion. *Nat. Commun.* **7**, 10619 (2016).
28. Atacan, K., Cakiroglu, B. & Ozacar, M. Improvement of the Stability and Activity of Immobilized Trypsin on Modified Fe3O4 Magnetic Nanoparticles for Hydrolysis of Bovine Serum Albumin and its Application in the Bovine Milk. *Food Chem.* **212**, 460–468 (2016).
29. Wang, Y., Huang, F., Sun, Y., Gao, M. & Chai, Z. Development of Shell Cross-Linked Nanoparticles Based on Boronic Acid-Related Reactions for Self-Regulated Insulin Delivery. *J. Biomater. Sci.* **28**, 93–106 (2017).
30. Furikado, Y. *et al.* Universal Reaction Mechanism of Boronic Acids with Diols in Aqueous Solution: Kinetics and the Basic Concept of a Conditional Formation Constant. *Chemistry – A European Journal* **20**, 13194–13202 (2014).
31. Curtis, C., Toghani, D., Wong, B. & Nance, E. Colloidal Stability as a Determinant of Nanoparticle Behavior in the Brain. *Collo. Surf. B.* **170**, 673–682 (2018).
32. Ramadan, W., Karim, M., Hannoyer, B. & Saha, S. Effect of pH on the Structural and Magnetic Properties of Magnetite Nanoparticles Synthesised by Co-Precipitation. *Adv. Mater. Res.* **324**, 129–132 (2012).

33. Dhadge, V. L., Hussain, A., Azevedo, A. M., Aires-Barros, R. & Roque, A. C. A. Boronic Acid-Modified Magnetic Materials for Antibody Purification. *J. R. Soc. Interface* **11**, (2014).
34. Ni, N. *et al.* Probing the General Time Scale Question of Boronic Acid Binding with Sugars in Aqueous Solution at Physiological pH. *Bioorg. Med. Chem.* **20**, 2957–2961 (2012).
35. Sun, X. *et al.* The Mechanisms of Boronate Ester Formation and Fluorescent Turn-On in Ortho -Aminomethylphenylboronic Acids. *Nat. Chem.* **11**, 768–778 (2019).
36. Marco-Dufort, B. & Tibbitt, M. W. Design of Moldable Hydrogels for Biomedical Applications Using Dynamic Covalent Boronic Esters. *Mater. Today Chem.* **12**, 16–33 (2019).
37. Yan, J., Springsteen, G., Deeter, S. & Wang, B. The Relationship Among pKa, pH, and Binding Constants in the Interactions Between Boronic Acids and Diols—It is Not as Simple as it Appears. *Tetrahedron* **60**, 11205–11209 (2004).
38. Thennadil, S. N. *et al.* Comparison of Glucose Concentration in Interstitial Fluid, and Capillary and Venous Blood During Rapid Changes in Blood Glucose Levels. *Diabetes. Technol. Ther.* **3**, 357–365 (2001).
39. Cobelli, C., Schiavon, M., Dalla Man, C., Basu, A. & Basu, R. Interstitial Fluid Glucose Is Not Just a Shifted-in-Time but a Distorted Mirror of Blood Glucose: Insight from an In Silico Study. *Diabetes. Technol. Ther.* **18**, 505–511 (2016).
40. Kulcu, E., Tamada, J. A., Reach, G., Potts, R. O. & Lesho, M. J. Physiological Differences Between Interstitial Glucose and Blood Glucose Measured in Human Subjects. *Diabetes Care* **26**, 2405–2409 (2003).
41. Wiig, H., Tenstad, O., Iversen, P. O., Kalluri, R. & Bjerkvig, R. Interstitial Fluid: The Overlooked Component of the Tumor Microenvironment? *Fibrog.Tissue Repair* **3**, 12 (2010).
42. Kuhn, S. J., Hallahan, D. E. & Giorgio, T. D. Characterization of Superparamagnetic Nanoparticle Interactions with Extracellular Matrix in an In Vitro System. *Ann. Biomed. Eng.,* **34**, 51–58 (2006).

Chapter 6

Conclusion and Future Work

6.1 Concluding remarks

This thesis contributes to the understanding of magnetophoretic transport of magnetic nanoparticles and factors that influence movement in a magnetic field through various biphasic polymer network-aqueous environments that mimic the extracellular environment of tissue. This work is significant because it provides an in-depth analysis of the physical, chemical and electrostatic effects that can influence magnetophoretic transport through agarose hydrogels and the ECM. It is critical to understand how specifically functionalised MNPs will interact with their surroundings for any biomedical application. The electrostatics that are present on the surface of the MNP and in the environment will dictate magnetophoretic transport. By understanding the influences that affect magnetophoresis, it is possible to optimise the characteristics of the MNP to enhance transport for sensing, drug delivery, biotargeting, biodetection or hyperthermia. The following paragraphs set out the specific detailed conclusions from all experimental chapters.

A review of relevant theory and literature in relation to the synthesis and functionalisation of MNPs for magnetophoretic-based bioapplications is presented. A detailed understanding of the potential for MNPs as a diagnostic platform for a multitude of in vivo applications was obtained. Synthesis of MNPs is well-established and enables tailored core sizes and magnetisation properties depending on desired application. MNP functionalisation chemistries are diverse and can be tailored depending on the desired properties needed. However, surface chemistry limitations still exist for MNP use in vivo including particle aggregation over time and subsequent recognition by the immune system. Manipulating MNPs in magnetic fields is broadly applied in MNP applications. However, there are only very few fundamental studies studying MNP velocity under magnetic field strengths and understanding the parameters that can impact on transport. Some initial studies have experimentally designed methods to measure particle velocities in media of defined bulk viscosities, including tissue mimics. Comparing these to theoretical velocity calculations and modelling of magnetic field gradients to explain certain phenomena have been done. The effects of certain parameters including intermolecular interactions of the MNPs with their environments, field strength, and tortuosity have not been yet been observed or fully elucidated to date. This thesis attempts to give further understanding of magnetophoresis of functionalised MNPs.

In Chapter 2, the synthesis of monodisperse superparamagnetic NPs was achieved with high reproducibility and low inter-batch variability. Functionalisation of the resulting MNP cores was carried out and resulting functionalised MNPs characterised. A method was developed to study magnetophoretic transport of these functionalised MNPs using an N52 magnet to generate the magnetic field gradient and biphasic agarose gel as the medium. This method was characterised and optimised by examining the impacts of parameters such as hydrogel dimensions, magnet geometry and an initial investigation into the impact MNP surface chemistry was carried out. Five surface functionalisation's (PEG, citrate, arginine, boronic acid, dopamine sulphonate) were investigated and different experimental velocities observed in each case indicating that surface chemistry may have an influence on magnetophoretic transport, which was then further interrogated in Chapter 3. Overall, this chapter set out the methodology used in the thesis for studying magnetophoretic transport, demonstrating excellent consistency and precision of the optimised method.

In Chapter 3, an equation derived from the balancing of drag and magnetic forces was used to predict theoretical velocities of MNPs moving through agarose gels which were then compared to the experimentally observed values. A tortuosity factor, φ, was proposed to account for the tortuous pathway that the MNPs must navigate through, given the biphasic nature of agarose. By comparing v_{exp} and v_{th} values, %D values were calculated. %D was shown to vary for the different surface chemistries indicating that an additional force was influencing magnetophoretic transport that was not accounted for in the velocity equation. Negatively charged MNPs moved slower than expected, while positively charged MNPs moved faster than expected. Electrostatic interactions between the fixed interactions on the agarose backbone and the charged MNP surface were proposed as the cause of this difference. The effect of these influences was investigated by manipulating the ionic strength of the aqueous phase and number of charged residues on the agarose polymer chains. It was observed that the electrostatics at the pore entrances and exits were influencing magnetophoretic transport and this was explained in the content of the electroendosmosis (EEO) effect observed before for molecular motion in fluidic channels. This study demonstrated strong evidence for the first time that electrostatic interactions at the particle level and its environment can influence magnetophoretic transport.

Magnetophoretic transport in more complex gels including agarose/collagen and in cultured ECM was studied in Chapter 4. The addition of collagen to agarose led to prominent hydrophobic effects at the gel surface and an increased tortuosity. The collagen fibres interacted with the charged MNPs, hindering their transport, further influencing magnetophoretic transport. The ECM possesses a significantly different environment, described by the ηφ factors in the velocity equation, compared to any of the agarose- gels previously studied. Initial magnetophoretic transport studies suggest the ECM is overall a negatively charged environment, which may relate to the presence of the various negatively charged proteoglycans within the non-fibrillar network of ECM.

A second aspect of Chapter 4 was the study of magnetophoretic transport in magnetic field strengths significantly higher than that given by the N52 magnet. A Giamag was used for these studies (approx. 5 times greater field strength) and greatly enhanced velocities were observed on account of the higher field strength. When compared to theoretical calculations, no differences (% D values) were found which were explained by the different interactions of the MNP chemistries with the polymer network whereby electrostatic effects could effectively be ‘switched off’ in the presence of the Giamag. Transport through ECM has shown that functionalised MNPs (PEG1000-, citrate- and arginine-) are capable of being guided through such a complex environment and remain stable for time periods of 8 h.

Chapter 5 investigated an affinity-based binding chemistry attached to MNPs for future in-vivo biomarker targeting in tissue. Biomarker targeting was demonstrated in this chapter using a boronic acid (BA) functionalisation chemistry. BA-MNPs were synthesised and then characterised (prior to polysaccharide binding) to understand the effect of pH on MNP surface charge. It was demonstrated that the ionisation state of the BA could be tracked as a function of pH by way of ζ_p. Upon binding of glucose to the BA, the ζ_p was observed to shift negatively toward an acidic pH in a consistent manner with the expected change in charge upon conversion of the BA to the boronate ester. Based on the data, experimental pKas (pKa_{exp}), a measure of the pKa, were obtained. This is the first time to our knowledge that the ionisation state of boronic acids has been characterised via ζ_p. To explore the biotargeting (or sampling) capability of the BA-MNPs, magnetophoretic transport experiments demonstrates the binding of glucose during transport through agarose gels. After transport through gels, MNPs were extracted from the gels and MNP-bound glucose quantitatively assessed via colorimetric enzyme assay to characterise capture efficiency. Analytical characterisation of this method demonstrated a capture efficiency of ~50%, 200 molecules of glucose taken up per MNP under the conditions used and a LOD of 0.73 ppm demonstrated the relevance of this sampling and analysis methodology for low concentration biomarker targeting in the extracellular matrix in the future.

Overall, this thesis contributes to the understanding of magnetophoretic transport and proposes new insights into the factors that can influence magnetophoretic transport. MNP size, surface charge, the physical and chemical composition of the surrounding environment and the magnetic field strength all play influential roles in governing magnetophoretic transport. This work has highlighted the roles that tortuosity and viscosity play in transport for MNPs. This work lays the foundation for further studies in biomedical applications that use magnetophoresis as a potential method to achieve their aim.

The advancements in magnetophoretic transport of MNPs through tissue and complex biological environments have opened up new ways to improve various biomedical applications such as site-specific drug delivery, specific tumour targeting or biomarker capture and detection. The various factors that can influence magnetophoretic transport have been studied in detail within this thesis. However, there remains more studies to be undertaken to realise in-vivo applications for this work. Further studies in human skin or tissue in vitro are required. There are still limitations to using MNPs for this use, mainly the safe delivery and extraction from tissue. The use of MNPs as a tool for minimally-invasive biomarker detection in complex media such as ECM could allow for the early detection of disease. This would present exciting opportunities for MNPs in clinical applications for example in the early detection of disease and in therapeutic drug delivery for the future.

6.2 References

1. Plecis, A., Schoch, R. B. & Renaud, P. Ionic Transport Phenomena in Nanofluidics: Experimental and Theoretical Study of the Exclusion-Enrichment Effect on a Chip. *Nano Lett.* **5**, 1147–1155 (2005).
2. Starodoubtsev, S. G., Churochkina, N. A. & Khokhlov, A. R. Hydrogel Composites of Neutral and Slightly Charged Poly(acrylamide) Gels with Incorporated Bentonite. Interaction with Salt and Ionic Surfactants. *Langmuir* **16**, 1529–1534 (2000).
3. Wei, W. & Wang, Z. Investigation of Magnetic Nanoparticle Motion under a Gradient Magnetic Field by an Electromagnet. *J. Nanomater.* (2018)
4. Leong, S. S., Yeap, S. P. & Lim, J. Working Principle and Application of Magnetic Separation for Biomedical Diagnostic at High- and Low-Field Gradients. *Interface Focus* **6**, 20160048 (2016).
5. Liu, J. F. *et al.* Use of Oppositely Polarized External Magnets To Improve the Accumulation and Penetration of Magnetic Nanocarriers into Solid Tumors. *ACS Nano* **14**, 142–152 (2020).